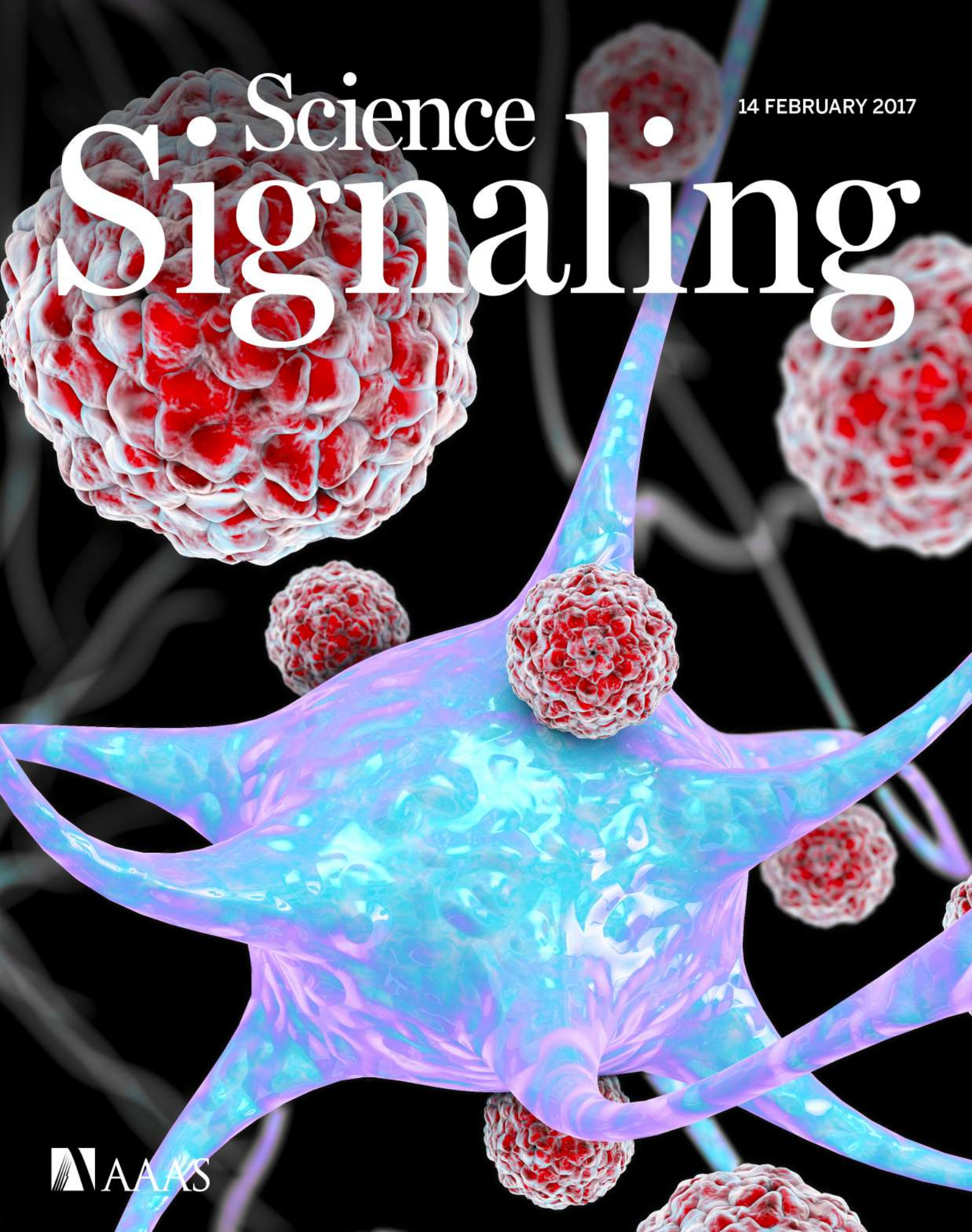
Science
Signaling
14 FEBRUARY 2017
AAAS

ANTIVIRAL IMMUNITY

The host microRNA miR-301a blocks the IRF1-mediated neuronal innate immune response to Japanese encephalitis virus infection

Bibhabasu Hazra, Kanhaiya Lal Kumawat, Anirban Basu*

Effective recognition of viral components and the subsequent stimulation of the production of type I interferons (IFNs) is crucial for the induction of host antiviral immunity. The failure of the host to efficiently produce type I IFNs in response to infection by the Japanese encephalitis virus (JEV) is linked with an increased probability for the disease to become lethal. JEV is a neurotropic virus of the *Flaviviridae* family that causes encephalitis in humans. JEV infection is regulated by several host factors, including microRNAs, which are conserved noncoding RNAs that participate in various physiological and pathological processes. We showed that the JEV-induced expression of *miR-301a* led to inhibition of the production of type I IFN by reducing the abundances of the transcription factor IFN regulatory factor 1 (IRF1) and the signaling protein suppressor of cytokine signaling 5 (SOCS5). Mechanistically, induction of *miR-301a* expression during JEV infection required the transcription factor nuclear factor κB. In mouse neurons, neutralization of miR-301a restored the host innate immune response by enabling IFN-β production, thereby restricting viral propagation. Inhibition of miR-301a in mouse brain rescued the production of IRF1 and SOCS5, increased the generation of IFN-β, and reduced the extent of JEV replication, thus improving mouse survival. Thus, our study suggests that the JEV-induced expression of *miR-301a* assists viral pathogenesis by suppressing IFN production, which might be targeted by antiviral therapies.

INTRODUCTION

Japanese encephalitis (JE) is a disease of public health importance because of its epidemic potential and high fatality rate. JE virus (JEV) is the leading cause of viral encephalitis in the Asia-Pacific region since its initial outbreak in 1871 in Japan (*1*). JEV is a single-stranded, positive-sense, mosquito-borne flavivirus that belongs to the same genus as the dengue virus (DENV), yellow fever virus, Zika virus, and West Nile virus (WNV). After entering the body, JEV invades the central nervous system (CNS) and clinically manifests as fever, headache, and vomiting. About one-third of patients die, and half of the survivors suffer permanent neuropsychiatric sequelae (*2*). According to the World Health Organization, most of the countries in Southeast Asia and the Western Pacific region have endemic JEV transmission, exposing more than 3 billion people to the risks of infection (*3*). With rapid globalization and climate shift, JEV has started to emerge in areas where the threat was previously unknown and has become the cause of worldwide pandemics (*4*). Although multiple vaccines with varying degrees of effectiveness exist to control JE, there is no cure for the disease (*5*), and treatment is mainly palliative.

Type I interferons (IFNs) are best known for their ability to induce an antiviral state by stimulating the transcription of IFN-stimulated genes (ISGs), the products of which affect multiple stages of the viral replication cycle (*6*). In addition, type I IFNs activate key components of the innate and adaptive immune systems, including the maturation of antigen-presenting cells and the production of cytokines involved in the activation of T cells, B cells, and natural killer cells (*7*). Pattern recognition receptors (PRRs) have become universally important in inducing the production of type I IFNs during viral infections by recognizing various viral components (*8*). In the case of JEV, we previously showed that the recognition of viral products by PRRs, including Toll-like receptor 7 (TLR7) and retinoic acid–inducible gene I, serves to elicit immunological responses involving type I IFNs in neurons (*9*–*11*). Despite this, different strategies are adopted by JEV to overpower the antiviral activities of type I IFNs (*12*, *13*). Failure of the host to produce IFNs competently against the virus is linked with an increased probability of the disease to become lethal (*14*). However, evasion of the immune system by JEV and its consequences might be mitigated if the type I IFN response could be augmented during viral infection, a proposal that is supported by studies reporting inhibition of the replication of different flaviviruses by IFN-based therapy (*15*–*17*).

MicroRNAs (miRNAs) have emerged as key posttranscriptional regulators of gene expression, and they affect nearly every cellular process (*18*). Because individual miRNAs can regulate the expression of multiple mRNAs, it is difficult to conclude whether an increase in the abundance of a specific miRNA represents a part of the host innate immune response to restrict viral infection or whether it was specifically induced by the virus to promote a cellular environment more favorable to viral replication (*19*). Increasing evidence indicates that cellular miRNAs can exert positive or negative influences on flaviviral infection. WNV infection induces the production of miR-154, which expedites virus-mediated apoptosis by targeting the mRNAs corresponding to cellular antiapoptotic factors (*20*). As a part of the host immune response, miR-532-5p exhibits antiviral activity against WNV through its suppression of the expression of the host genes SEC14 and spectrin domain containing 1 (*SESTD1*) and transforming growth factor–β–activated kinase 1/MAP3K7 binding protein 3 (*TAB3*) (*21*). The miRNA let-7c inhibits DENV infection by targeting the DENV genome (*22*). Another host miRNA, miR-30e*, substantially suppresses DENV replication by promoting IFN-β production, whereas miR-223 inhibits DENV by negatively regulating the microtubule-destabilizing protein stathmin 1 (STMN1) (*23*, *24*). Another flavivirus, JEV, reduces the abundance of miR-33a-5p in the host to stabilize the components of the JEV replicase complex and thus enhance JEV replication (*25*). Two other miRNAs, miR-155 and miR-15b, are induced during JEV infection and modulate JEV-induced innate immunity and inflammatory responses, respectively (*26*, *27*). In our previous studies, we found that the expression of many miRNAs was induced abruptly

National Brain Research Centre, Manesar, Haryana 122051, India.
*Corresponding author. Email: anirban@nbrc.ac.in

during JEV infection (*28*); among these, the regulation of two host miRNAs, miR-29b and miR-155, in JEV-induced microglial inflammation has already been documented (*28*, *29*).

Here, we investigated the role of miR-301 family (miR-301a and miR-301b) and initially investigated whether the increase in miR-301 abundance during JEV infection exclusively occurred in microglia. We found that the abundances of both these miRNAs were increased in microglia together with that of miR-301a in neurons early during JEV infection. The altered amounts of miRNAs early during infection were generally coupled with pathogen detection and the host immune response. Because a proinflammatory function of miR-301a is well established in different models (*30*–*33*) but its role in the immune response is not well characterized (*34*), its prompt induction in neurons motivated us to investigate host immune regulation of miR-301a during JEV infection. Here, we postulate that the JEV-induced increase in host miR-301a abundance may inhibit type I IFN signaling and enable JEV to take advantage of a weakened immune system.

RESULTS

miR-301a expression is enhanced early during JEV infection of neurons

We previously used miRNA polymerase chain reaction (PCR)–based arrays to analyze the miRNA expression profile in JEV-infected microglia (BV2 cells) and found that the abundance of members of the miR-301 family (miR-301a and miR-301b) was markedly increased compared to that in uninfected cells (*28*). Here, we performed quantitative reverse transcription PCR (qRT-PCR) analysis of the abundance of miR-301 family members in BV2 cells and in HT22 cells, a mouse hippocampal neuronal cell line. As shown previously, BV2 cells exhibited increased abundance of miR-301a and miR-301b 12 hours after infection with JEV, whereas a substantial early increase in miR-301a abundance (up to 6 hours) was also observed in JEV-infected HT22 cells (fig. S1, A and B). Furthermore, HT22 cells infected with varying concentrations of JEV for 6 hours had a higher abundance of miR-301a than mock-infected (MI) cells, suggesting that infection with JEV at early times induces the expression of *miR-301a* in HT22 cells (Fig. 1A). Similar results were obtained from the analysis of the time and dose dependency of *miR-301a* expression in JEV-infected primary cortical neurons (Fig. 1, B and C). To detect the early induction of *miR-301a* expression in mouse brain neurons, we performed both in situ hybridization (ISH) analysis for miR-301a or U6 small nuclear RNA (snRNA) (as a positive control) and immunohistochemical (IHC) analysis of neurons in uninfected and JEV-infected (2 days after infection) mouse brain sections. Although both sections showed similar amounts of U6 snRNA, the increased abundance of miR-301a was observed only in the neurons of JEV-infected mice (Fig. 1D). Next, we validated the expression of *miR-301a* in JEV-infected human neuroblastoma (SH-SY5Y) cells. Our qRT-PCR analysis showed both time- and dose-dependent increase in the abundance of miR-301a early during JEV infection (Fig. 1, E and F). Together, these results suggest that *miR-301a* expression in neurons is enhanced early during JEV infection.

miR-301a inhibits the antiviral IFN response and promotes JEV replication

Induction of miRNAs early during infection usually regulates the antiviral IFN response and viral replication. To explore whether the silencing of miR-301a could augment the production of type I IFNs, we transfected HT22 and SH-SY6Y cells with either an miR-301a inhibitor (anti–miR-301a) or a negative control (anti–miR-Con) 24 hours before the cells were subjected to JEV infection. We observed a substantial decrease in miR-301a abundance in the cells transfected with anti–miR-301a compared to that in cells transfected with anti–miR-Con (Fig. 2A and fig. S2A). Inhibition of miR-301a led to a substantial increase in *IFN*-β mRNA abundance, whereas *IFN*-α mRNA abundance remained unchanged up to 6 hours after infection of HT22 cells (Fig. 2, B and C). We observed a similar trend in *IFN*-α (fig. S2B) and *IFN*-β (fig. S2C) mRNA abundances in JEV-infected SH-SY5Y cells. The amount of IFN-β secreted by infected HT22 cells transfected with anti–miR-301a was also increased compared to that secreted by control cells as determined by enzyme-linked immunosorbent assay (ELISA) (Fig. 2D). Inhibition of miR-301a led to the increased expression of ISGs in both HT22 (Fig. 2E) and SH-SY5Y cells (fig. S2D) up to 6 hours after JEV infection. Because IFNs play a pivotal role in the host antiviral defense, we further assessed whether anti–miR-301a affected viral replication, and we found that there was a substantial reduction in viral RNA abundances in both HT22 (Fig. 2F) and SH-SY5Y cells (fig. S2E) that were transfected with anti–miR-301a, as analyzed by qRT-PCR. We also checked the long-term effect of the miRNA inhibitor on JEV infection and detected a marked decrease in the viral titer (number of viral particles) in the culture medium of HT22 cells 48 hours after infection (Fig. 2G).

Virus-induced miR-301a targets a number of host genes

To gain insight into the mechanism underlying miR-301a function, we analyzed miR-301a target genes that might influence the IFN response in our model of JE. We found more than 500 common target genes of mouse miR-301a by analyzing four widely used miRNA target prediction databases: Miranda (*35*), TargetScan (*36*), PicTar (*37*), and miRDB (*38*). Among these targets, 100 common targets that had high binding scores were identified (table S1). To identify prospective candidate target genes whose products might control JEV replication, we chose to investigate suppressor of cytokine signaling 5 (SOCS5) and IFN regulatory factor 1 (IRF1) because they are potential regulators of innate immunity (*39*, *40*). The targeting of the genes encoding SOCS5 and IRF1 by miR-301a could have a broad effect on the innate response against JEV. All computational analyses indicated that there was a conserved miR-301a binding site within the 3′ untranslated regions (3′UTRs) of *SOCS5* (Fig. 3A) and *IRF1* (Fig. 3B).

To verify these database predictions, we cloned the 3′UTRs of mouse *SOCS5* and *IRF1* into a firefly luciferase reporter vector. We then generated six- and seven-base mutations in the predicted seed matching site in the 3′UTRs of *SOCS5* (Fig. 3C) and *IRF1* (Fig. 3D) to test the miRNA-target interactions. HT22 cells were then transfected with individual reporters containing wild-type (WT) or mutant (Mut) UTRs together with an miR-301a mimic or a mimic control. The miR-301a mimic effectively reduced the luciferase activity of the WT UTR reporter compared to that in cells transfected with the mimic control. In contrast, the miR-301a–dependent reduction in luciferase activity was disrupted by mutating the 3′UTR binding sites in *SOCS5* (Fig. 3C) or *IRF1* (Fig. 3D). We further investigated whether the amounts of SOCS5 and IRF1 mRNAs and proteins were affected by the miR-301a mimic. Transfection of HT22 or SH-SY5Y cells with the miR-301a mimic substantially increased the abundance of miR-301a and subsequently attenuated the production of both SOCS5 and IRF1 proteins (Fig. 3E and fig. S3, A and B) but did not substantially affect their mRNA abundances (Fig. 3F). These results suggest that miR-301a suppressed the production of SOCS5 and IRF1 proteins by inhibiting translation rather than inducing mRNA degradation.

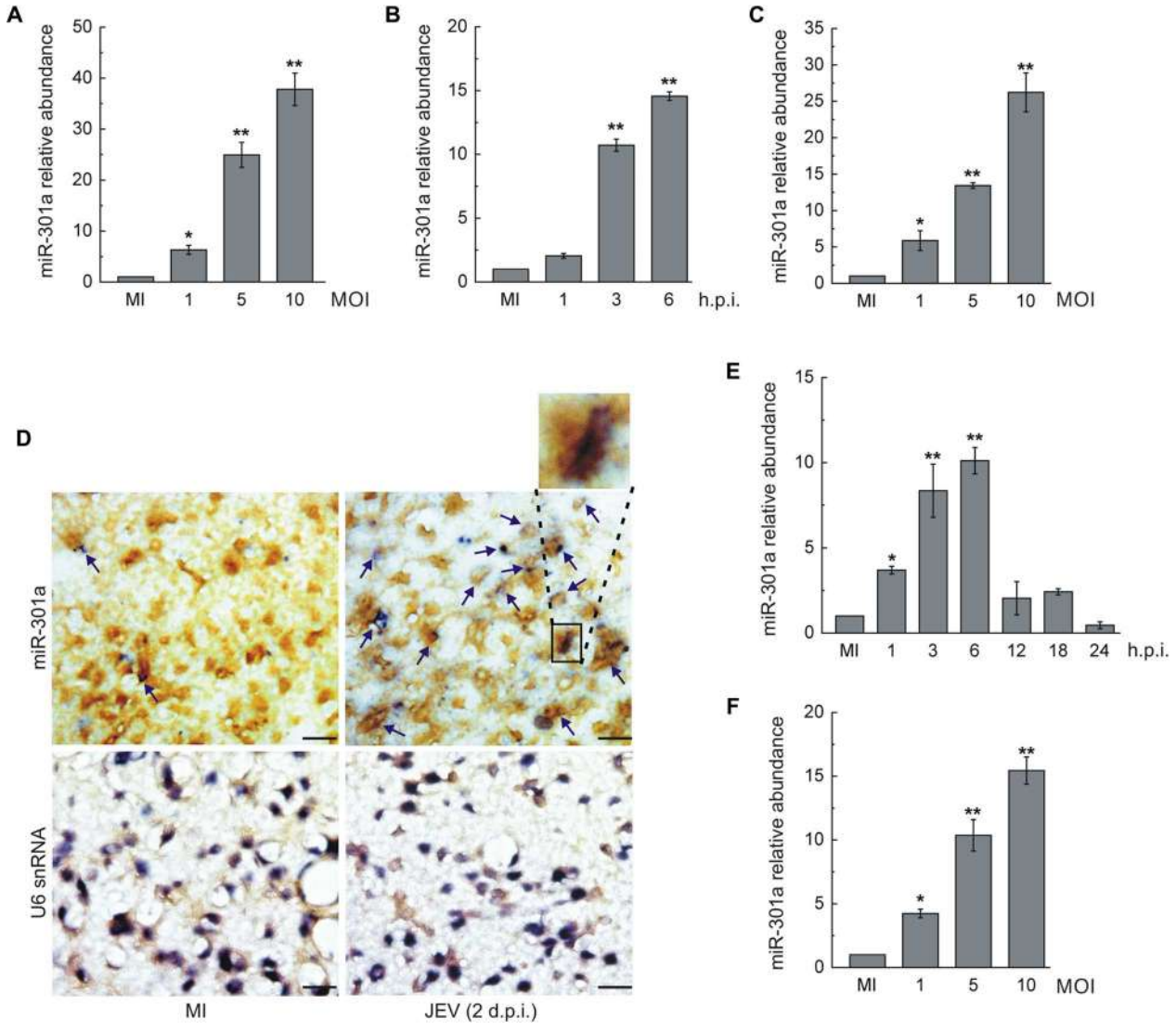

Fig. 1. *miR-301a* expression is induced early in JEV-infected neuronal cells. (**A**) HT22 cells were left uninfected (MI) or were infected with JEV at the indicated multiplicity of infections (MOIs) for 6 hours before the abundance of miR-301a was measured by qRT-PCR analysis and normalized to that of *SNORD68* snRNA. *$P < 0.05$, **$P < 0.01$ compared to uninfected cells. (**B** and **C**) Primary neuronal cells were isolated from postnatal day 0 (P0) to P2 BALB/c mouse pups, cultured for 7 days, and exposed to JEV for the indicated times (B) or were infected with JEV at the indicated MOIs for 6 hours (C). In both cases, miR-301a abundance was quantified by qRT-PCR analysis, and the results are expressed as the fold change compared to that in uninfected cells. *$P < 0.05$, **$P < 0.01$. (**D**) ISH of *miR-301a* (purple chromogen) in neuronal cells (brown chromogen) from mouse brain. Brain samples from P10 mice were collected from MI mice or from mice 2 days postinfection (d.p.i.) with JEV, and sections were hybridized with the miRCURY LNA miR-301a probe or the LNA U6 snRNA probe, which was followed by IHC analysis of neurons with DAB (3,3′-diaminobenzidine). Scale bars, 20 μm; magnification, ×40. The ubiquitously expressed U6 snRNA was used as a positive control for miRNA ISH. Data are representative of four mice per group. (**E**) SH-SY5Y cells were left uninfected (MI) or were exposed to JEV for the indicated times, and the abundance of miR-301a was evaluated by qRT-PCR analysis. *$P < 0.05$, **$P < 0.01$ compared to uninfected cells. (**F**) SH-SY5Y cells were left uninfected (MI) or were infected with JEV at the indicated MOIs for 6 hours. Relative miR-301a abundance was then determined by qRT-PCR analysis. *$P < 0.05$, **$P < 0.01$ compared to uninfected cells. h.p.i., hours postinfection. All data in bar graphs are means ± SD of three biological replicates. *P* values are calculated by analysis of variance (ANOVA) followed by Bonferroni's post hoc test.

miR-301a inhibits the production of SOCS5 and IRF1 proteins during JEV infection

We next examined whether miR-301a targeted SOCS5 and IRF1 during JEV infection. We cotransfected HT22 cells with either the miR-301a inhibitor or the inhibitor control together with either WT or mutant *SOCS5* or *IRF1* 3′UTR reporter constructs, which was followed by infection of the cells with JEV for 6 hours. We detected a substantial increase in luciferase activity in the cells transfected with the WT UTR construct and the miR-301a inhibitor (Fig. 4, A and B). In contrast, mutating the *SOCS5* and *IRF1* 3′UTRs blocked the anti–miR-301a–mediated increase in luciferase activity in these cells (Fig. 4, A and B). To present direct evidence that the miR-301a induced by JEV infection suppressed the production of SOCS5 and IRF1 proteins, we examined the abundances of SOCS5 and IRF1 in HT22 cells infected with JEV for different times as well as in HT22 cells infected for a fixed time with different viral concentrations, in which miR-301a was inhibited. We found that inhibition of miR-301a reconstituted SOCS5 and IRF1 protein production in JEV-infected cells compared to that in control cells (Fig. 4, C and D). Similarly, silencing of miR-301a in SH-SY5Y cells led to the restoration of SOCS5 and IRF1 protein production compared to that in control cells infected with JEV (fig. S4, A and B).

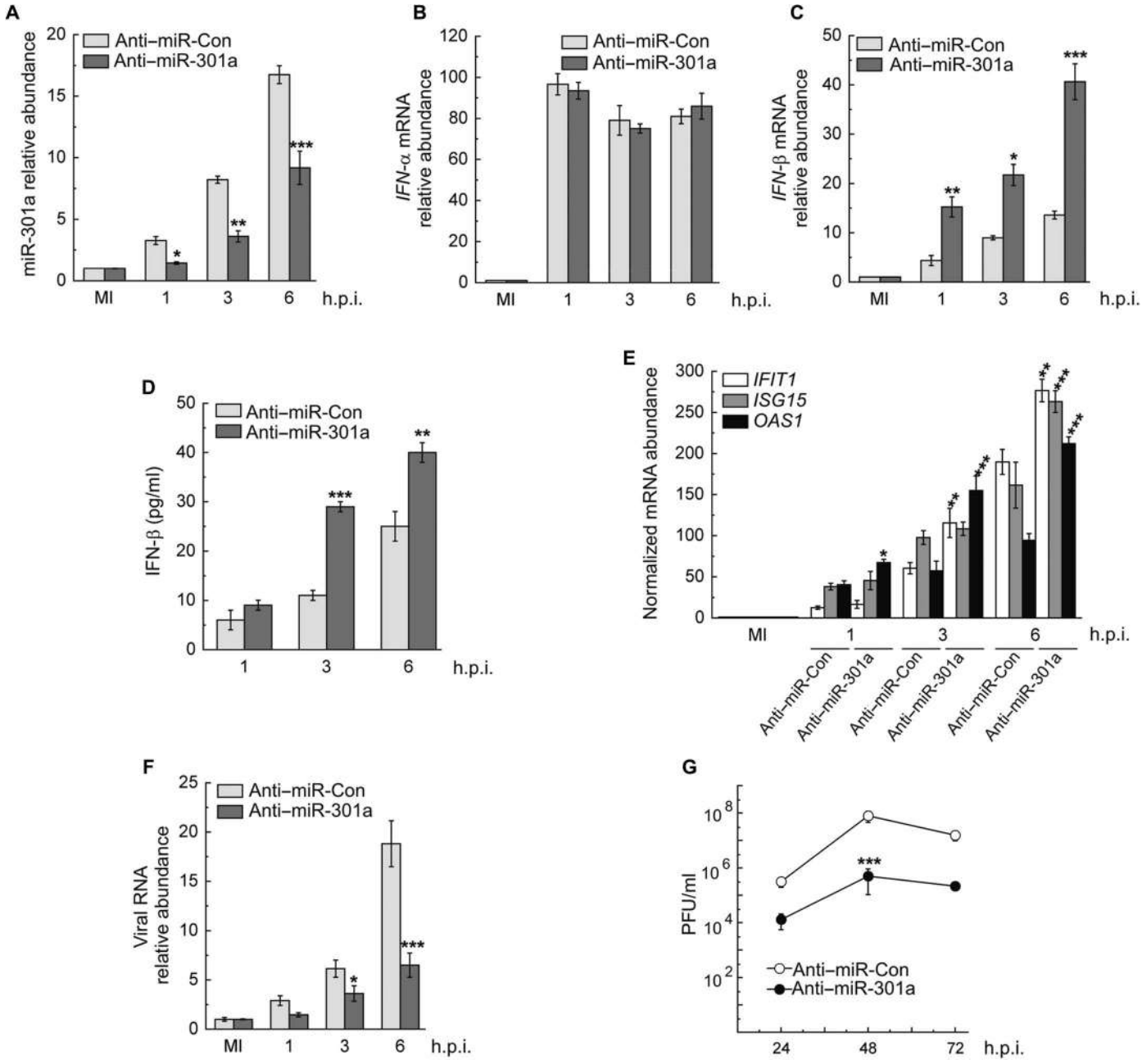

Fig. 2. miR-301a inhibits the antiviral IFN response and enhances viral replication. (**A**) HT22 cells transfected with an miR-301a inhibitor (anti–miR-301a) or a negative control (anti–miR-Con) were left uninfected (MI) or were infected with JEV for the indicated times. Relative miR-301a abundance was then determined by qRT-PCR analysis. $^{*}P < 0.05$, $^{**}P < 0.01$, $^{***}P < 0.001$ compared to the inhibitor control. (**B** and **C**) HT22 cells were transfected with the miR-301a inhibitor or the nonspecific inhibitor control. Twenty-four hours later, the cells were infected with JEV for the indicated times before the cells were subjected to qRT-PCR analysis of the relative abundances of *IFN*-α (B) and *IFN*-β (C) mRNAs. $^{*}P < 0.05$, $^{**}P < 0.01$, $^{***}P < 0.001$ compared to the inhibitor control. (**D**) Cell culture medium from the cells shown in (B) and (C) was analyzed by ELISA to determine the amount of secreted IFN-β protein. $^{**}P < 0.01$, $^{***}P < 0.001$ compared to the inhibitor control. (**E**) HT22 cells were transfected with the miR-301a inhibitor or the nonspecific inhibitor control. Twenty-four hours later, the cells were left uninfected (MI) or were infected with JEV for the indicated times before the cells were subjected to qRT-PCR analysis of the relative abundances of *IFIT1*, *ISG15*, and *OAS1* mRNAs. $^{*}P < 0.05$, $^{**}P < 0.01$, $^{***}P < 0.001$ compared to the inhibitor control. (**F**) HT22 cells were transfected with the miR-301a inhibitor or the nonspecific inhibitor control. Twenty-four hours later, the cells were infected with JEV for the indicated times before the cells were subjected to qRT-PCR analysis of the relative abundances of viral RNA. $^{*}P < 0.05$, $^{***}P < 0.001$ compared to the inhibitor control. (**G**) HT22 cells were transfected with the miR-301a inhibitor or the nonspecific inhibitor control. Twenty-four hours later, the cells were infected with JEV for the indicated times before the cell culture medium was collected for plaque assays, which were performed as described in Materials and Methods. $^{***}P < 0.001$ compared to the inhibitor control. All data are means ± SD of three biological replicates. *P* values were calculated by two-way ANOVA followed by the Holm-Sidak method.

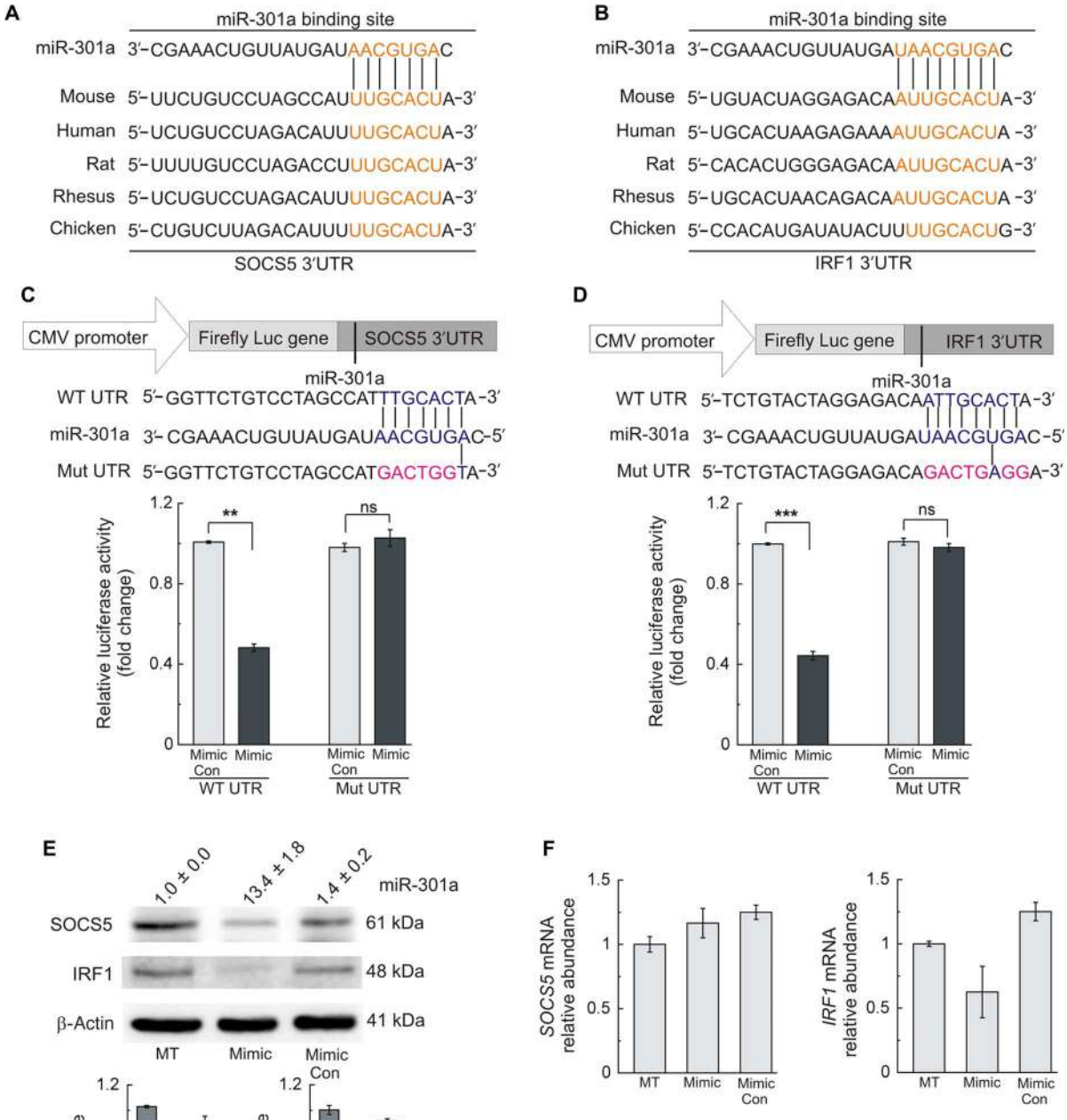

Fig. 3. *SOCS5* and *IRF1* are targets of miR-301a. (**A** and **B**) Predicted miR-301a binding sites in the 3′UTRs of *SOCS5* mRNA (A) and *IRF1* mRNA (B). Perfect matches in the seed regions are indicated in orange. (**C** and **D**) Top: Diagrams of constructs containing the 3′UTR of *SOCS5* (C) or *IRF1* (D) downstream of a luciferase reporter. The WT 3′UTR (WT UTR) contains an intrinsic miR-301a binding site, whereas the mutant 3′UTR (Mut UTR) contains mutations that eliminated the seed match with *miR-301a*. Mutations (magenta) in the 3′UTRs of both *SOCS5* and *IRF1* were generated for reporter gene assays. Bottom: Dual luciferase assays of HT22 cells cotransfected with firefly luciferase constructs containing the WT or mutant 3′UTRs of *SOCS5* (C) or *IRF1* (D) and either the miR-301a mimic (Mimic) or the control mimic (Mimic Con) were performed. Firefly luciferase activity was normalized to *Renilla* luciferase activity. Data are shown as the relative luciferase activity of cells transfected with the miR-301a mimic compared to that of cells transfected with the control mimic. Data are means ± SD of nine experiments from three independent transfections. $^{**}P < 0.01$, $^{***}P < 0.001$, by Student's *t* test. ns, not significant. (**E**) HT22 cells were subjected to mock transfection [mock-transfected (MT)] or were transfected with either the miR-301a miRNA mimic or the negative control mimic. Top: Twenty-four hours later, the cells were subjected to Western blotting analysis of the abundances of SOCS5 and IRF1 proteins. Bottom: Densitometric analysis of the Western blots from three experiments was performed to determine the fold changes in SOCS5 and IRF1 protein abundance (normalized to that of β-actin) relative to the MT cells. The relative abundance of miR-301a as determined by qRT-PCR analysis of each set of cells is shown above the blots to confirm effective transfection. Data are means ± SD of three independent experiments. $^{***}P < 0.001$, by one-way ANOVA followed by Bonferroni's post hoc test. (**F**) HT22 cells were left untransfected (MI) or were transfected with either the miR-301a mimic or the negative control mimic. Twenty-four hours later, the cells were subjected to qRT-PCR analysis of the relative abundances of *SOCS5* and *IRF1* mRNAs. Data are means ± SD of three independent experiments. Statistical analysis of the data by one-way ANOVA with Bonferroni's multiple comparisons showed that there were no statistically significant differences.

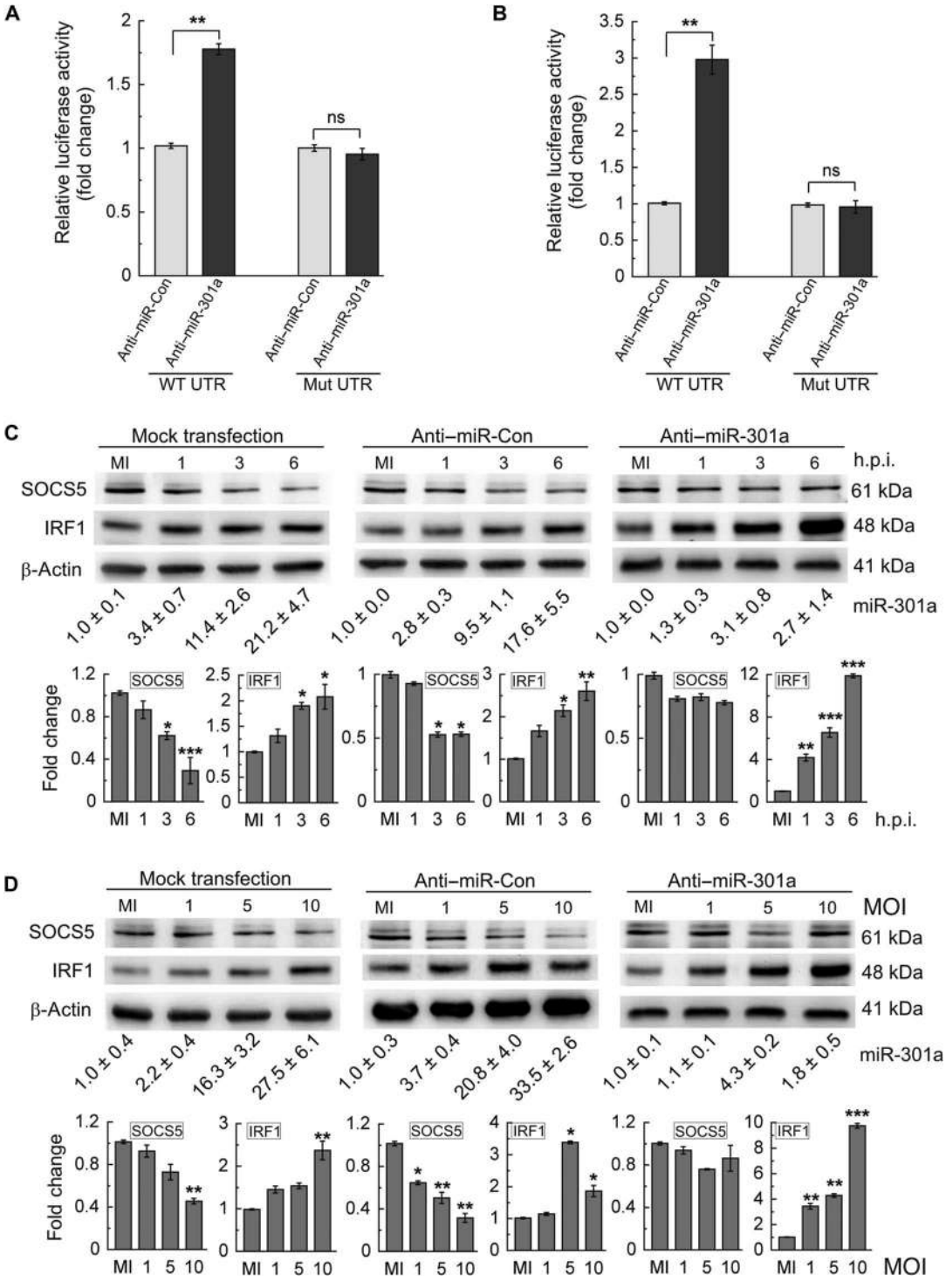

Fig. 4. JEV-induced miR-301a suppresses SOCS5 and IRF1 protein production. (**A** and **B**) HT22 cells were cotransfected with either the miR-301a inhibitor (anti–miR-301a) or the inhibitor control (anti–miR-Con) together with a firefly luciferase reporter plasmid encoding the WT or mutant 3′UTRs of *SOCS5* (A) or *IRF1* (B). Twenty-four hours later, the cells were infected with JEV for 6 hours before luciferase activities were measured with a dual luciferase assay kit and normalized to that of *Renilla* luciferase. Data are expressed as the relative luciferase activity of the anti–miR-301a–transfected cells compared to that of the anti–miR-Con–transfected cells. Data are means ± SD of nine experiments from three independent transfections. $^{**}P < 0.01$, by Student's *t* test. (**C** and **D**) HT22 cells were transfected with either the miR-301a inhibitor or the inhibitor control and then were either infected with JEV at an MOI of 5 for the indicated times (C) or infected for 6 hours with JEV at the indicated MOIs (D). Top: The cells were analyzed by Western blotting to determine the relative abundances of SOCS5 and IRF1 proteins. β-Actin was used as a loading control. Western blots are representative of three independent experiments. The relative abundance of miR-301a in each set of cells was determined by qRT-PCR analysis and is shown below the blots to confirm effective transfection. Bottom: Densitometric analysis of the Western blots was performed to determine the fold changes in the indicated protein abundances (normalized to that of β-actin) in infected cells compared to those in uninfected (MI) cells. Data are means ± SD of three individual experiments. $^{*}P < 0.05$, $^{**}P < 0.01$, $^{***}P < 0.001$, by one-way ANOVA followed by Bonferroni's post hoc test.

miR-301a hampers the JEV-induced production of type I IFN by suppressing *SOCS5* and *IRF1* mRNA translation

To validate the roles of SOCS5 and IRF1 in the anti-IFN action of miR-301a, we performed experiments in which SOCS5 or IRF1 were knocked down or overexpressed. HT22 cells were cotransfected with the miR-301a inhibitor and with Con-esiRNA [control (Con) endoribonuclease-prepared small interfering RNA (siRNA) (esiRNA)] or esiRNAs specific for SOCS5 and IRF1 alone or in combination before being infected 24 hours later with JEV for 6 hours. The induction in expression of *IFN*-β and the ISGs *IFIT1*, *ISG15*, and *OAS1* by the miR-301a inhibitor observed in Con-esiRNA–transfected cells was disrupted by the knockdown of SOCS5, IRF1, or both (Fig. 5, A to D). Consequently, the decrease in viral RNA caused by miR-301a inhibition was restored by knockdown of both SOCS5 and IRF1 (Fig. 5E).

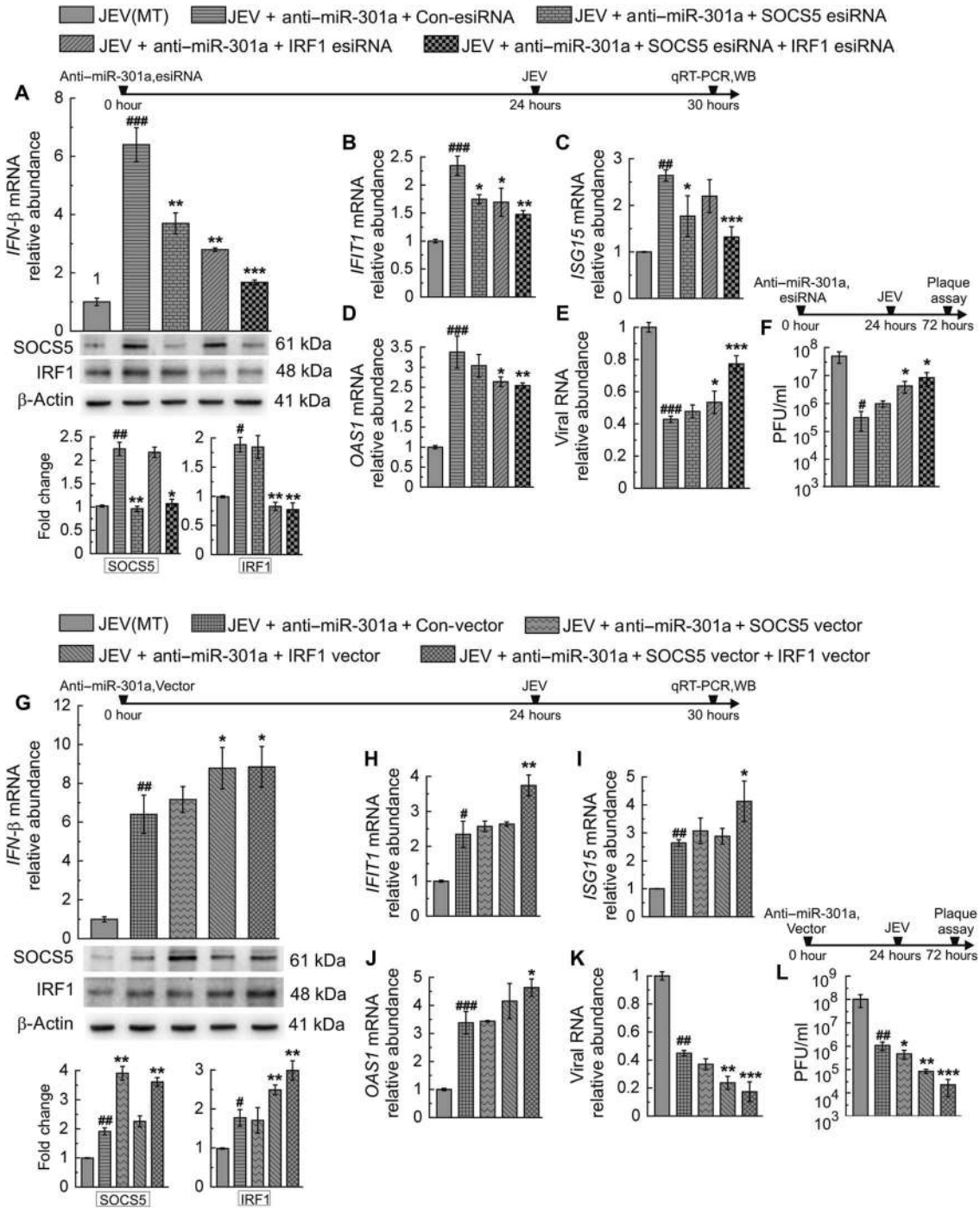

Fig. 5. miR-301a inhibits the IFN response by repressing SOCS5 and IRF1 protein production. (**A** to **E**) HT22 cells were left untransfected (MT) or were transfected with anti–miR-301a together with Con-esiRNA or esiRNAs specific for SOCS5 or IRF1 alone or in combination before being infected with JEV at an MOI of 5. Six hours after infection, the relative abundances of *IFN*-β (A), *IFIT1* (B), *ISG15* (C), *OAS1* (D) mRNAs, and viral RNA (E) were quantified by qRT-PCR analysis. (A) Cells were also subjected to Western blotting (WB) analysis of SOCS5 and IRF1 abundances to confirm effective transfection of the cells. Bar graphs show densitometric analysis of the fold changes in the abundance of the indicated proteins (normalized to that of β-actin) compared to that in the MT, JEV-infected cells. $^{\#\#}P < 0.01$, $^{\#\#\#}P < 0.001$ compared to MT cells; $^{*}P < 0.05$, $^{**}P < 0.01$, $^{***}P < 0.001$ compared to cells transfected with anti–miR-301a and Con-esiRNA. (**F**) HT22 cells transfected as described in (A) to (E) were infected with JEV for 48 hours before the culture medium was collected for plaque assays. Data are means ± SD of three independent experiments. $^{\#}P < 0.05$ compared to MT cells; $^{*}P < 0.05$ compared to cells transfected with anti–miR-301a and Con-esiRNA. (**G** to **K**) HT22 cells were left untransfected (MT) or were transfected with the indicated combinations of plasmids and anti–miR-301a. Twenty-four hours later, the cells were infected with JEV at an MOI of 5. At 6 hours after infection, the relative abundances of *IFN*-β (G), *IFIT1* (H), *ISG15* (I), and *OAS1* (J) mRNAs, and of viral RNA (K) were measured by qRT-PCR analysis. (G) Cells were also subjected to Western blotting analysis of SOCS5 and IRF1 abundances to confirm effective transfection of the cells. Bar graphs show densitometric analysis of the fold changes in the abundance of the indicated proteins (normalized to that of β-actin) compared to that in the MT, JEV-infected cells. $^{\#}P < 0.05$, $^{\#\#}P < 0.01$, $^{\#\#\#}P < 0.001$ compared to untransfected cells (MT); $^{*}P < 0.05$, $^{**}P < 0.01$, $^{***}P < 0.001$ compared to cells transfected with anti–miR-301a and Con-vector. (**L**) HT22 cells that were transfected as described in (G) to (K) were infected with JEV for 48 hours before the culture medium was collected for plaque assays. Data are means ± SD of three independent experiments. $^{\#\#}P < 0.01$ compared to untransfected cells (MT); $^{*}P < 0.05$, $^{**}P < 0.01$, $^{***}P < 0.001$ compared to cells transfected with anti–miR-301a and Con-vector. *P* values were calculated by one-way ANOVA followed by Bonferroni's post hoc test.

The viral titer in the cell culture medium of HT22 cells transfected with anti–miR-301a was increased by the concomitant knockdown of either SOCS5 or IRF1 (Fig. 5F). In contrast, transfection of miR-301a inhibitor–treated HT22 cells with plasmids encoding SOCS5 or IRF1 alone or in combination followed by infection with JEV enhanced the expression of *IFN*-β and the ISGs compared to cells cotransfected with

the control vector (Con-vector) (Fig. 5, G to J). Accordingly, the impairment of viral replication caused by miR-301a inhibition was augmented by overexpression of SOCS5 or IRF1 (Fig. 5K). The viral titer in the culture medium of cells overexpressing SOCS5, IRF1, or both was also reduced compared to that for cells transfected with Con-vector (Fig. 5L). Thus, the miR-301a induced upon JEV infection exhibited its viral-promoting function mainly through the suppression of *SOCS5* and *IRF1* expression and the subsequent reduced IFN response.

Reduction in SOCS5 leads to epidermal growth factor receptor activation and inhibits IRF1

IRF1 is a potential regulator of the antiviral IFN response (*41*), but little is known about the role of SOCS5 in antiviral innate immunity. Therefore, the function of SOCS5 in the miR-301a–mediated suppression of IFN-β production in JEV-infected HT22 cells was investigated. First, we found that SOCS5 protein abundance in JEV-infected cells was substantially reduced up to 24 hours after infection (Fig. 6A). We also confirmed a decrease in SOCS5 protein abundance in JEV-infected mouse brain and primary neurons by immunofluorescence analysis (fig. S5, A and B). Because SOCS proteins are potential regulators of IRF signaling (*42*), we evaluated whether suppression of SOCS5 during JEV infection might have any effect on *IRF1* expression. We found that transfection of cells with SOCS5-specific esiRNA reduced *IRF1* expression compared to JEV-infected HT22 cells transfected with control esiRNA (Fig. 6B). Conversely, overexpression of exogenous SOCS5 substantially rescued *IRF1* expression in cells after infection with JEV (Fig. 6C).

SOCS5 inhibits epidermal growth factor receptor (EGFR) signaling (*43*), and active, phosphorylated EGFR (p-EGFR) inhibits the

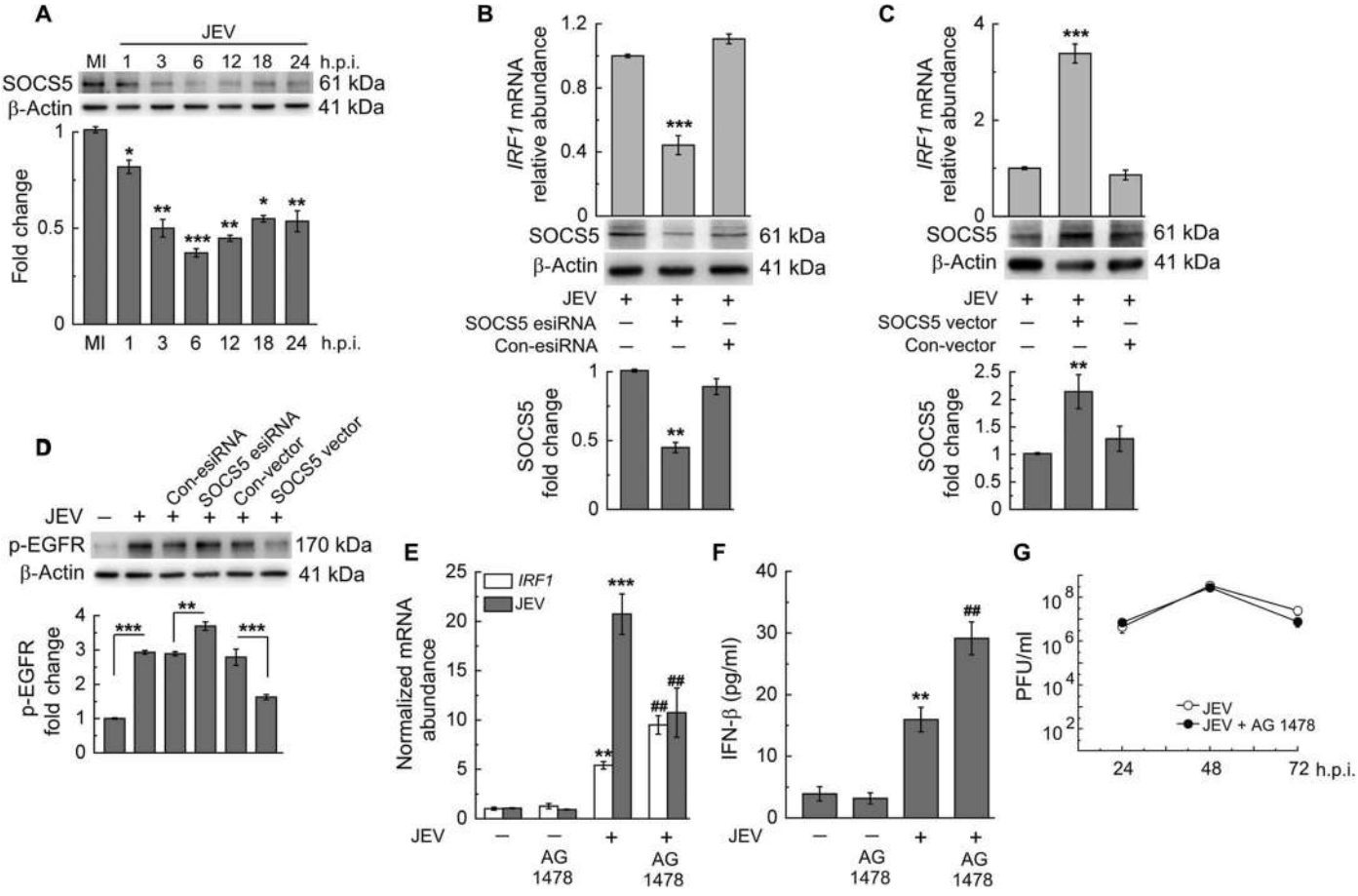

Fig. 6. Loss of SOCS5 facilitates the suppression of IRF1 production through EGFR activation. (**A**) HT22 cells were left uninfected (MI) or were infected with JEV at an MOI of 5 for 24 hours. Top: Cells were analyzed by Western blotting with antibodies against the indicated proteins. Bottom: Densitometric analysis was performed to show the fold change in SOCS5 protein abundance (normalized to that of β-actin) in infected cells compared to that in uninfected cells (MI). $^{*}P < 0.05$, $^{**}P < 0.01$, $^{***}P < 0.001$ compared to uninfected cells. (**B** and **C**) HT22 cells were left untransfected or were transfected with either SOCS5-specific or Con-esiRNA (B) or with either the SOCS5 expression plasmid or the control plasmid (C). Top: Twenty-four hours later, the cells were infected with JEV for 6 hours before the relative abundance of *IRF1* mRNA was quantified by qRT-PCR analysis. $^{***}P < 0.001$ compared to untransfected cells. Bottom: Transfection efficiency was determined by Western blotting analysis of SOCS5 abundance. Histograms show the densitometric analysis of the fold change in SOCS5 protein abundance (normalized to that of β-actin) in transfected cells compared to that in untransfected cells. $^{**}P < 0.01$ compared to untransfected cells. (**D**) HT22 cells were left untransfected or were transfected with the indicated esiRNAs or expression plasmids before being infected with JEV for 6 hours. Top: Samples were then analyzed by Western blotting with antibodies against the indicated proteins. Equivalent gel loading was confirmed by analysis with an antibody against β-actin. Bottom: Densitometric quantification of the abundance of p-EGFR normalized to that of β-actin. $^{**}P < 0.01$, $^{***}P < 0.001$. (**E** and **F**) HT22 cells were treated with 10 μM AG 1478 or vehicle before being left uninfected of infected with JEV for 6 hours. The relative abundance of *IRF1* mRNA and viral RNA were analyzed by qRT-PCR (E). $^{**}P < 0.01$, $^{***}P < 0.001$ compared to untreated control cells; $^{\#\#}P < 0.01$ compared to JEV-infected cells. In addition, the amount of IFN-β secreted by the indicated cells was measured by ELISA (F). $^{**}P < 0.01$ comparison to untreated control cells; $^{\#\#}P < 0.01$ compared to JEV-infected cells. (**G**) HT22 cells treated with or without 10 μM AG 1478 were infected with JEV for the indicated times before the culture medium was collected for plaque assays. All data are means ± SD of three biological replicates. *P* values were obtained by one-way ANOVA followed by Bonferroni's multiple comparisons.

IRF1-dependent antiviral IFN response (*44*). Therefore, to investigate the mechanism underlying the SOCS5-mediated regulation of IRF1, we investigated the effect of SOCS5 on p-EGFR abundance in JEV-infected HT22 cells. EGFR activation in JEV-infected cells was further enhanced when SOCS5 was knocked down, whereas SOCS5 overexpression markedly reduced the abundance of p-EGFR (Fig. 6D), which suggests that JEV activates EGFR by suppressing SOCS5 in neuronal cells. Furthermore, to assess whether EGFR activation suppressed *IRF1* expression, we treated JEV-infected HT22 cells with a selective EGFR tyrosine kinase inhibitor, AG 1478. We found that *IRF1* mRNA abundance in JEV-infected cells was increased to a greater extent in the presence of AG 1478 than in cells infected with JEV alone; however, AG 1478 substantially decreased the abundance of viral RNA (Fig. 6E). In addition, AG 1478 increased the amount of IFN-β secreted by JEV-infected cells (Fig. 6F). The viral titer in the culture medium of AG 1478–treated, JEV-infected cells was similar to that in the culture medium of cells infected with JEV alone (Fig. 6G). Together, these data suggest that the miR-301a–mediated reduction in SOCS5 abundance during JEV infection leads to EGFR activation, which then represses the IRF1-mediated production of IFN-β.

miR-301a expression is induced through an nuclear factor κB–dependent mechanism

We next investigated the underlying mechanism by which *miR-301a* expression is enhanced during JEV infection. The human *miR-301a* promoter has a binding site for RelA, and nuclear factor κB (NF-κB) activation promotes *miR-301a* expression (*33*). Here, we examined the time-dependent activation of NF-κB and found that JEV infection increased the amounts of the phosphorylated forms of p65, IκBα, and IKKα/β in HT22 (Fig. 7, A and B) and SH-SY5Y (fig. S6, A and B) cells up to 6 hours after infection. Hence, we used bioinformatics to investigate the binding sites for RelA in the promoter region of mouse *miR-301a*. The *miR-301a* gene in the mouse resides on chromosome 11: 86920763 to 86924763 (+), within the first intron of a ~15-kb mRNA transcript of spindle and kinetochore-associated protein 2 (Ska2). Using the PROMO software (*45*), a search engine that identifies transcription factor binding sites in DNA sequences from a given species, we analyzed the regions 1.5 kb upstream and 0.3 kb downstream of the transcription start site (TSS) of *Ska2*. Binding sites for more than 15 transcription factors were predicted (table S2). Among these, we identified a putative RelA binding site within a CpG island upstream of the TSS (1169 to 1178) (Fig. 7C).

To confirm whether this DNA fragment was a functional promoter and that the binding site was genuine, we cloned the 1.8-kb DNA sequence into a luciferase reporter plasmid and further prepared a construct containing a mutation in the RelA binding site within this promoter region. HT22 cells were transfected separately with plasmids encoding the WT or mutant reporter constructs, and we observed a minor difference in luciferase activity between cells expressing the WT or mutant reporters (Fig. 7D). However, ectopic expression of p65 in cells expressing the WT reporter construct substantially enhanced the transcriptional activity of the *miR-301a* promoter and induced luciferase expression, suggesting that this fragment is an active promoter with an authentic RelA binding site (Fig. 7D). Furthermore, we transfected cells with the WT or mutant *miR-301a* promoter constructs before infecting the cells with JEV to analyze whether NF-κB activation stimulated promoter activity as a response to JEV infection. Although there was a substantial increase in luciferase activity in cells expressing the WT construct, mutation of the RelA binding site substantially reduced promoter activity during the first 6 hours of JEV infection (Fig. 7E). This result suggests that the JEV-induced activation of NF-κB increased *miR-301a* expression.

Next, we investigated whether the activation of NF-κB suppressed SOCS5 and IRF1 during JEV infection. To address this issue, we introduced ammonium pyrrolidinedithiocarbamate (PDTC) into HT22 cells before viral infection to block the activation of NF-κB and its translocation to the nucleus, where it could bind to the *miR-301a* promoter and induce expression. The abundance of p-p65 in the nucleus of JEV-infected cells was reduced in response to PDTC; however, PDTC had no effect on the abundance of p-p65 in the cytoplasm (Fig. 7, F and G). PDTC inhibited NF-κB translocation, and miR-301a abundance was partially reduced during JEV infection (Fig. 7F). Furthermore, the abundances of SOCS5 and IRF1 proteins were restored in JEV-infected HT22 cells treated with PDTC (Fig. 7, F and G). Similar results were observed in PDTC-treated SH-SY5Y cells in response to JEV infection (fig. S6, C and D). Next, we performed a ChIP assay with lysates of uninfected or JEV-infected HT22 cells to further verify the binding of endogenous RelA to the putative binding site in the *miR-301a* promoter. We found that JEV infection resulted in the recruitment of NF-κB to the putative *miR-301a* promoter, which did not occur in uninfected cells, as determined by the increased abundance of miR-301a by PCR and qRT-PCR analysis (Fig. 7, H to J). Together, these results suggest that JEV infection leads to the activation of NF-κB, which then binds to the *miR-301a* promoter to facilitate its expression.

Mice treated with a miR-301a Vivo-Morpholino are protected from JEV infection

Morpholino oligomers are a proven antisense reagent used to block mRNA translation or interfere with RNA processing, including splicing and miRNA maturation. To evaluate the effect of miR-301a inhibition on the production of type I IFN in vivo, we designed a Vivo-Morpholino to specifically target the seed sequence of miR-301a (miR-301a-VM) and an appropriate negative control (VM-NC) in which five nucleotides of the seed sequence were mutated (Fig. 8A). The Vivo-Morpholino system provides effective delivery of morpholino antisense oligomers into a wide range of tissues in live mice (*46*). Because the efficiency of Vivo-Morpholino delivery into the brain through the intravenous or intraperitoneal route is quite low, mice were initially injected intracranially with sequentially increasing amounts of miR-301a-VM for dose standardization. We observed a substantial reduction in endogenous *miR-301a* expression in mice treated with miR-301a-VM doses of ≥16 mg/kg body weight (fig. S7A). However, at doses >18 mg/kg, the mice exhibited decreased survival and lost weight (fig. S7, B and C), indicating that when administered above this dose, miR-301a-VM resulted in toxicity. Next, we administered miR-301a-VM (intracranially) into WT mice at a dose of 18 mg/kg 12, 24, or 48 hours after the mice were infected intraperitoneally with JEV and monitored the mice for clinical symptoms daily. Treatment with miR-301a-VM at 12 or 24 hours after infection improved the survival percentage (60 and 20%, respectively) of the mice as compared with the survival of the mice treated with VM-NC (Fig. 8B). Furthermore, the percentage of paralyzed mice and the degree of body weight loss were substantially reduced in the mice treated with miR-301a-VM 12 or 24 hours after infection (fig. S7, D and E) compared to those of mice treated with VM-NC. Thus, miR-301a-VM not only improved survival but also lessened disease severity in the CNS.

In another set of experiments, the mice were left uninfected or were infected with JEV and treated with VM-NC (18 mg/kg) or miR-301a-VM at 12, 24, and 48 hours after infection and then were left for another 24 hours, at which point brain samples were collected. Although mice

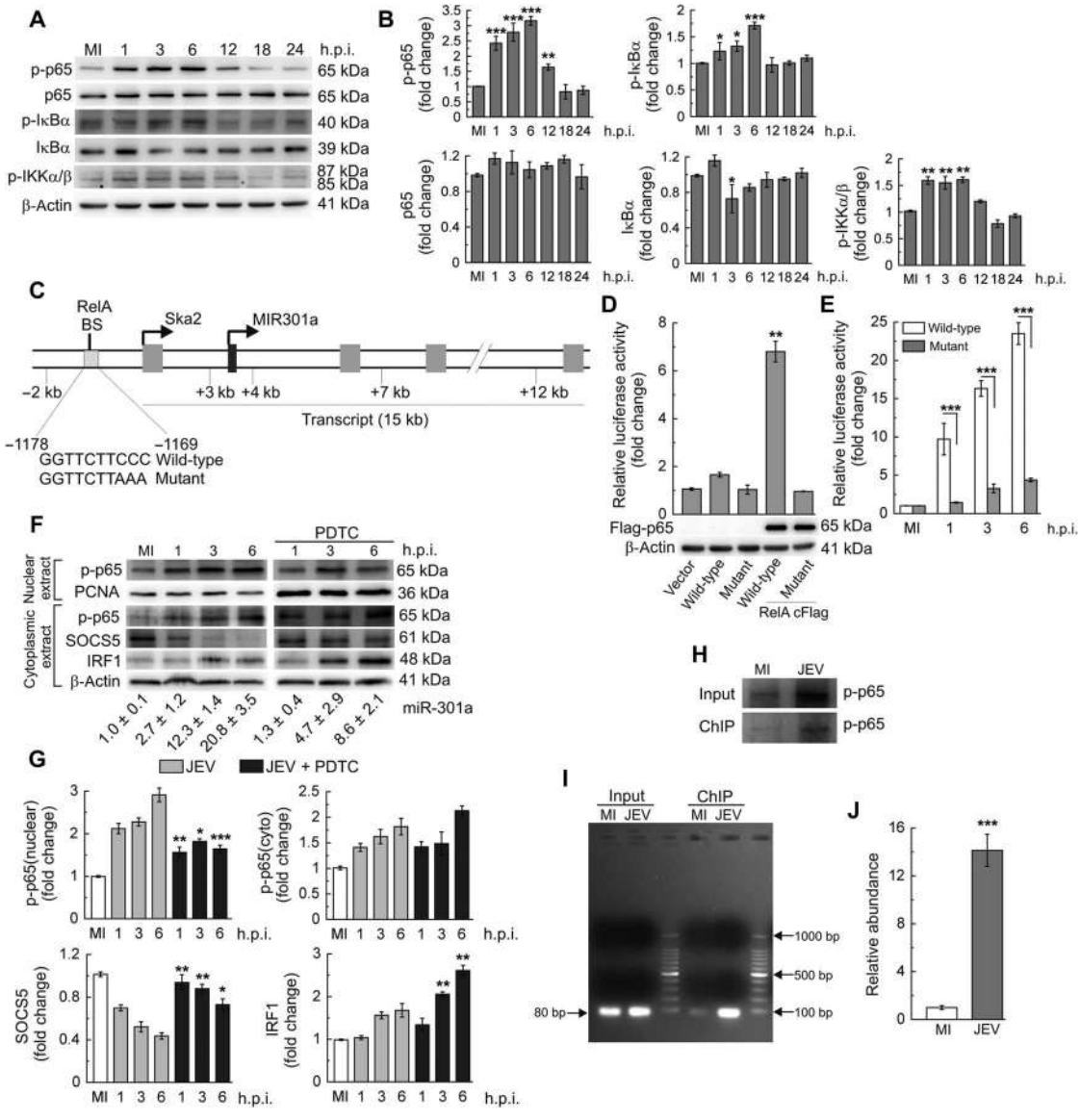

Fig. 7. JEV induces *miR-301a* expression through the activation of NF-κB. (**A**) HT22 cells were left uninfected (MI) or were infected with JEV at an MOI of 5 for the indicated times. Cells were then analyzed by Western blotting with antibodies specific for the indicated proteins. β-Actin served as a loading control. Western blots are representative of three independent experiments. (**B**) Densitometric analysis of the indicated bands in the Western blots shown in (A). Fold changes in the abundance of the indicated proteins (normalized to that of β-actin) are shown relative to those in uninfected cells. Data are means ± SD of three separate experiments. $^{*}P < 0.05$, $^{**}P < 0.01$, $^{***}P < 0.001$ compared to uninfected cells. Data were analyzed by one-way ANOVA followed by Bonferroni's post hoc test. (**C**) Schematic representation of the predicted RelA binding site in the *miR-301a* promoter region within the host gene *Ska2*. The WT sequence GGTTCTTCCC in the *miR-301a* promoter was replaced by GGTTCTTAAA to generate the mutant construct. (**D**) Top: HT22 cells were transfected with either the WT or mutant *miR-301a* promoter construct alone or together with plasmid encoding Flag-tagged RelA (RelA cFlag pcDNA3). Twenty-four hours later, promoter activity was analyzed by dual luciferase assay. Firefly luciferase activity was normalized to *Renilla* luciferase activity, and the fold change in luciferase activity compared to that in cells transfected with the empty plasmid pGL3 was determined. Data are means ± SD of nine experiments from three independent transfections. $^{**}P < 0.01$ compared to plasmid control, by one-way ANOVA with Bonferroni's corrections. Bottom: Transfection efficiency was determined by Western blotting analysis of Flag-p65 abundance. (**E**) HT22 cells were transfected with the WT or mutant *miR-301a* promoter reporter. Six to 8 hours later, the cells were left uninfected or were infected with JEV at an MOI of 5 for the indicated times before luciferase assays were performed. The relative luciferase activity of the mutant reporter compared to that of the WT reporter after normalization to *Renilla* luciferase was determined. Data are means ± SD nine experiments from three independent transfections. $^{***}P < 0.001$ by two-way ANOVA followed by the Holm-Sidak method. (**F**) HT22 cells pretreated with or without 50 μM PDTC were left uninfected or were infected with JEV for 6 hours. Nuclear and cytoplasmic fractions of the cells were then isolated and analyzed by Western blotting with antibodies specific for the indicated proteins. PCNA and β-actin served as loading controls for the nuclear and cytoplasmic extracts, respectively. Values below the blots show miR-301a abundance in the corresponding samples as determined by qRT-PCR analysis. (**G**) Densitometric analysis of the indicated bands in the Western blots shown in (F). The fold changes in the abundance of the indicated proteins (normalized to that of the appropriate loading control) compared to those in uninfected control cells were determined. Data are means ± SD of three biological replicates. $^{*}P < 0.05$, $^{**}P < 0.01$, $^{***}P < 0.001$ compared to JEV-infected, untreated cells, as analyzed by one-way ANOVA followed by Bonferroni's post hoc test. (**H** to **J**) HT22 cells were left uninfected or were infected with JEV at an MOI of 5 for 6 hours before being subjected to chromatin immunoprecipitation (ChIP) assay with an anti–p-p65 antibody to measure recruitment to the *miR-301a* promoter. The nuclear extract before treatment with antibody served as input. (I) PCR analysis of the DNA isolated by ChIP compared to input DNA with primers flanking the RelA binding site in the predicted *miR-301a* promoter region. (J) The relative abundance of the *miR-301a* promoter fragment in the indicated samples, normalized to that in the input, was determined by qRT-PCR analysis. $^{***}P < 0.001$ compared to the uninfected cells, as determined by Student's *t* test. Data are means ± SD of three independent experiments, each with triplicate measurements.

treated with VM-NC showed a substantial increase in miR-301a abundance in response to infection compared to uninfected mice, this enhancement was markedly reduced in the mice treated with miR-301a-VM (Fig. 8C). Because of the increased survival of miR-301a-VM–treated mice compared to VM-NC–treated mice, we measured the titers of JEV in the mouse brains. Both plaque and qRT-PCR assays showed that there was a substantial reduction in viral load in the miR-301a-VM–treated mice, which suggested that viremia was restricted because of the

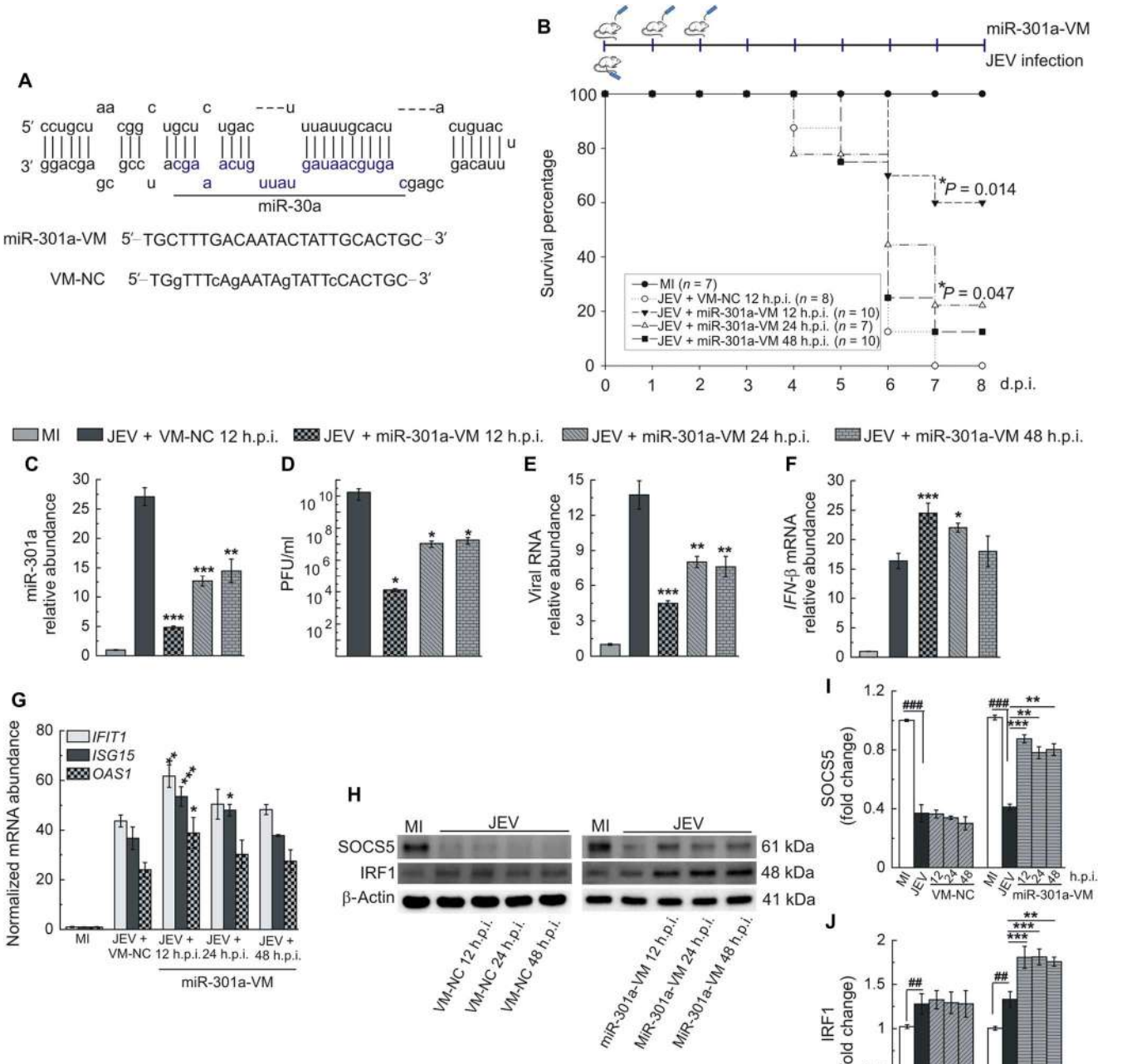

Fig. 8. Inhibition of *miR-301a* in vivo restores the IFN response and improves survival in JEV-infected mice. (**A**) Stem-loop sequence of pre–miR-301a. Bottom: Sequences of the miR-301a Vivo-Morpholino (miR-301a-VM), which targets mature *miR-301a* (blue), and a scrambled Vivo-Morpholino that was designed as a negative control (VM-NC). (**B**) BALB/c mice were intracranially treated with miR-301a-VM or VM-NC (18 mg/kg) at the indicated times after they were infected with JEV (3×10^5 PFU) and then were observed daily to determine their survival rate. The asterisk represents comparison between the JEV/VM-NC group versus the JEV/miR-301a-VM 12 h.p.i. and JEV/miR-301a-VM 24 h.p.i. groups. *P* values were determined by one-way ANOVA followed by Bonferroni's post hoc test. (**C**) Brain samples from the mice shown in (B) were collected on day 3 (72 h.p.i.) of infection, and their abundance of miR-301a was quantified by qRT-PCR analysis. Data are represented as the fold change in miR-301a abundance (normalized to that of *SNORD68*) in the infected samples relative to that in the uninfected samples. Data are means ± SD of four mice from each group. $^{**}P < 0.01$, $^{***}P < 0.001$ compared to the JEV + VM-NC group, as analyzed by one-way ANOVA followed by Bonferroni's multiple comparisons. (**D**) Viral loads in the brain tissues of the mice shown in (B) were evaluated by plaque assay in porcine kidney cells. Plaque assays were performed twice, and the data are means ± SD of three mice from each group. $^{*}P < 0.05$ when compared to the JEV + VM-NC group, as determined by one-way ANOVA with Bonferroni's correction. (**E** to **G**) Mice were left uninfected or were infected with JEV in the presence of VM-NC or were infected with JEV and treated with miR-301a-VM at the indicated times. Three days after infection, brains were collected from the mice and analyzed by qRT-PCR to determine the abundances of viral RNA (E), *IFN*-β mRNA (F), and *IFIT1*, *ISG15*, and *OAS1* mRNAs (G). Data are means ± SD of four mice from each group. $^{*}P < 0.05$, $^{**}P < 0.01$, $^{***}P < 0.001$ when compared to the VM-NC group. Data were analyzed by one-way ANOVA followed by Bonferroni's post hoc test. (**H**) Brain samples from the mice described in (E) to (G) were analyzed by Western blotting with antibodies specific for SOCS5 and IRF1. β-Actin served as loading control. Blots are representative of four mice from each group. (**I** and **J**) Densitometric analysis of the blots shown in (H). The histograms show the fold changes in SOCS5 (I) and IRF1 (J) protein abundance (normalized to that of β-actin) in infected samples compared to those in uninfected samples. Data are means ± SD of four mice from each group. $^{\#\#}P < 0.01$, $^{\#\#\#}P < 0.001$, $^{**}P < 0.01$, $^{***}P < 0.001$, as calculated by one-way ANOVA followed by Bonferroni's multiple comparisons.

inhibition of miR-301a in the JEV-infected mice (Fig. 8, D and E). To determine whether the reduction in viremia was caused by the IFN response, we evaluated the expression of *IFN*-β and various ISGs. We found that all of these mRNAs were substantially increased in abundance in the mice treated with miR-301a-VM 12 and 24 hours after infection compared to those in the VM-NC–treated mice (Fig. 8, F and G). As expected, the suppression of SOCS5 and IRF1 protein production in the VM-NC–treated, JEV-infected mice was partially restored in the JEV-infected mice treated with miR-301a-VM (Fig. 8, H to J). Thus, these data suggest that the inhibition of *miR-301a* expression in vivo improved the survival of the JEV-infected mice by inducing the type I IFN response to inhibit viral propagation.

JEV infection of peripheral organs has no effect on *miR-301a* expression

Although JEV is neurotropic, it also infects some peripheral tissues before invading the CNS. To explore whether miR-301a might regulate JEV infection in peripheral tissues, we infected liver (HepG2) and kidney [human embryonic kidney–293 (HEK 293)] cell lines with JEV and then analyzed the cells for NF-κB activation and the expression of *miR-301a*, *IFN*-β, *IFIT1*, and *ISG15*, as well as the generation of SOCS5 and IRF1 proteins, at various times. We found that JEV infection did not induce substantial increases in miR-301a abundance in either cell type (fig. S8A); however, NF-κB was activated up to 6 hours after infection (fig. S8, B and C). Consequently, no changes in the abundances of SOCS5 and IRF1 proteins were observed in JEV-infected cells transfected with anti–miR-301a compared to those in JEV-infected cells transfected with the negative control (anti–miR-Con) (fig. S8, D and E). Furthermore, the effect of the inhibitor on the JEV-induced expression of *IFN*-β and ISGs in HepG2 and HEK 293 cells was examined. The abundances of *IFN*-β and ISG mRNAs were equivalent in inhibitor- and control inhibitor–treated cells (fig. S8, F and G); thus, JEV replication was not inhibited in either cell type, as evident from the measurement of viral RNA and titers (fig. S8, H and I). Consistent with these data, liver and kidney samples taken from JEV-infected mice had similar amounts of miR-301a to those from uninfected mice (fig. S9A). For further confirmation, we injected JEV-infected mice with miR-301a-VM or VM-NC intraperitoneally at various times and then collected liver and kidney samples after 72 hours. The amounts of *IFN*-β mRNA and viral RNA in the miR-301a-VM–treated, JEV-infected mice were similar to those in the VM-NC–treated infected mice (fig. S9, B and C). These results suggest that the NF-κB–mediated induction of *miR-301a* expression and the suppression of SOCS5 and IRF1 production are not ubiquitous mechanisms in the livers and kidneys of JEV-infected mice.

DISCUSSION

Upon viral infection, host innate immunity is the first line of antiviral defense, which is tasked with the recognition of viral components and the production of proinflammatory cytokines and type I IFNs (*47*–*49*). Neuronal innate immunity in flaviviral infection, including that by JEV, is critical because of the neurotropic nature of these viruses. After the initial infection of peripheral tissues by flaviviruses, they invade the CNS, where neurons are the main target (*50*). Because the CNS lacks secondary lymphoid tissues and cannot induce adaptive immune responses, it relies typically on intrinsic neuronal innate immunity to limit the extent of neuroviral infection. IFN-β, an early type I IFN, which is an inherent part of the neuronal innate immune response, is vital for the efficient restriction of neurotropic viral propagation (*51*).

miRNAs have emerged as important posttranscriptional regulators of many biological systems, including mammalian innate immunity (*52*, *53*), and they sometimes play a decisive role when the innate immune system is challenged by viral infection. Viruses may exploit cellular miRNAs, and in some cases, the increased abundance of cellular miRNAs may reshape cellular gene expression to the benefit of the virus. Here, we observed the substantial early enhancement of neuronal *miR-301a* expression after JEV infection, which led us to investigate whether miR-301a affected the antiviral IFN response. Inhibition of miR-301a in JEV-infected neuronal cells resulted in the considerable restoration of IFN-β production and the restriction of viral replication, suggesting that miR-301a abrogates the JEV-induced IFN response in neurons. Consistent with a previous report that showed that IFN-β elicits its antiviral actions by inducing the expression of a wide array of ISGs through its binding to IFN-stimulated response elements in the promoters of these genes (*54*), we found that the expression of *ISG15*, *IFIT1*, and *OAS1* was induced under conditions in which *miR-301a* expression was restricted. Under basal conditions, the expression of these ISGs is usually undetectable, but their expression is stimulated upon viral infection to mediate the antiviral effector functions of IFN-β (*55*).

To determine the biological role of the enhanced expression of *miR-301a* in the host response to JEV infection, we analyzed specific target genes and identified *IRF1* and *SOCS5* as miR-301a targets involved in the IFN-β response in neuronal cells. Delivery of miR-301a into neuronal cells resulted in decreased IRF1 and SOCS5 protein abundances but did not affect the amounts of *IRF1* and *SOCS5* mRNAs, which suggests that miR-301a reduced the amounts of these proteins by inhibiting mRNA translation without affecting mRNA abundance. Moreover, knockdown of miR-301a in JEV-infected neuronal cells substantially rescued the generation of IRF1 and SOCS5 proteins, demonstrating that JEV-induced miR-301a suppresses IRF1 and SOCS5.

Studies previously showed that IRF1 is a potent inhibitor of a broad spectrum of viruses, including flaviviruses (*56*, *57*). IRF1 shapes both innate and adaptive immune responses to protect the host from lethal WNV infection (*41*). Furthermore, *IRF1* expression in neurons prevents the replication of fatal neurotropic vesicular stomatitis virus (VSV) (*58*). The transcriptional profile of antiviral genes induced by type I IFNs is also stimulated by IRF1 (*56*). Thus, both IRF1 and IFN-β appear to promote an active and critical antiviral program. Although IRF1 is implicated as a regulator of the expression of genes encoding IFN-α and IFN-β, it specifically binds to the upstream regulatory region of the *IFN*-β gene and induces *IFN*-β expression in response to viral infection (*40*, *59*). Because miR-301a directly targets IRF1, we observed the substantial stimulation of the expression of *IFN*-β, but not *IFN*-α, when miR-301a was inhibited in JEV-infected neuronal cells. Knockdown of IRF1 in JEV-infected cells prevented the induction of *IFN*-β expression that occurred in miR-301a–inhibited cells, whereas ectopic expression of IRF1 conversely enhanced the expression of *IFN*-β in cells in which *miR-301a* was inhibited. Together, these observations suggest that miR-301a contributes to the suppression of IFN-β production through its effects on IRF1.

The other specific target of miR-301a that we found was SOCS5, which is not associated directly with the regulation of IFN-β production. SOCS5 is preferentially found in T helper 1 (T_H1) cells, and it inhibits the differentiation of naïve $CD4^+$ T cells into T_H2 cells, signifying a key role in regulating the balance between these two cell subsets (*60*). Members of the SOCS family can be manipulated for viral benefit, and the expression of SOCS-encoding genes is usually induced upon different viral infections (*61*–*63*). However, the role of SOCS5 in innate immunity was unknown until a report by Watanabe *et al.* (*39*) described how the overexpression

of SOCS5 enhances the innate immune response in murine septic peritonitis and improves survival. Consistent with this previous study, we found that knockdown or overexpression of SOCS5 in JEV-infected cells respectively attenuated or amplified *IFN*-β expression in neuronal cells in which miR-301a was inhibited.

The activation of EGFR during viral infection suppresses the IRF1-mediated antiviral response (*44*). Previous studies showed that SOCS5 interacts with the EGFR in a ligand-independent manner to inhibit EGFR signaling (*43*, *64*). Thus, we hypothesized that the miR-301a–mediated suppression of SOCS5 during JEV infection might initiate EGFR activation and thereby suppress *IRF1* expression. Accordingly, we observed that EGFR was activated in JEV-infected neuronal cells and that manipulation of endogenous or exogenous SOCS5 abundance potentially regulated the abundance of p-EGFR. Furthermore, the decreased expression of *IRF1* caused by knockdown of SOCS5 and the enhanced expression of *IRF1* in cells overexpressing SOCS5 suggest that SOCS5 stimulates *IRF1* expression in JEV-infected neuronal cells. The amplification of the IRF1-mediated IFN-β response in cells treated with the EGFR inhibitor AG 1478 further suggested the participation of EGFR in the SOCS5-dependent generation of IRF1 protein. The substantial reduction in JEV RNA abundance compared to the modest increase in *IRF1* expression in AG 1478–treated cells suggested that, in addition to enabling induction of *IRF1* expression, AG 1478 might directly inhibit JEV replication. Several reports showed that multiple viruses use EGFR for cell entry and that inhibitors of the kinase activity of EGFR inhibit viral infection (*65*–*67*). We assume that AG 1478, in conjunction with enabling induction of *IRF1* expression, might also hamper the entry of JEV into cells by inhibiting EGFR activation. The observation of the almost comparable viral titers in the culture medium of cells infected with JEV in the presence or absence of AG 1478 at late times during infection also supported our assumption. IRF1 and SOCS5 are involved in the miR-301a–mediated inhibition of JEV infection in neurons; however, they are not the only contributory factors. There are many other genes that are predicted to be potential targets of miR-301a (table S1) and thus may also be involved in the miR-301a–mediated regulation of host-virus interactions.

Numerous studies showed that virus-induced host transcription factors induce miRNA expression by binding to their promoter regions (*68*, *69*). We analyzed the *miR-301a* promoter with a software-based method and detected the binding sites of several transcription factors, including NF-κB. We focused on NF-κB because NF-κB activation stimulates the expression of *miR-301a* in a human pancreatic cancer cell line (*33*). However, other transcription factors may regulate *miR-301a* expression through binding to its promoter. Several miRNAs that are critical to innate and adaptive immunity regulate NF-κB signaling and influence the mammalian response to microbial infection (*70*, *71*). Here, we found that the promoter for mouse *miR-301a* contains an authentic RelA binding site and that *miR-301a* expression in neurons after JEV infection was dependent on NF-κB activation. The extent of NF-κB activation in JEV-infected neurons was directly proportional to the degree of *miR-301a* expression. Overexpressing NF-κB subunits in HT22 cells increased the transcription of *miR-301a*, as confirmed by mutagenesis studies in which the NF-κB binding site was disrupted. Furthermore, the NF-κB–driven transcription of *miR-301a* in JEV-infected cells was confirmed by luciferase reporter assays. Next, we treated the cells with PDTC. PDTC is an established antioxidant and NF-κB inhibitor, and it blocks NF-κB activation by inhibiting the ubiquitylation of IκB (inhibitor of nuclear factor κB) independently of its antioxidative functions (*72*). In neurons, PDTC prevents the nuclear translocation of NF-κB and its binding to DNA (*73*). Consistently, when we inhibited NF-κB translocation in JEV-infected HT22 cells with PDTC, we attenuated the expression of *miR-301a*. This resulted in the restored generation of the products of the target genes of miR-301a, thus suggesting that NF-κB promotes the expression of *miR-301a* during JEV infection. The binding of NF-κB to the *miR-301a* promoter element was further confirmed by ChIP analysis.

We validated the in vivo effect of miR-301a in a JEV-infected mouse model with miR-301a-VM. Several studies have already shown that Vivo-Morpholino actively decreases viral titers in animal models by blocking the translation of viral mRNA (*74*–*76*). Vivo-Morpholino has been used in vivo for the effective inhibition of specific miRNAs (*77*); therapeutics involving Vivo-Morpholino have also fruitfully reached human clinical trials (*78*, *79*). Previously, we showed that a Vivo-Morpholino against the JEV genome serves a neuroprotective role and blocks viral replication in mice to an extent similar to that by which a Vivo-Morpholino against TLR7 inhibits type I IFN production and promotes viral infection in neurons (*9*, *80*). Here, we injected miR-301a-VM into mice to demonstrate its potential application against JEV-induced immune evasion in a mouse model. Therapeutic treatment during the early stage of JEV infection efficiently relieved clinical signs, including paralysis and loss of body weight, as well as improved survival. For further clarification, we checked the interactions of miR-301a with its targets and the subsequent effects on IFN-β production and JEV propagation in vivo. Inhibition of miR-301a restored the abundances of IRF1 and SOCS5 proteins and further promoted the expression of *IFN*-β and ISGs, effectively resulting in a substantial reduction in JEV replication. Thus, Vivo-Morpholino–based antisense therapy targeting miR-301a could be a promising therapeutic approach against JEV infections. JEV pathogenicity is fundamentally similar to that of other encephalitic flaviviruses, where it is believed that initial virus replication occurs in peripheral organs including the liver, kidney, heart, and lung, and then invades the CNS to develop neuropathogenesis (*81*). Because miR-301a is an abundant miRNA in the brain and there is no evidence of its signaling in liver and kidney, it did not affect IFN production in peripheral organs after infection with JEV.

Most miRNAs, together with cellular mRNAs, are transcribed by polymerase II using many of the same transcription factors (*19*). Thus, cellular transcription factors, whose abundances are increased by viral infection, play a vital role in changing miRNA expression patterns. Viral infection activates NF-κB, which is crucial for initiating the production of antiviral IFNs; however, sometimes this immune response, if it is too strong and persists for too long, can be harmful to the host. Thus, cells must have negative feedback mechanisms to tightly regulate the response (*82*). There are several reports indicating that miRNA is part of a negative feedback mechanism, which inhibits inflammatory cytokine production in response to microbial stimuli (*83*, *84*). A study that used bacterial lipopolysaccharide revealed that the NF-κB–dependent induction of *miR-146a* and *miR-146b* expression inhibits the innate immune response by targeting IL-1 receptor–associated kinase 1 (IRAK1) and tumor necrosis factor receptor–associated factor 6 (TRAF6) (*70*). This regulatory mechanism is exploited by many viruses, including Epstein-Barr virus (EBV), Kaposi's sarcoma–associated herpesvirus (KSHV), Enterovirus 71 (EV71), Sendai virus (SeV), VSV, and hepatitis C virus (HCV), to evade the host innate immune system. EBV stimulates the NF-κB–dependent expression of cellular *miR-155*, which in turn targets intermediates of innate immune signaling pathways (*71*). The miRNA miR-132 inhibits innate antiviral immunity during KSHV infection by inhibiting expression of the transcriptional coactivator p300 (*85*). EV71 induces the expression of *miR-146a*, which targets IRAK1 and TRAF6, which are involved in TLR signaling and type I IFN production (*86*). The expression of *IFNA1* is repressed by miR-466I in cells infected with SeV and VSV (*87*). The increased expression of *miR-21* promotes

HCV replication by inhibiting IFN-α signaling through the targeting of MyD88 and IRAK1 (*88*). HCV also induces the expression of a liver-specific miRNA, miR-122, to enhance viral genome stabilization and protein translation (*89*). Here, we found that JEV infection increases the abundance of the host miR-301a to inhibit IFN-β production and escape the host immune response.

In summary, we have identified a previously uncharacterized, neuron-specific host-virus interaction, in which the NF-κB–mediated inducible expression of *miR-301a* inhibits the antiviral IFN-β response by suppressing IRF1 and SOCS5 production. Thus, the virus evades the host innate immune system. Deactivation of JEV-induced *miR-301a* expression conversely impaired this molecular pathway, thereby restoring the antiviral immune response and reducing mortality in JEV-infected mice (fig. S10). Thus, miR-301a might be a potential therapeutic target in JEV infection of humans. These findings further illuminate the influence of host miRNA on the antiviral response and may help to understand the molecular pathogenesis driven by flavivirus-host interactions.

MATERIALS AND METHODS

Mice

P10 BALB/c mice of either sex were housed together with their respective mothers under a 12-hour dark/12-hour light cycle at a constant temperature and humidity. All experiments were performed after obtaining approval from the Institutional Animal Ethics Committee of the National Brain Research Centre (NBRC) (approval no. NBRC/IAEC/2014/96). The animals were handled in strict accordance with good animal practice as per the guidelines of the Committee for the Purpose of Control and Supervision of Experiments on Animals, Ministry of Environment and Forestry, Government of India.

Cell culture

The mouse hippocampal neuronal cell line HT22, a gift from S. K. Sharma (NBRC); the mouse microglial cell line BV2 and the human neuroblastoma cell line SH-SY5Y, a gift from S. Levison (Rutgers University–New Jersey Medical School, NJ); the human hepatocellular liver carcinoma cell line HepG2, a gift from E. Sen (NBRC); the HEK 293 cell line, provided by A. Krishnan (Institute of Molecular Medicine, New Delhi, India); and porcine stable kidney cells (PS cells), a gift from G. R. Medigeshi (Translational Health Science and Technology Institute, Faridabad, India), were cultured at 37°C in Dulbecco's modified Eagle's medium (DMEM) supplemented with 10% fetal bovine serum (FBS), penicillin (100 units/ml), and streptomycin (100 μg/ml). All cell culture reagents were obtained from Sigma-Aldrich, unless otherwise specified. HT22 cells were used for our experiments with previous permission from D. Schubert of the Salk Institute from whom these cells were originally obtained.

Primary cortical neuronal cultures

Cortical neurons were cultured according to a previously described protocol (*9*). Briefly, cortices of P2 BALB/c mouse pups were dissected aseptically in calcium- and magnesium-free (CMF) Tyrode's solution after decapitation. After the meninges were removed, the tissue was chopped into smaller pieces and collected in the CMF-Tyrode's solution. The samples were treated with trypsin-deoxyribonuclease and then dissociated in the same solution by trituration to make a single-cell suspension. The suspension was centrifuged, and the pellet was resuspended in neurobasal medium, supplemented with 2 mM L-glutamine, 1% glucose, 5% FBS, 10% horse serum, and penicillin-streptomycin. Cells were plated at a density of $5 \times 10^3/cm^2$ onto poly-D-lysine–coated Lab-Tek chamber slides for immunofluorescence staining, whereas for RNA preparation, 3×10^5 cells were seeded in 60-mm plates. After 48 hours of incubation at 37°C, the serum-containing medium was replaced with serum-free medium, and the cells were incubated for 4 hours with antibiotics alone. For experimental treatments, the resting medium was exchanged for DMEM with N2 and B27 supplements and antibiotics. Arabinoside (20 μM) was used to inhibit astrocyte proliferation.

Viral infection of cells and mice

All cells were seeded at the desired density in culture plates as per the requirements for different experiments. After the cells reached 90% confluence, they were further incubated for 3 to 4 hours in serum-free medium and infected with JEV (strain GP78) at an MOI of 5. Cells were harvested at different times for the time course study. For the dose-dependent study, the cells were infected for 6 hours separately with JEV at MOIs of 1, 5, or 10. The infection of primary neuronal cells was performed according to a similar procedure. Mock infection (MI) consisted of adding the same amount of medium as that containing the JEV inoculum but without virus. P10 BALB/c mouse pups were divided into two groups, each having four pups; the gender of the mice in each group was random unless otherwise indicated. Members of the JEV group of mice were injected with 3×10^5 plaque-forming units (PFU) of virus, whereas members of the uninfected group received phosphate-buffered saline (PBS) through the intraperitoneal route. After 2 days of infection, the animals were sacrificed, and the brains were excised after repeated transcardial perfusion with ice-cold PBS. For ISH and immunofluorescence analysis, tissues were fixed with 4% paraformaldehyde (PFA) for 48 hours at 4°C and then dipped in 30% sucrose until they were completely immersed in the solution. The tissues were then processed for cryosectioning. For miRNA, RNA, and protein isolation, the brains were stored at −80°C until needed for use.

Combined ISH and IHC analysis

Cryosections, prepared with a Leica CM3050S cryostat, were processed for ISH with the miRCURY LNA microRNA ISH Optimization Kit (Exiqon), as described previously (*29*). Briefly, thawed sections were fixed in fresh 30% formalin overnight. After washes with PBS, the sections were treated with proteinase K (7 μg/ml) at 37°C for 15 min. The sections were then thoroughly washed with PBS, dehydrated with ethanol, and incubated with hybridization buffer containing 60 nM double digoxigenin (DIG)–labeled LNA miR-301a probe (5′-GCTTTGACAATACTATTGCACTG-3′; Exiqon) or 5 nM 5′-DIG–labeled LNA U6 snRNA probe (5′-CACGAATTTGCGTGTCATCCTT-3′; Exiqon) for 1 hour at 55°C in a humidified chamber. After hybridization, the sections were sequentially washed with 5×, 1×, and 0.2× saline-sodium citrate buffer and incubated with blocking solution for 15 min at room temperature. Sections were then incubated with sheep anti–DIG–alkaline phosphatase (AP) antibody (1:400 dilution; Roche Life Science) for 60 min at room temperature in a humidified chamber and then were washed twice with 1× PBS-Tween 20 (PBST). Freshly prepared AP substrate (Roche Life Science) was then added to the sections and incubated for 2 hours at 30°C in the humidifying chamber under dark conditions. The reaction was terminated by the addition of KTBT buffer (an AP stop solution composed of 50 mM tris-HCl, 150 mM NaCl, and 10 mM KCl) for 5 min. After stringent washing with water, sections were incubated in blocking solution (5% bovine serum albumin in PBS) for 20 min followed by overnight incubation with anti-MAP2 antibody (1:200, Millipore) at 4°C. After extensive washing with PBS, the sample slides were incubated with biotinylated anti-mouse immunoglobulin G (IgG; 1:200, Vector

Laboratories) for 30 min at room temperature followed by a 20-min incubation with horseradish peroxidase (HRP)–conjugated streptavidin (1:250, Vector Laboratories). After the samples were rinsed with PBS, a brown reaction product was developed with a DAB substrate kit (SK-4100, Vector Laboratories) according to the manufacturer's instructions. After a 2-min reaction, the slides were dehydrated in a series of solutions containing different percentages of alcohol and mounted with DPX (Qualigens). The slides were observed with a Leica DMRXA2 microscope, and images were taken under the appropriate magnification for each sample.

Transfection of cells with miRNA mimics and inhibitors

To overexpress or inhibit miR-301a, we transfected cells with mimics of mouse or human miR-301a (double-stranded RNAs that mimic mature endogenous miR-301a) or with miR-301a inhibitors (single-stranded, modified RNAs that specifically inhibit endogenous miR-301a) (Qiagen), respectively, with the HiPerFect Transfection Reagent (Qiagen) according to the manufacturer's instructions. Twenty-four hours later, the cells were harvested or infected with JEV for specific times and then were analyzed to determine the abundances of the miRNAs, mRNAs, and proteins of interest. Negative controls of the mimic or inhibitor (Ambion) were used in the transfections as the matched controls. MT cells received an equal volume of HiPerFect reagent that did not contain any nucleic acid.

Enzyme-linked immunosorbent assay

HT22 cells were seeded in six-well plates (0.3×10^6), incubated overnight, and transfected with the miR-301a inhibitor or inhibitor control. Twenty-four hours later, the cells were infected with JEV for the appropriate times. In another set of experiments, the cells were infected with JEV for 6 hours in the presence of Tyrphostin AG 1478, as indicated in the figure legends. In both sets of experiments, the concentration of IFN-β in the cell culture medium was determined by ELISA using the antibody pair for the detection IFN-β and the IFN-β standard (BioLegend) according to the manufacturer's recommendations.

Plasmid construction

The 354–base pair (bp) segment of cDNA encoding the 3′UTR of mouse *SOCS5* and a 429-bp cDNA segment encoding the 3′UTR of *IRF1* containing the putative miR-301a binding site were amplified by PCR from mouse brain cDNA with the SOCS5 Luc and IRF1 Luc primers (forward and reverse), respectively (table S3). The DNA fragments were subcloned into the Hind III and Spe I sites downstream of the firefly luciferase gene in the pMIR-REPORT plasmid. Site-directed mutagenesis performed with the SOCS5 Luc Mut and IRF1 Luc Mut primers (forward and reverse; table S3) generated mutants with the appropriate mutations. A PCR-based method involving Phusion High-Fidelity DNA Polymerase and Dpn I (New England Biolabs) was performed for mutagenesis. The SOCS cds and IRF1 cds primers (forward and reverse; table S3) were respectively used to amplify the coding regions for *SOCS5* and *IRF1* from mouse cDNA. These PCR products were digested with Hind III and Xho I or Hind III and Bam HI, respectively, and then cloned into the pcDNA 3.1(+) plasmid (which was provided by D. Chattopadhyay, Amity University, Kolkata, India). The ~1.8-kb promoter element of *miR-301a* was amplified from mouse cDNA with the miR-301a Pro forward and reverse primers (table S3), digested with Mlu I and Xho I, and inserted into the pGL3-Basic vector (a gift from P. Chattopadhyay, All India Institute of Medical Sciences, New Delhi, India) immediately upstream of the firefly luciferase gene. The mutation in the RelA binding site in the promoter segment was achieved with the miR-301a Pro Mut forward and reverse primer (table S3) according to the site-directed mutagenesis procedure described earlier. Hence, all of the constructs were commercially sequenced at Invitrogen BioServices India Pvt. Ltd., Gurgaon, India.

Transfection of cells with esiRNA and plasmids

esiRNA specific for mouse SOCS5 (EMU021991) and IRF1 (EMU052481), as well as negative Con-esiRNA (sense, 5′-GTGAGCAAGGGCGAGGAGCTGTTCACCGGGGTGGTGCCCATCCTGGTCGAG CTG GA-3′) were purchased from Sigma-Aldrich. HT22 cells were transfected with either esiRNAs (10 pM) or plasmids encoding SOCS5 or IRF1 with Lipofectamine 2000 (Invitrogen) according to the manufacturer's protocol. Briefly, after the cells reached 70 to 80% confluence, they were cotransfected with the miR-301a inhibitor and either the esiRNAs or expression plasmids with commercial medium (Opti-MEM, Invitrogen) and Lipofectamine 2000. Twenty-four hours later, the cells were infected with JEV (MOI, 5) for 6 hours, and the cells were then subjected to mRNA analysis. Transfection efficiency was assessed by measuring the amounts of the proteins of interest. MT cells received an equivalent volume of Opti-MEM and Lipofectamine mix in the absence of any nucleic acid.

Luciferase reporter assays

HT22 cells (2×10^4) were seeded in a 24-well plate for 16 to 18 hours and then were transiently transfected with firefly luciferase reporter constructs together with either an miR-301a mimic or inhibitor and their respective controls with Lipofectamine 2000. The cells were also cotransfected with a *Renilla* luciferase vector (pRL-TK, a gift from E. Sen, NBRC) for normalization of transfection efficiency. Twenty-four hours later, the cells were harvested at the times indicated in the figure legends and were lysed in Passive Lysis Buffer (Promega). The luciferase activity of each sample was measured with the Dual-Luciferase Reporter Assay System (Promega) with a GloMax 96 Microplate Luminometer according to the manufacturer's protocol. For promoter analysis, HT22 cells were cotransfected with the luciferase reporter constructs, and the mouse RelA cFlag pcDNA3 clone (Addgene plasmid repository) with Lipofectamine 2000. The pGL3-Basic vector was used as a negative control. Luciferase activity was determined 24 hours later. In another set of experiments, the cells were transiently transfected with the promoter constructs. Twenty-four hours later, the cells were infected with JEV, and luminescence was measured at the times indicated in the figure legends.

ChIP assays

ChIP assays were performed with the Dynabeads Protein G Immunoprecipitation Kit (Life Technologies) according to the manufacturer's instructions. Briefly, uninfected or JEV-infected HT22 cells were first treated with 1% formaldehyde for 10 min, which was stopped by the addition of 0.25 M glycine (pH 7.0). After centrifugation, the cell pellet was lysed in radioimmunoprecipitation assay buffer containing protease inhibitors and then was sonicated to shear the chromatin. The lysate was then mixed with Dynabeads Protein G (Invitrogen) (50/250 μl of lysate) in a HulaMixer (Invitrogen) for 1 hour at 4°C. The precleared supernatant, referred to as input sample, was subjected to immunoprecipitation with 10 μl of anti-RelA (p-p65) antibody conjugated to Dynabeads (50 μl). The precipitated complexes were then eluted and subjected to reverse cross-linking by the addition of 0.2 M NaCl, which was followed by incubation at 65°C for 6 hours. The coimmunoprecipitated DNA was purified with a QIAquick PCR purification kit (Qiagen). Occupancy of the promoter was

detected by PCR and qRT-PCR with primers flanking the p50-RelA binding site in the mouse *miR-301a* promoter (forward primer, 5′-AGTC-GTGAAGCATTGCTATC-3′; reverse primer, 5′-AAGACTAAGGAC-CTGTGGTC-3′). Input sample (40 μl) was subjected to reverse cross-linking and resolved by SDS–polyacrylamide gel electrophoresis (SDS-PAGE). After ChIP was performed, the Dynabeads were boiled with loading buffer for 10 min and analyzed by Western blotting to assess the immunoprecipitation efficiency.

Quantitative RT-PCR

For quantitative determination of mature mRNA and miRNA abundances, qRT-PCR analysis was performed. After the isolation of total RNA from treated cells with Tri Reagent (Sigma-Aldrich), cDNA was prepared with the Advantage RT-for-PCR Kit (Clontech Laboratories). qRT-PCR analysis of mouse and human IFNs, ISGs, and viral RNA were performed with the Power SYBR Green PCR Master Mix (Applied Biosystems) with gene-specific primers (table S1). The relative abundance of an mRNA of interest was determined by normalization to that of *GAPDH* mRNA through the $2^{-\Delta\Delta C_t}$ method (C_t refers to the threshold value). miRNA was isolated with a miRNeasy kit (Qiagen), and cDNA was prepared with a miScript II RT Kit with miScript HiSpec buffer (Qiagen) according to the manufacturer's instructions. The forward primers for amplification of different miRNAs were as follows: mouse miR-301a, 5′-CAGUGCAAUAGUAUUGUCAAAGC-3′; human miR-301a, 5′-CAGUGCAAUAGUAUUGUCAAAGC-3′; and mouse miR-301b, 5′-CAGUGCAAUGGUAUUGUCAAAGC-3′. qRT-PCR was performed with specific forward primers and the miScript SYBR Green PCR Kit containing the miScript Universal Reverse Primer (Qiagen). The snRNA *SNORD68* was used as a normalization control. The thermal cycler ViiA 7 Real-Time PCR (Applied Biosystems) was used for qRT-PCR, and the data were analyzed with the iCycler Thermal Cycler software (Applied Biosystems).

Western blotting

Cells and mouse tissues were lysed in complete lysis buffer containing 1% Triton X-100, 10 mM tris-HCl (pH 8.0), 150 mM NaCl, 0.5% NP-40, 1 mM EDTA, 0.2% EGTA, 0.2% sodium orthovanadate, and a protease inhibitor cocktail (Sigma-Aldrich); and the protein concentration in each sample was measured with the BCA reagent (Sigma-Aldrich). Equal amounts of the proteins were resolved by SDS-PAGE and transferred onto a nitrocellulose membrane, which was blocked with 5% skim milk in 1× PBST and incubated with primary antibodies specific for SOCS5 (1:1000, Abcam), IRF1 (1:1000, Cell Signaling Technology), NF-κB (1:1000, Santa Cruz Biotechnology), pNF-κB (1:1000, Cell Signaling Technology), pIκBα (1:1000, Cell Signaling Technology), IκBα (1:1000, Cell Signaling Technology), pIKKα/β (1:1000, Cell Signaling Technology), p-EGFR (1:1000, Abcam), the Flag tag (1:1000, Sigma-Aldrich), proliferating cell nuclear antigen (PCNA) (1:2000, Cell Signaling Technology), or β-actin (1:10,000; Sigma-Aldrich). β-actin was used as internal control except for samples containing nuclear proteins for which PCNA acted as the internal control. The secondary antibodies used for detection were HRP-conjugated goat anti-mouse and goat anti-rabbit IgG (1:5000, Vector Laboratories). The blots were developed by exposure in a ChemiGenius Bio-Imaging System (Syngene) with GeneSnap software. Representative Western blots are shown in the figures. Samples of the Western blots used to generate the densitometric data shown in Figs. 3 to 8 can be found in fig. S11, whereas those used to generate the densitometric data shown in figs. S3, S4, S6, and S8 can be found in fig. S12.

Immunofluorescence

Brain sections were permeabilized with 0.1% Triton X-100 in PBS and then incubated with a blocking buffer for 1 hour at room temperature, which was followed by overnight incubation with anti-NeuN (1:250, Millipore) and anti-SOCS5 (1:250, Abcam) antibodies at 4°C. After extensive washing, the sections were incubated with Alexa Fluor 488– or Alexa Fluor 594–conjugated secondary antibodies (1:1500, Molecular Probes) for 1 hour. Finally, the sections were mounted with 4′,6-diamidino-2-phenylindole (Vector Laboratories Inc.) and observed with a Zeiss Apotome microscope at the specified magnification. Primary cortical neuronal cells were infected with JEV for 6 hours, fixed with 4% PFA, and then subjected to the same immunofluorescence analysis.

Inhibition of EGFR activation

HT22 cells were seeded into six-well plates and infected with JEV in the presence or absence of the selective EGFR tyrosine kinase inhibitor, Tyrphostin AG 1478 (10 μM) (Sigma-Aldrich). Six hours after infection, the cells were harvested to assess *IRF1* mRNA and viral RNA abundances by qRT-PCR analysis. In addition, cell culture medium was collected to measure IFN-β secretion and JEV titers at the times indicated in the figure legends.

Inhibition of NF-κB activation

HT22 cells were treated with 50 μM PDTC (an inhibitor of NF-κB activation) (Sigma-Aldrich) for 2 hours before being infected with JEV for 6 hours. The abundances of cytosolic and nuclear proteins of interest were analyzed by Western blotting, whereas the amounts of miRNAs were analyzed by qRT-PCR analysis.

JEV infection and administration of Vivo-Morpholino to mice

The GP78 strain of JEV was propagated in suckling BALB/c mice (P3 or P4) of either sex until the symptoms of sickness (limb paralysis, poor pain response, and whole-body tremors) appeared. At this point, viral suspensions were prepared as described previously (*29*). The virus was titrated by plaque formation assay with the PS cell line as reported previously (*29*). For in vivo experiments, P10 mice of either sex were randomly assigned to eight groups. Among them, group 1 was the MI group and received only PBS, whereas mice from the other seven groups were injected intraperitoneally with JEV (3×10^5 PFU). In addition to receiving virus, mice in groups 3, 4, and 5 were treated with the Vivo-Morpholino (Gene Tools LLC) negative control (VM-NC; 18 mg/kg) intracranially at the times indicated in the figure legends, whereas those in groups 6, 7, and 8 received miR-301a Vivo-Morpholino (miR-301a-VM; 18 mg/kg). After 72 hours, the mice were euthanized, and brain samples were collected for qRT-PCR, plaque assay, and Western blotting analyses. For peripheral infections, WT mice were injected intraperitoneally with miR-301a-VM (12 mg/kg) or VM-NC (12 mg/kg), according to the manufacturer's instructions, after 12, 24, and 48 hours of virus infection (3×10^5 PFU) as indicated. Three days later, liver and kidney tissues were collected to evaluate miRNA and mRNA expression.

Plaque assays

Viral titers in cell culture medium and brain samples were assessed by plaque assay. Plaque formation was performed on monolayers of PS cells. Cells were seeded in six-well plates at a density to give semiconfluent monolayers in about 18 hours. Monolayers were inoculated with serial dilutions of culture medium or virus sample (obtained from brain) in MEM containing 1% fetal calf serum and incubated for 1 hour at 37°C

with occasional shaking. The inoculum was removed by aspiration, and the monolayers were overlaid with MEM containing 5% FBS, 1% low–melting point agarose, and a cocktail of penicillin-streptomycin (0.5%). Plates were incubated at 37°C for 3 to 4 days until plaques were visible. To enable counting of the plaques, we stained the cell monolayer with crystal violet after the cells were fixed with 10% PFA (*80*).

Statistical analysis

All experiments were performed in triplicate unless otherwise indicated. To analyze statistical difference between the two groups, we used a Student's two-tailed unpaired *t* test. Comparisons involving multiple groups were assessed by one-way ANOVA followed by Bonferroni's post hoc test, whereas differences between multiple groups influenced by two factors were evaluated by two-way ANOVA followed by the Holm-Sidak method. $P < 0.05$ was considered statistically significant. The results are expressed as means ± SD, and graphs were prepared with KyPlot (version 2.0 beta 13) and SigmaPlot 11.0.

SUPPLEMENTARY MATERIALS

www.sciencesignaling.org/cgi/content/full/10/466/eaaf5185/DC1

Fig. S1. Expression profile of miR-301 family members during JEV infection.
Fig. S2. miR-301a inhibits the antiviral type I IFN response and increases viral replication.
Fig. S3. *SOCS5* and *IRF1* are targets of miR-301a.
Fig. S4. Suppression of SOCS5 and IRF1 protein production is reversed by inhibition of miR-301a.
Fig. S5. Loss of SOCS5 protein early during JEV infection.
Fig. S6. JEV induces *miR-301a* expression through the activation of NF-κB.
Fig. S7. In vivo dose standardization and treatment with miR-301a-VM in JEV-infected mice.
Fig. S8. Aberrant regulation of *miR-301a* expression during JEV infection in mouse liver and kidney.
Fig. S9. The regulation of *miR-301a* expression is not ubiquitous in the peripheral organs of JEV-infected mice.
Fig. S10. The role of miR-301a early in JEV infection.
Fig. S11. Examples of Western blots used for densitometric analysis.
Fig. S12. Further examples of Western blots used for densitometric analysis.
Table S1. Potential targets of mouse miR-301a.
Table S2. Prediction of transcription factor binding sites within the *miR-301a* promoter by PROMO software.
Table S3. Primer sequences.

REFERENCES AND NOTES

1. S. Tiwari, R. K. Singh, R. Tiwari, T. N. Dhole, Japanese encephalitis: A review of the Indian perspective. *Braz. J. Infect. Dis.* **16**, 564–573 (2012).
2. T. Solomon, N. M. Dung, R. Kneen, M. Gainsborough, D. W. Vaughn, V. T. Khanh, Japanese encephalitis. *J. Neurol. Neurosurg. Psychiatry* **68**, 405–415 (2000).
3. D. Ghosh, A. Basu, Japanese encephalitis—A pathological and clinical perspective. *PLOS Negl. Trop. Dis.* **3**, e437 (2009).
4. T. Solomon, Control of Japanese encephalitis—Within our grasp? *N. Engl. J. Med.* **355**, 869–871 (2006).
5. M. Fischer, N. Lindsey, J. E. Staples, S. Hills, Japanese encephalitis vaccines: Recommendations of the Advisory Committee on Immunization Practices (ACIP). *MMWR Recomm. Rep.* **59**, 1–27 (2010).
6. N. Yan, Z. J. Chen, Intrinsic antiviral immunity. *Nat. Immunol.* **13**, 214–222 (2012).
7. A. N. Theofilopoulos, R. Baccala, B. Beutler, D. H. Kono, Type I interferons (α/β) in immunity and autoimmunity. *Annu. Rev. Immunol.* **23**, 307–336 (2005).
8. A. Nazmi, K. Dutta, B. Hazra, A. Basu, Role of pattern recognition receptors in flavivirus infections. *Virus Res.* **185**, 32–40 (2014).
9. A. Nazmi, S. Mukherjee, K. Kundu, K. Dutta, A. Mahadevan, S. K. Shankar, A. Basu, TLR7 is a key regulator of innate immunity against Japanese encephalitis virus infection. *Neurobiol. Dis.* **69**, 235–247 (2014).
10. A. Nazmi, K. Dutta, A. Basu, RIG-I mediates innate immune response in mouse neurons following Japanese encephalitis virus infection. *PLOS ONE* **6**, e21761 (2011).
11. A. Nazmi, R. Mukhopadhyay, K. Dutta, A. Basu, STING mediates neuronal innate immune response following Japanese encephalitis virus infection. *Sci. Rep.* **2**, 347 (2012).
12. R.-J. Lin, C.-L. Liao, E. Lin, Y.-L. Lin, Blocking of the alpha interferon-induced Jak-Stat signaling pathway by Japanese encephalitis virus infection. *J. Virol.* **78**, 9285–9294 (2004).
13. R.-J. Lin, B.-L. Chang, H.-P. Yu, C.-L. Liao, Y.-L. Lin, Blocking of interferon-induced Jak-Stat signaling by Japanese encephalitis virus NS5 through a protein tyrosine phosphatase-mediated mechanism. *J. Virol.* **80**, 5908–5918 (2006).
14. D. S. Burke, W. Lorsomrudee, C. J. Leake, C. H. Hoke, A. Nisalak, V. Chongswasdi, T. Laorakpongse, Fatal outcome in Japanese encephalitis. *Am. J. Trop. Med. Hyg.* **34**, 1203–1210 (1985).
15. C. Harinasuta, S. Nimmanitya, U. Titsyakorn, The effect of interferon-alpha A on two cases of Japanese encephalitis in Thailand. *Southeast Asian J. Trop. Med. Public Health* **16**, 332–336 (1985).
16. C. Ajariyakhajorn, M. P. Mammen Jr., T. P. Endy, M. Gettayacamin, A. Nisalak, S. Nimmannitya, D. H. Libraty, Randomized, placebo-controlled trial of nonpegylated and pegylated forms of recombinant human alpha interferon 2a for suppression of dengue virus viremia in rhesus monkeys. *Antimicrob. Agents Chemother.* **49**, 4508–4514 (2005).
17. M. A. Samuel, M. S. Diamond, Alpha/beta interferon protects against lethal West Nile virus infection by restricting cellular tropism and enhancing neuronal survival. *J. Virol.* **79**, 13350–13361 (2005).
18. V. Ambros, The functions of animal microRNAs. *Nature* **431**, 350–355 (2004).
19. B. R. Cullen, Viruses and microRNAs: RISCy interactions with serious consequences. *Genes Dev.* **25**, 1881–1894 (2011).
20. J. L. Smith, F. E. Grey, J. L. Uhrlaub, J. Nikolich-Zugich, A. J. Hirsch, Induction of the cellular microRNA, Hs_154, by West Nile virus contributes to virus-mediated apoptosis through repression of antiapoptotic factors. *J. Virol.* **86**, 5278–5287 (2012).
21. A. Slonchak, R. P. Shannon, G. Pali, A. A. Khromykh, Human microRNA miR-532-5p exhibits antiviral activity against West Nile virus via suppression of host genes SESTD1 and TAB3 required for virus replication. *J. Virol.* **90**, 2388–2402 (2015).
22. M. Escalera-Cueto, I. Medina-Martínez, R. M. del Angel, J. Berumen-Campos, A. L. Gutiérrez-Escolano, M. Yocupicio-Monroy, Let-7c overexpression inhibits dengue virus replication in human hepatoma Huh-7 cells. *Virus Res.* **196**, 105–112 (2015).
23. X. Zhu, Z. He, Y. Hu, W. Wen, C. Lin, J. Yu, J. Pan, R. Li, H. Deng, S. Liao, J. Yuan, J. Wu, J. Li, M. Li, MicroRNA-30e* suppresses dengue virus replication by promoting NF-κB-dependent IFN production. *PLOS Negl. Trop. Dis.* **8**, e3088 (2014).
24. N. Wu, N. Gao, D. Fan, J. Wei, J. Zhang, J. An, miR-223 inhibits dengue virus replication by negatively regulating the microtubule-destabilizing protein STMN1 in EAhy926 cells. *Microbes Infect.* **16**, 911–922 (2014).
25. Z. Chen, J. Ye, U. Ashraf, Y. Li, S. Wei, S. Wan, A. Zohaib, Y. Song, H. Chen, S. Cao, MicroRNA-33a-5p modulates Japanese encephalitis virus replication by targeting eukaryotic translation elongation factor 1A1. *J. Virol.* **90**, 3722–3734 (2016).
26. S. Pareek, S. Roy, B. Kumari, P. Jain, A. Banerjee, S. Vrati, MiR-155 induction in microglial cells suppresses Japanese encephalitis virus replication and negatively modulates innate immune responses. *J. Neuroinflammation* **11**, 97 (2014).
27. B. Zhu, J. Ye, Y. Nie, U. Ashraf, A. Zohaib, X. Duan, Z. F. Fu, Y. Song, H. Chen, S. Cao, MicroRNA-15b modulates Japanese encephalitis virus-mediated inflammation via targeting RNF125. *J. Immunol.* **195**, 2251–2262 (2015).
28. M. C. Thounaojam, D. K. Kaushik, K. Kundu, A. Basu, MicroRNA-29b modulates Japanese encephalitis virus-induced microglia activation by targeting tumor necrosis factor alpha-induced protein 3. *J. Neurochem.* **129**, 143–154 (2014).
29. M. C. Thounaojam, K. Kundu, D. K. Kaushik, S. Swaroop, A. Mahadevan, S. K. Shankar, A. Basu, MicroRNA 155 regulates Japanese encephalitis virus-induced inflammatory response by targeting Src homology 2-containing inositol phosphatase 1. *J. Virol.* **88**, 4798–4810 (2014).
30. X. Ma, F. Yan, Q. Deng, F. Li, Z. Lu, M. Liu, L. Wang, D. J. Conklin, J. McCracken, S. Srivastava, A. Bhatnagar, Y. Li, Modulation of tumorigenesis by the pro-inflammatory microRNA miR-301a in mouse models of lung cancer and colorectal cancer. *Cell Discov.* **1**, 15005 (2015).
31. C. He, Y. Shi, R. Wu, M. Sun, L. Fang, W. Wu, C. Liu, M. Tang, Z. Li, P. Wang, Y. Cong, Z. Liu, miR-301a promotes intestinal mucosal inflammation through induction of IL-17A and TNF-α in IBD. *Gut* **65**, 1938–1950 (2016).
32. L. Huang, Y. Liu, L. Wang, R. Chen, W. Ge, Z. Lin, Y. Zhang, S. Liu, Y. Shan, Q. Lin, M. Jiang, Down-regulation of miR-301a suppresses pro-inflammatory cytokines in Toll-like receptor-triggered macrophages. *Immunology* **140**, 314–322 (2013).
33. Z. Lu, Y. Li, A. Takwi, B. Li, J. Zhang, D. J. Conklin, K. H. Young, R. Martin, Y. Li, miR-301a as an NF-κB activator in pancreatic cancer cells. *EMBO J.* **30**, 57–67 (2011).
34. M. P. Mycko, M. Cichalewska, A. Machlanska, H. Cwiklinska, M. Mariasiewicz, K. W. Selmaj, MicroRNA-301a regulation of a T-helper 17 immune response controls autoimmune demyelination. *Proc. Natl. Acad. Sci. U.S.A.* **109**, E1248–E1257 (2012).
35. B. John, A. J. Enright, A. Aravin, T. Tuschl, C. Sander, D. S. Marks, Human microRNA targets. *PLOS Biol.* **2**, e363 (2004).
36. B. P. Lewis, C. B. Burge, D. P. Bartel, Conserved seed pairing, often flanked by adenosines, indicates that thousands of human genes are microRNA targets. *Cell* **120**, 15–20 (2005).

37. A. Krek, D. Grün, M. N. Poy, R. Wolf, L. Rosenberg, E. J. Epstein, P. MacMenamin, I. da Piedade, K. C. Gunsalus, M. Stoffel, N. Rajewsky, Combinatorial microRNA target predictions. *Nat. Genet.* **37**, 495–500 (2005).
38. N. Wong, X. Wang, miRDB: An online resource for microRNA target prediction and functional annotations. *Nucleic Acids Res.* **43**, D146–D152 (2014).
39. H. Watanabe, M. Kubo, K. Numata, K. Takagi, H. Mizuta, S. Okada, T. Ito, A. Matsukawa, Overexpression of suppressor of cytokine signaling-5 in T cells augments innate immunity during septic peritonitis. *J. Immunol.* **177**, 8650–8657 (2006).
40. M. Miyamoto, T. Fujita, Y. Kimura, M. Maruyama, H. Harada, Y. Sudo, T. Miyata, T. Taniguchi, Regulated expression of a gene encoding a nuclear factor, IRF-1, that specifically binds to IFN-β gene regulatory elements. *Cell* **54**, 903–913 (1988).
41. J. D. Brien, S. Daffis, H. M. Lazear, H. Cho, M. S. Suthar, M. Gale Jr., M. S. Diamond, Interferon regulatory factor-1 (IRF-1) shapes both innate and $CD8^+$ T cell immune responses against West Nile virus infection. *PLOS Pathog.* **7**, e1002230 (2011).
42. A. Yoshimura, T. Naka, M. Kubo, SOCS proteins, cytokine signalling and immune regulation. *Nat. Rev. Immunol.* **7**, 454–465 (2007).
43. S. E. Nicholson, D. Metcalf, N. S. Sprigg, R. Columbus, F. Walker, A. Silva, D. Cary, T. A. Willson, J.-G. Zhang, D. J. Hilton, W. S. Alexander, N. A. Nicola, Suppressor of cytokine signaling (SOCS)-5 is a potential negative regulator of epidermal growth factor signaling. *Proc. Natl. Acad. Sci. U.S.A.* **102**, 2328–2333 (2005).
44. I. F. Ueki, G. Min-Oo, A. Kalinowski, E. Ballon-Landa, L. L. Lanier, J. A. Nadel, J. L. Koff, Respiratory virus–induced EGFR activation suppresses IRF1-dependent interferon λ and antiviral defense in airway epithelium. *J. Exp. Med.* **210**, 1929–1936 (2013).
45. X. Messeguer, R. Escudero, D. Farré, O. Núñez, J. Martínez, M. M. Albà, PROMO: Detection of known transcription regulatory elements using species-tailored searches. *Bioinformatics* **18**, 333–334 (2002).
46. P. A. Morcos, Y. Li, S. Jiang, Vivo-Morpholinos: A non-peptide transporter delivers Morpholinos into a wide array of mouse tissues. *Biotechniques* **45**, 613–614 (2008).
47. S. Akira, S. Uematsu, O. Takeuchi, Pathogen recognition and innate immunity. *Cell* **124**, 783–801 (2006).
48. B. Beutler, C. Eidenschenk, K. Crozat, J. L. Imler, O. Takeuchi, J. A. Hoffmann, S. Akira, Genetic analysis of resistance to viral infection. *Nat. Rev. Immunol.* **7**, 753–766 (2007).
49. O. Takeuchi, S. Akira, MDA5/RIG-I and virus recognition. *Curr. Opin. Immunol.* **20**, 17–22 (2008).
50. O. O. Koyuncu, I. B. Hogue, L. W. Enquist, Virus infections in the nervous system. *Cell Host Microbe* **13**, 379–393 (2013).
51. D. E. Griffin, Immune responses to RNA-virus infections of the CNS. *Nat. Rev. Immunol.* **3**, 493–502 (2003).
52. L. He, G. J. Hannon, MicroRNAs: Small RNAs with a big role in gene regulation. *Nat. Rev. Genet.* **5**, 522–531 (2004).
53. D. Baltimore, M. P. Boldin, R. M. O'Connell, D. S. Rao, K. D. Taganov, MicroRNAs: New regulators of immune cell development and function. *Nat. Immunol.* **9**, 839–845 (2008).
54. G. R. Stark, I. M. Kerr, B. R. G. Williams, R. H. Silverman, R. D. Schreiber, How cells respond to interferons. *Annu. Rev. Biochem.* **67**, 227–264 (1998).
55. J. W. Schoggins, C. M. Rice, Interferon-stimulated genes and their antiviral effector functions. *Curr. Opin. Virol.* **1**, 519–525 (2011).
56. J. W. Schoggins, S. J. Wilson, M. Panis, M. Y. Murphy, C. T. Jones, P. Bieniasz, C. M. Rice, A diverse range of gene products are effectors of the type I interferon antiviral response. *Nature* **472**, 481–485 (2011).
57. S. J. Robertson, K. J. Lubick, B. A. Freedman, A. B. Carmody, S. M. Best, Tick-borne flaviviruses antagonize both IRF-1 and type I IFN signaling to inhibit dendritic cell function. *J. Immunol.* **192**, 2744–2755 (2014).
58. S. Nair, K. Michaelsen-Preusse, K. Finsterbusch, S. Stegemann-Koniszewski, D. Bruder, M. Grashoff, M. Korte, M. Köster, U. Kalinke, H. Hauser, A. Kröger, Interferon regulatory factor-1 protects from fatal neurotropic infection with vesicular stomatitis virus by specific inhibition of viral replication in neurons. *PLOS Pathog.* **10**, e1003999 (2014).
59. T. Fujita, J. Sakakibara, Y. Sudo, M. Miyamoto, Y. Kimura, T. Taniguchi, Evidence for a nuclear factor(s), IRF-1, mediating induction and silencing properties to human IFN-beta gene regulatory elements. *EMBO J.* **7**, 3397–3405 (1988).
60. Y.-i. Seki, K. Hayashi, A. Matsumoto, N. Seki, J. Tsukada, J. Ransom, T. Naka, T. Kishimoto, A. Yoshimura, M. Kubo, Expression of the suppressor of cytokine signaling-5 (SOCS5) negatively regulates IL-4-dependent STAT6 activation and Th2 differentiation. *Proc. Natl. Acad. Sci. U.S.A.* **99**, 13003–13008 (2002).
61. E.-K. Pauli, M. Schmolke, T. Wolff, D. Viemann, J. Roth, J. G. Bode, S. Ludwig, Influenza A virus inhibits type I IFN signaling via NF-κB-dependent induction of SOCS-3 expression. *PLOS Pathog.* **4**, e1000196 (2008).
62. J. Pothlichet, M. Chignard, M. Si-Tahar, Cutting edge: Innate immune response triggered by influenza A virus is negatively regulated by SOCS1 and SOCS3 through a RIG-I/IFNAR1-dependent pathway. *J. Immunol.* **180**, 2034–2038 (2008).
63. L. N. Akhtar, H. Qin, M. T. Muldowney, L. L. Yanagisawa, O. Kutsch, J. E. Clements, E. N. Benveniste, Suppressor of cytokine signaling 3 inhibits antiviral IFN-β signaling to enhance HIV-1 replication in macrophages. *J. Immunol.* **185**, 2393–2404 (2010).
64. E. Kario, M. D. Marmor, K. Adamsky, A. Citri, I. Amit, N. Amariglio, G. Rechavi, Y. Yarden, Suppressors of cytokine signaling 4 and 5 regulate epidermal growth factor receptor signaling. *J. Biol. Chem.* **280**, 7038–7048 (2005).
65. G. Chan, M. T. Nogalski, A. D. Yurochko, Activation of EGFR on monocytes is required for human cytomegalovirus entry and mediates cellular motility. *Proc. Natl. Acad. Sci. U.S.A.* **106**, 22369–22374 (2009).
66. T. Eierhoff, E. R. Hrincius, U. Rescher, S. Ludwig, C. Ehrhardt, The epidermal growth factor receptor (EGFR) promotes uptake of influenza A viruses (IAV) into host cells. *PLOS Pathog.* **6**, e1001099 (2010).
67. J. Lupberger, M. B. Zeisel, F. Xiao, C. Thumann, I. Fofana, L. Zona, C. Davis, C. J. Mee, M. Turek, S. Gorke, C. Royer, B. Fischer, M. N. Zahid, D. Lavillette, J. Fresquet, F.-L. Cosset, S. M. Rothenberg, T. Pietschmann, A. H. Patel, P. Pessaux, M. Doffoël, W. Raffelsberger, O. Poch, J. A. McKeating, L. Brino, T. F. Baumert, EGFR and EphA2 are host factors for hepatitis C virus entry and possible targets for antiviral therapy. *Nat. Med.* **17**, 589–595 (2011).
68. R. Zhou, G. Hu, A.-Y. Gong, X.-M. Chen, Binding of NF-kappaB p65 subunit to the promoter elements is involved in LPS-induced transactivation of miRNA genes in human biliary epithelial cells. *Nucleic Acids Res.* **38**, 3222–3232 (2010).
69. G. Song, L. Wang, A conserved gene structure and expression regulation of miR-433 and miR-127 in mammals. *PLOS ONE* **4**, e7829 (2009).
70. K. D. Taganov, M. P. Boldin, K.-J. Chang, D. Baltimore, NF-κB-dependent induction of microRNA miR-146, an inhibitor targeted to signaling proteins of innate immune responses. *Proc. Natl. Acad. Sci. U.S.A.* **103**, 12481–12486 (2006).
71. G. Gatto, A. Rossi, D. Rossi, S. Kroening, S. Bonatti, M. Mallardo, Epstein–Barr virus latent membrane protein 1 *trans*-activates miR-155 transcription through the NF-κB pathway. *Nucleic Acids Res.* **36**, 6608–6619 (2008).
72. M. Hayakawa, H. Miyashita, I. Sakamoto, M. Kitagawa, H. Tanaka, H. Yasuda, M. Karin, K. Kikugawa, Evidence that reactive oxygen species do not mediate NF-κB activation. *EMBO J.* **22**, 3356–3366 (2003).
73. A. Nurmi, N. Vartiainen, R. Pihlaja, G. Goldsteins, J. Yrjänheikki, J. Koistinaho, Pyrrolidine dithiocarbamate inhibits translocation of nuclear factor kappa-B in neurons and protects against brain ischaemia with a wide therapeutic time window. *J. Neurochem.* **91**, 755–765 (2004).
74. R. Burrer, B. W. Neuman, J. P. C. Ting, D. A. Stein, H. M. Moulton, P. L. Iversen, P. Kuhn, M. J. Buchmeier, Antiviral effects of antisense morpholino oligomers in murine coronavirus infection models. *J. Virol.* **81**, 5637–5648 (2007).
75. S.-H. Lai, D. A. Stein, A. Guerrero-Plata, S.-L. Liao, T. Ivanciuc, C. Hong, P. L. Iversen, A. Casola, R. P. Garofalo, Inhibition of respiratory syncytial virus infections with morpholino oligomers in cell cultures and in mice. *Mol. Ther.* **16**, 1120–1128 (2008).
76. T. S. Deas, C. J. Bennett, S. A. Jones, M. Tilgner, P. Ren, M. J. Behr, D. A. Stein, P. L. Iversen, L. D. Kramer, K. A. Bernard, P.-Y. Shi, In vitro resistance selection and in vivo efficacy of morpholino oligomers against West Nile virus. *Antimicrob. Agents Chemother.* **51**, 2470–2482 (2007).
77. H. Francis, K. McDaniel, Y. Han, X. Liu, L. Kennedy, F. Yang, J. McCarra, T. Zhou, S. Glaser, J. Venter, L. Huang, P. Levine, J.-M. Lai, C.-G. Liu, G. Alpini, F. Meng, Regulation of the extrinsic apoptotic pathway by microRNA-21 in alcoholic liver injury. *J. Biol. Chem.* **289**, 27526–27539 (2014).
78. P. L. Iversen, V. Arora, A. J. Acker, D. H. Mason, G. R. Devi, Efficacy of antisense morpholino oligomer targeted to c-*myc* in prostate cancer xenograft murine model and a Phase I safety study in humans. *Clin. Cancer Res.* **9**, 2510–2519 (2003).
79. M. Kinali, V. Arechavala-Gomeza, L. Feng, S. Cirak, D. Hunt, C. Adkin, M. Guglieri, E. Ashton, S. Abbs, P. Nihoyannopoulos, M. E. Garralda, M. Rutherford, C. McCulley, L. Popplewell, I. R. Graham, G. Dickson, M. J. A. Wood, D. J. Wells, S. D. Wilton, R. Kole, V. Straub, K. Bushby, C. Sewry, J. E. Morgan, F. Muntoni, Local restoration of dystrophin expression with the morpholino oligomer AVI-4658 in Duchenne muscular dystrophy: A single-blind, placebo-controlled, dose-escalation, proof-of-concept study. *Lancet Neurol.* **8**, 918–928 (2009).
80. A. Nazmi, K. Dutta, A. Basu, Antiviral and neuroprotective role of octaguanidinium dendrimer-conjugated morpholino oligomers in Japanese encephalitis. *PLOS Negl. Trop. Dis.* **4**, e892 (2010).
81. T. Kimura, M. Sasaki, M. Okumura, E. Kim, H. Sawa, Flavivirus encephalitis: Pathological aspects of mouse and other animal models. *Vet. Pathol.* **47**, 806–818 (2010).
82. F. Y. Liew, D. Xu, E. K. Brint, L. A. J. O'Neill, Negative regulation of Toll-like receptor-mediated immune responses. *Nat. Rev. Immunol.* **5**, 446–458 (2005).
83. M. Ceppi, P. M. Pereira, I. Dunand-Sauthier, E. Barras, W. Reith, M. A. Santos, P. Pierre, MicroRNA-155 modulates the interleukin-1 signaling pathway in activated human monocyte-derived dendritic cells. *Proc. Natl. Acad. Sci. U.S.A.* **106**, 2735–2740 (2009).
84. A. Mukherjee, A. M. Di Bisceglie, R. B. Ray, Hepatitis C virus-mediated enhancement of microRNA miR-373 impairs the JAK/STAT signaling pathway. *J. Virol.* **89**, 3356–3365 (2015).
85. D. Lagos, G. Pollara, S. Henderson, F. Gratrix, M. Fabani, R. S. B. Milne, F. Gotch, C. Boshoff, miR-132 regulates antiviral innate immunity through suppression of the p300 transcriptional co-activator. *Nat. Cell Biol.* **12**, 513–519 (2010).

86. B.-C. Ho, I.-S. Yu, L.-F. Lu, A. Rudensky, H.-Y. Chen, C.-W. Tsai, Y.-L. Chang, C.-T. Wu, L.-Y. Chang, S.-R. Shih, S.-W. Lin, C.-N. Lee, P.-C. Yang, S.-L. Yu, Inhibition of miR-146a prevents enterovirus-induced death by restoring the production of type I interferon. *Nat. Commun.* **5**, 3344 (2014).
87. Y. Li, X. Fan, X. He, H. Sun, Z. Zou, H. Yuan, H. Xu, C. Wang, X. Shi, MicroRNA-466l inhibits antiviral innate immune response by targeting interferon-alpha. *Cell. Mol. Immunol.* **9**, 497–502 (2012).
88. Y. Chen, J. Chen, H. Wang, J. Shi, K. Wu, S. Liu, Y. Liu, J. Wu, HCV-induced miR-21 contributes to evasion of host immune system by targeting MyD88 and IRAK1. *PLOS Pathog.* **9**, e1003248 (2013).
89. J. I. Henke, D. Goergen, J. Zheng, Y. Song, C. G. Schüttler, C. Fehr, C. Junemann, M. Niepmann, microRNA-122 stimulates translation of hepatitis C virus RNA. *EMBO J.* **27**, 3300–3310 (2008).

Acknowledgments: We are grateful to P. K. Roy [National Brain Research Centre (NBRC)] for helping with statistical analysis of the data. We are obliged to S. K. Sharma (NBRC), E. Sen (NBRC), D. Schubert (Salk Institute), S. Levison (Rutgers University), A. Krishnan (Institute of Molecular Medicine), G. R. Medigeshi (Translational Health Science and Technology Institute), D. Chattopadhyay (Amity University), and P. Chattopadhyay (All India Institute of Medical Science) for providing cell lines and plasmids. We acknowledge K. Dutta (University of Laval, Quebec, Canada) for critically reading the manuscript and giving insightful comments. We thank A. Nazmi (University of Gothenburg, Sweden) for his valuable suggestions. We are highly thankful to M. Dogra for his technical assistance. **Funding:** The study was supported by the NBRC Core Fund and a Tata Innovation Fellowship (BT/HRD/35/01/02/2014) to A.B. from the Department of Biotechnology, Ministry of Science and Technology, Government of India. B.H. is supported by a postdoctoral fellowship from the Indian Council of Medical Research, Government of India (80/901/2014-ECD-I). **Author contributions:** A.B. and B.H. designed the study, generated the hypothesis, analyzed the data, and wrote the manuscript. B.H. performed all of the experiments, interpreted the results, and executed statistical analysis. K.L.K. helped in handling and performing all animal experiments. All of the authors read and approved the final manuscript. **Competing interests:** The authors declare that they have no competing interests.

Submitted 22 February 2016
Accepted 27 January 2017
Published 14 February 2017
10.1126/scisignal.aaf5185

Citation: B. Hazra, K. L. Kumawat, A. Basu, The host microRNA miR-301a blocks the IRF1-mediated neuronal innate immune response to Japanese encephalitis virus infection. *Sci. Signal.* **10**, eaaf5185 (2017).

The host microRNA miR-301a blocks the IRF1-mediated neuronal innate immune response to Japanese encephalitis virus infection

Bibhabasu Hazra, Kanhaiya Lal Kumawat and Anirban Basu

(February 14, 2017)
Science Signaling **10** (466), eaaf5185. [doi: 10.1126/scisignal.aaf5185]

Science Signaling (ISSN 1937-9145) is published weekly, except the last December, by the American Association for the Advancement of Science, 1200 New York Avenue, NW, Washington, DC 20005.

AMERICAN SOCIETY FOR MICROBIOLOGY | mBio®

RESEARCH ARTICLE

Involvement of RIG-I Pathway in Neurotropic Virus-Induced Acute Flaccid Paralysis and Subsequent Spinal Motor Neuron Death

Meenakshi Bhaskar,[a] Sriparna Mukherjee,[a]* Anirban Basu[a]

[a]National Brain Research Centre, Manesar, Haryana, India

ABSTRACT Poliomyelitis-like illness is a common clinical manifestation of neurotropic viral infections. Functional loss and death of motor neurons often lead to reduced muscle tone and paralysis, causing persistent motor sequelae among disease survivors. Despite several reports demonstrating the molecular basis of encephalopathy, the pathogenesis behind virus-induced flaccid paralysis remained largely unknown. The present study for the first time aims to elucidate the mechanism responsible for limb paralysis by studying clinical isolates of Japanese encephalitis virus (JEV) and Chandipura virus (CHPV) responsible for causing acute flaccid paralysis (AFP) in vast regions of Southeast Asia and the Indian subcontinent. An experimental model for studying virus-induced AFP was generated by intraperitoneal injection of 10-day-old BALB/c mice. Progressive decline in motor performance of infected animals was observed, with paralysis being correlated with death of motor neurons (MNs). Furthermore, we demonstrated that upon infection, MNs undergo an extrinsic apoptotic pathway in a RIG-I-dependent fashion via transcription factors pIRF-3 and pIRF-7. Both gene-silencing experiments using specific RIG-I-short interfering RNA and *in vivo* morpholino abrogated cellular apoptosis, validating the important role of pattern recognition receptor (PRR) RIG-I in MN death. Hence, from our experimental observations, we hypothesize that host innate response plays a significant role in deterioration of motor functioning upon neurotropic virus infections.

IMPORTANCE Neurotropic viral infections are an increasingly common cause of immediate or delayed neuropsychiatric sequelae, cognitive impairment, and movement disorders or, in severe cases, death. Given the highest reported disability-adjusted life years and mortality rate worldwide, a better understanding of molecular mechanisms for underlying clinical manifestations like AFP will help in development of more effective tools for therapeutic solutions.

KEYWORDS acute flaccid paralysis, neurotropic virus, motor neuron, cell death, pattern-recognition receptor RIG-I

Virus-induced acute flaccid paralysis (AFP) or viral myelitis, including complex poliomyelitis-like syndrome, a term coined by T. Solomon in 1998 (1), has emerged as a serious health concern after being rereported in various forms of epidemics annually (2–10). Despite the success of the World Health Organization's global polio eradication initiative, AFP remains a prevalent disease in children below the age of 15 (11, 12). Active surveillance of AFP following the polio vaccine era has linked the unusual rise of poliomyelitis cases to non-polio viral infections (13–15). Asymmetric flaccid weakness, a clinical manifestation of AFP, may progress to permanent limb paralysis in severe-outcome patients, adding to disability-adjusted life years (16). Owing to its clinical importance with no specific treatment available, a lack of an experimental model to

Citation Bhaskar M, Mukherjee S, Basu A. 2021. Involvement of RIG-I pathway in neurotropic virus-induced acute flaccid paralysis and subsequent spinal motor neuron death. mBio 12:e02712-21. https://doi.org/10.1128/mBio.02712-21.

Invited Editor Emily Hemann, CDC

Editor Nisha K. Duggal, CDC

Address correspondence to Anirban Basu, anirban@nbrc.ac.in or anirban.nbrc@gmail.com.

*Present address: Sriparna Mukherjee, Department of Pharmacology and Physiology, Pavilion Roger-Gaudry, Universite de Montreal, Montreal, Quebec, Canada.

This article is a direct contribution from Anirban Basu, a Fellow of the American Academy of Microbiology, who arranged for and secured reviews by Nihal Altan-Bonnet, National Institutes of Health, and Mukesh Kumar, Georgia State University.

Received 14 September 2021
Accepted 12 October 2021
Published 16 November 2021

understand the etiology of virus-induced AFP further limits the development of potential therapies.

Like polio, many emerging viral infections, such as enterovirus, West Nile virus (WNV), and Japanese encephalitis virus (JEV), are causing AFP outbreaks annually due to endemic circulation of virus among populations (17–22). JEV and CHPV are two such viruses, endemic to Southeast Asia and the Indian subcontinent, which are mainly responsible for causing AFP and encephalitis in young children (23). Patients suffering from JEV and CHPV principally develop flu-like symptoms and characteristic features of lower motor neuron (MN) disease, such as lower limb wastage and flaccid weakness in affected populations (24, 25). Historically, the first clinical case of JEV-induced AFP was identified in 1945 on Okinawa Island, where the native population presented features of flaccid paralysis with sudden onset of fever and headache. When observed microscopically, autopsy samples of JE-positive patients displayed damaged anterior horn cells that were histologically similar to the lesions observed in acute poliomyelitis disease (26). Extensive electrophysiological and radiological studies performed on conscious JE-infected patients further suggested a role of anterior horn cells in JEV-induced muscle wasting (27). Additionally, magnetic resonance imaging (MRI) scans showed abnormal signal intensity on T2-weighted images of spine, indicating anterior horn cell injury in convalescent patients (28). Consistent with the clinical case reports, the anatomical basis of virus-induced AFP was first demonstrated in mice after neuroadapted Sindbis virus infection (29). Later, various studies conducted showed evidence of apoptotic injury in mouse central nervous system (CNS) upon EV71, WNV, reovirus, and Sindbis virus infection (30–34); however, the precise mechanism behind MN death and virus-induced AFP remained elusive.

Research in our laboratory previously defined a role of oxidative stress and neuroinflammation in brain, which answered some of the basic questions of virus-induced encephalitis (35–40). Therefore, in this study, we developed an experimental model of virus-induced AFP that replicates all features of clinical AFP. Interestingly, we found that viral replication in lumbar cord correlates with behavioral impairments and paralysis in diseased mice, with RIG-I signaling playing a central role in activating the extrinsic apoptotic pathway. Thus, overall, we addressed two important questions of viral AFP. First, we described that sustained activation of RIG-I/pIRF3-7 signaling upon infection triggers the host endogenous apoptotic pathway, which, being a part of the antiviral response system, leads to MN death. Second, our investigations further highlighted that RIG-I-induced MN death during neurotropic virus infection is independent and distinct from well-described type 1 interferon (IFN)-induced apoptosis.

RESULTS

Characterization of neurotropic virus-induced AFP. In this study, we screened two clinical isolates of neurotropic virus, JEV (strain GP-78) and CHPV (strain 1653514), for their ability to induce flaccid paralysis in BALB/c mice (Fig. 1A). Both viral strains induced AFP by day 5 postinfection (pi) for JEV and day 2 pi for CHPV in mice. The degree of virus-induced paralysis was accurately determined by performing series of behavioral tests. Animals were scored on a scale of 0 to 3 to study general locomotion in mice (GLB score) (Fig. 1B), ranging from the ability to walk freely to no movement at all. Postinfection, both experimental groups showed significant differences in GLB score compared to respective age-matched controls. For JEV, 3/5 animals studied displayed hind leg inhibition with severe limp at day 5 of infection, while 2/5 animals exhibited features of tiptoe or knuckle walking. With disease progression (7 days pi [dpi]), 4/5 animals in the JEV group exhibited complete paralysis of hindlimbs (GLB score = 3) with zero movement, while 1/5 displayed severe limping. Akin to the JEV group, mice infected with CHPV also showed significantly higher GLB scores than mock-infected animals. For CHPV, 3/5 mice developed hind leg inhibition with severe limp shortly after infection (2 dpi), while 4/5 mice showed complete paralysis of lower limbs by day 3 pi. To further assess MN degeneration, hindlimb clasping score (HLC)

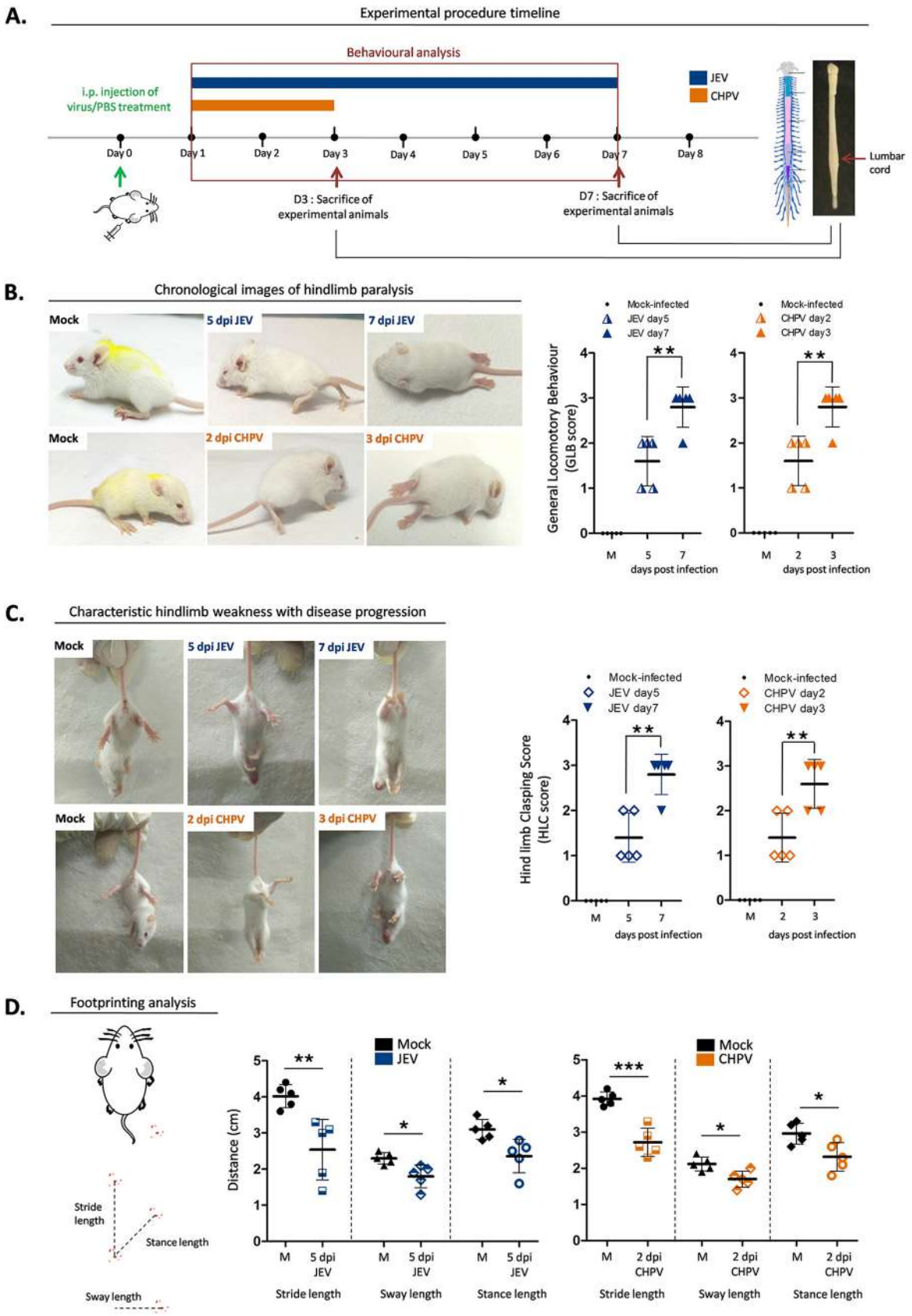

FIG 1 Japanese encephalitis virus and Chandipura virus induce AFP in 10-day-old BALB/c mice. (A) Pups were either mock infected using PBS or inoculated intraperitoneally with 3×10^4 PFU of JEV or 1×10^4 PFU of CHPV. Animals were scored daily until clinical features of

(Continued on next page)

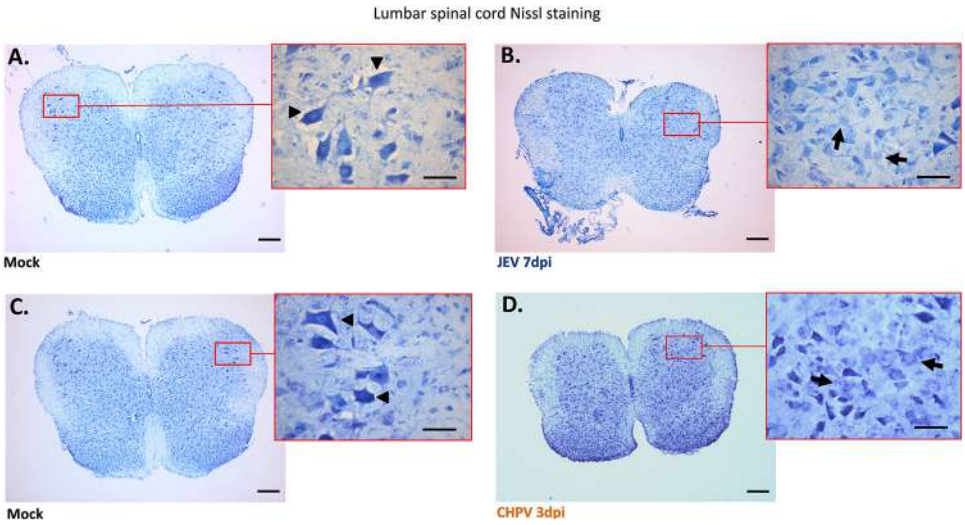

FIG 2 Pathology of lumbar motor neurons (MNs) following JEV and CHPV infection in mice. Ten-day-old BALB/c pups were either mock infected with PBS or inoculated intraperitoneally with 3×10^4 PFU of JEV or 1×10^4 PFU of CHPV in a 25-μl volume. Animals were examined daily and sacrificed at day 7 pi for JEV and day 3 pi for CHPV, when pups displayed complete hindlimb paralysis with difficult or no movement at all. Thin sections of 20-μm thickness prepared from both mock-infected and virus-infected lumbar cord tissue were examined using Nissl stain. (A and C) Coronal lumbar cord sections of respective age-matched control animal (mock infected) with red-outlined boxes representing enlarged images of anterior horn SC (spinal cord) with healthy MNs indicated by black arrowheads. (B and D) Representative image of infected lumbar cord sections upon JEV and CHPV infection with magnified area displaying dying MNs indicated by black arrows. Scale bar denotes 50 μm and 200 μm using oil magnification. Data are representative of a minimum of three independent experiments performed.

(Fig. 1C) was calculated, wherein the infected group again displayed significantly higher scores than their control littermates. Interestingly, from both the JEV and CHPV experimental groups, 2/5 animals developed partial retraction of hindlimbs toward midline when suspended freely in air, while with progression of infection, 4/5 animals in the JEV and 3/5 animals in the CHPV group developed complete retraction of hindlimbs (HLC score, 3). In a further attempt to analyze gait abnormalities, we did footprint analysis, wherein significant decrease in stride length, sway length, and stance length were recorded compared with mock-infected animals (Fig. 1D).

To further correlate clinical observations of AFP with motor neuron pathology, we performed Nissl staining using spinal cord (SC) sections. Selective loss of motor neurons was observed exclusively in anterior horn of the lumbar region compared with cervical and thoracic SC sections of the same animal (data not shown). Both JEV- and CHPV-infected lumbar sections displayed features of chromatolysis, like eccentric nucleus and cellular swelling of MN (Fig. 2B and D), compared to healthy MNs observed in mock-infected mice (Fig. 2A and C). Thus, collectively these findings suggest that virus infection not only impaired overall motor coordination but also induced clinical AFP with degenerating motor neurons.

Virus titer in lumbar SC corresponds to disease progression. To determine whether active replication of virus is associated with disease severity, we next performed plaque

FIG 1 Legend (Continued)
hindlimb paralysis appeared. Pups were sacrificed and lumbar cord tissue was harvested at days 1, 3, 5, and 7 postinfection (pi) for JEV and days 1, 2, and 3 pi for CHPV. Blue bar charts represent JEV infection and orange bar charts represent CHPV infection. (B) Characteristic changes in locomotion of infected animals with representative posture of duck foot motion and hindlimb paralysis were scored quantitatively and analyzed as GLB (general locomotory behavior) score. Data are represented as means ± standard deviations (SD) for 5 animals per group where *P* values were determined (*, $P < 0.05$; **, $P < 0.01$; ***, $P < 0.001$) using one-way ANOVA followed by *post hoc* Bonferroni test. (C) Altered hindlimb clasping phenotype with typical posture of hindlimbs retracted toward the midline or away from midline was scored as HLC (hindlimb clasping) score where data are represented as means ± SD for 5 animals per group, with statistical significance being determined (*, $P < 0.05$; **, $P < 0.01$; ***, $P < 0.001$) using one-way ANOVA followed by *post hoc* Bonferroni correction. (D) Severity in gait of the animals was quantified by footprinting analysis where error bars are represented as mean ± SD for 5 animals, with *P* values determined (*, $P < 0.05$; **, $P < 0.01$; ***, $P < 0.001$) using two-tailed paired *t* test.

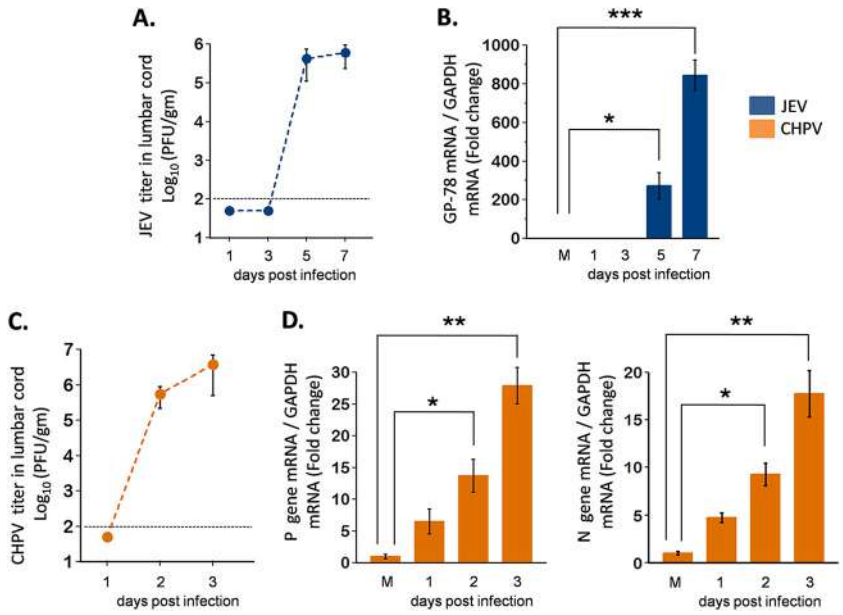

FIG 3 Viral titer in lumbar spinal cord (SC) of infected mice. Ten-day-old BALB/c pups were either PBS injected or infected with clinical isolates, 3×10^4 PFU of JEV or 1×10^4 PFU of CHPV, intraperitoneally. Viral titers were determined from infected lumbar cord tissue in a daywise manner (days 1, 3, 5, and 7 after JEV infection and days 1, 2, and 3 after CHPV infection) for studying viral kinetics with disease progression. Blue bar charts represent JEV-infected data and orange bar charts represent CHPV-infected data. (A and C) Lumbar tissue homogenates prepared and pooled from 2 mice for each time point of infection were analyzed for infectious virus count using plaque assay. Dashed lines represent the limit of detection of plaque assays for all experiments performed. (B and D) Total RNA was extracted from lumbar SC tissue for analyzing relative abundance of viral mRNA using qRT-PCR, where GAPDH was used as the loading control. Data represent mean ± standard deviation (SD) from a minimum of 3 independent experiments, where *P* values were determined (*, $P < 0.05$; **, $P < 0.01$; ***, $P < 0.001$) using one-way ANOVA followed by *post hoc* Bonferroni test.

assays using lumbar cord homogenates at various dpi. To our interest, infectious viral particles were detected only at day 5 and 7 pi for JEV and day 2 and 3 pi for CHPV, suggesting inability of virus to penetrate the blood-brain barrier (BBB) at early dpi (Fig. 3A and C). Additionally, to confirm *in vivo* viral replication, two-step quantitative PCRs targeting glycoprotein gene of JEV and P, N gene of CHPV were performed to detect viral RNA extracted from lumbar cords at various time points pi. Significant upregulation of GP-78 (Fig. 3B) at days 5 and 7 pi for JEV and P, N gene (Fig. 3D) at days 2 and 3 pi for CHPV were detected. Overall, results from the quantitative real-time PCR (qRT-PCR) analysis and plaque assay paralleled the behavioral deficits observed in mice, indicating an association between viral replication and paralysis onset.

JEV and CHPV infect motor neuron both *in vivo* and *in vitro*. To determine whether virus-induced AFP is linked to active infection of MNs, we performed immunohistochemistry (IHC) with lumbar sections using anti-JEV NS3 and anti-CHPV P-protein antibody. Motor neurons were identified using anti-SMI32, a specific marker for anterior horn cells, which appeared intact with no immunoreactivity toward viral antigen in mock-infected samples. Both JEV- and CHPV-infected pups displayed clear colocalization of SMI32 and NS3 and P-protein at days 5 and 7 pi for JEV and days 2 and 3 pi for CHPV (Fig. 4A and D), with quantification graphs attached (Fig. 4C and F). Interestingly, viral protein kinetics (blots) showed significant upregulation of NS3 at day 7 pi for JEV and P-protein at day 3 pi for CHPV (Fig. 4B and E), which is in line with IHC data and further corroborates the association of MN infection with AFP.

Having shown that viral replication in MN is associated with onset of paralysis, we next studied permissiveness of virus in NSC34 cells to further investigate molecular events contributing to AFP pathogenesis. For this, we infected NSC34 cells with JEV and CHPV at a multiplicity of infection (MOI) of 1 and 0.1, respectively, and harvested

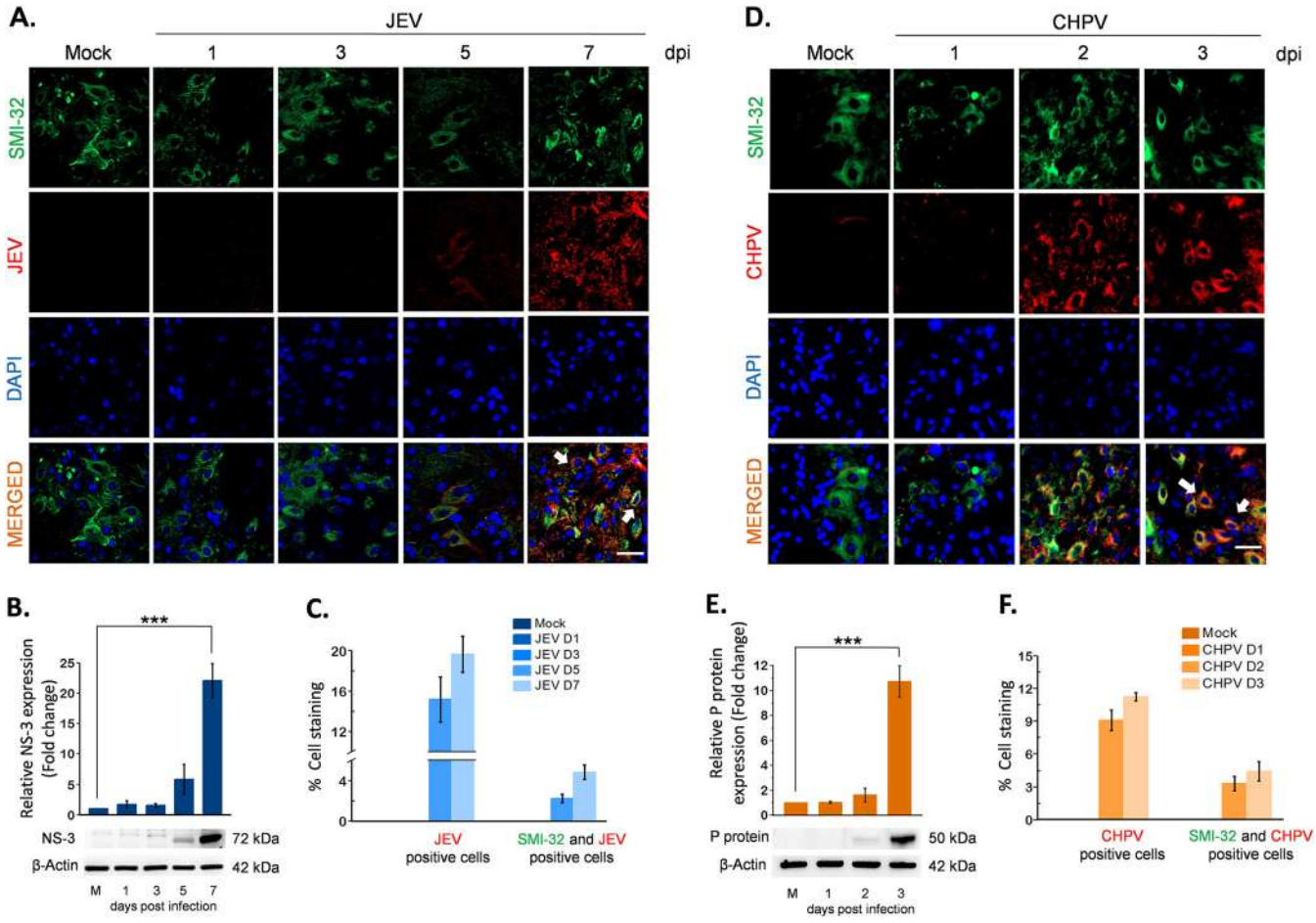

FIG 4 Virus-induced AFP correlates with spread of viral antigen in lumbar motor neurons. Ten-day-old BALB/c mice were either mock infected or inoculated intraperitoneally with 3×10^4 PFU of JEV or 1×10^4 PFU of CHPV. Infected cord tissues were collected in a daywise manner as indicated for studying paralysis onset and disease progression. Blue bar charts represent JEV infected data, and orange bar charts represent CHPV infected data. (A and D) Lumbar cord sections were double stained for motor neuron marker SMI-32 and viral antigen NS3 for JEV and P-protein for CHPV infection. Representative epifluorescence images show colocalization of viral antigen with MN marker and DAPI, indicated by white arrows in respective panels. Scale bar denotes 50 μm. (B and E) Lumbar cord lysates from both PBS-injected and virus-infected pups were analyzed using Western blotting to determine relative abundance of viral proteins (NS3 for JEV and P-protein for CHPV). (C and F) Representative graphs showing percentage of JEV- and CHPV-infected cells along with double-positive cells for SMI32 (motor neuron marker) and viral protein markers in respective lumbar cord sections. Data here represent mean ± SD from a minimum of 3 independent experiments, where statistical significance (*, $P < 0.05$; **, $P < 0.01$; ***, $P < 0.001$; NS, nonsignificant) was calculated using one-way ANOVA followed by *post hoc* Bonferroni correction.

samples at various hours postinfection (hpi) to study time-dependent kinetics of viral replication. Phase-contrast images were captured for monitoring cellular health through brief periods of infection, where NSC34 cells displayed cytopathic changes characterized by rounding up of cells by 12 and 24 hpi for JEV and 6 and 12 hpi for CHPV (see Fig. S1 in the supplemental material). To confirm active replication of virus in NSC34 cells, we performed immunostaining with virus-specific antibodies. No signal was detected in mock-infected cells, while with progression of infection, increased viral staining was observed both in JEV (Fig. 5A, v)- and CHPV (Fig. 5B, v)-infected NSC34 cells. In addition to this, terminal deoxynucleotidyltransferase-mediated dUTP-biotin nick end labeling (TUNEL)-positive cells were also observed at 24 hpi for JEV (Fig. 5A, vi) and 12 hpi for CHPV (Fig. 5B, vi), suggesting a correlation between apoptotic death of MN and flaccid paralysis.

Next, to study time-dependent kinetics of viral replication, we performed qRT-PCR analysis at various hpi. Significant upregulation of viral copies was evident at 6, 12, and 24 hpi (Fig. 5A, ii), an observation in parallel with time-dependent reduction of viability from 100% in control to 63.08% in 24-h JEV-infected NSC34 cells (Fig. 5A, i). In contrast, infection with CHPV reduced NSC34 viability from 100% to 56% (Fig. 5B, ii) within 12

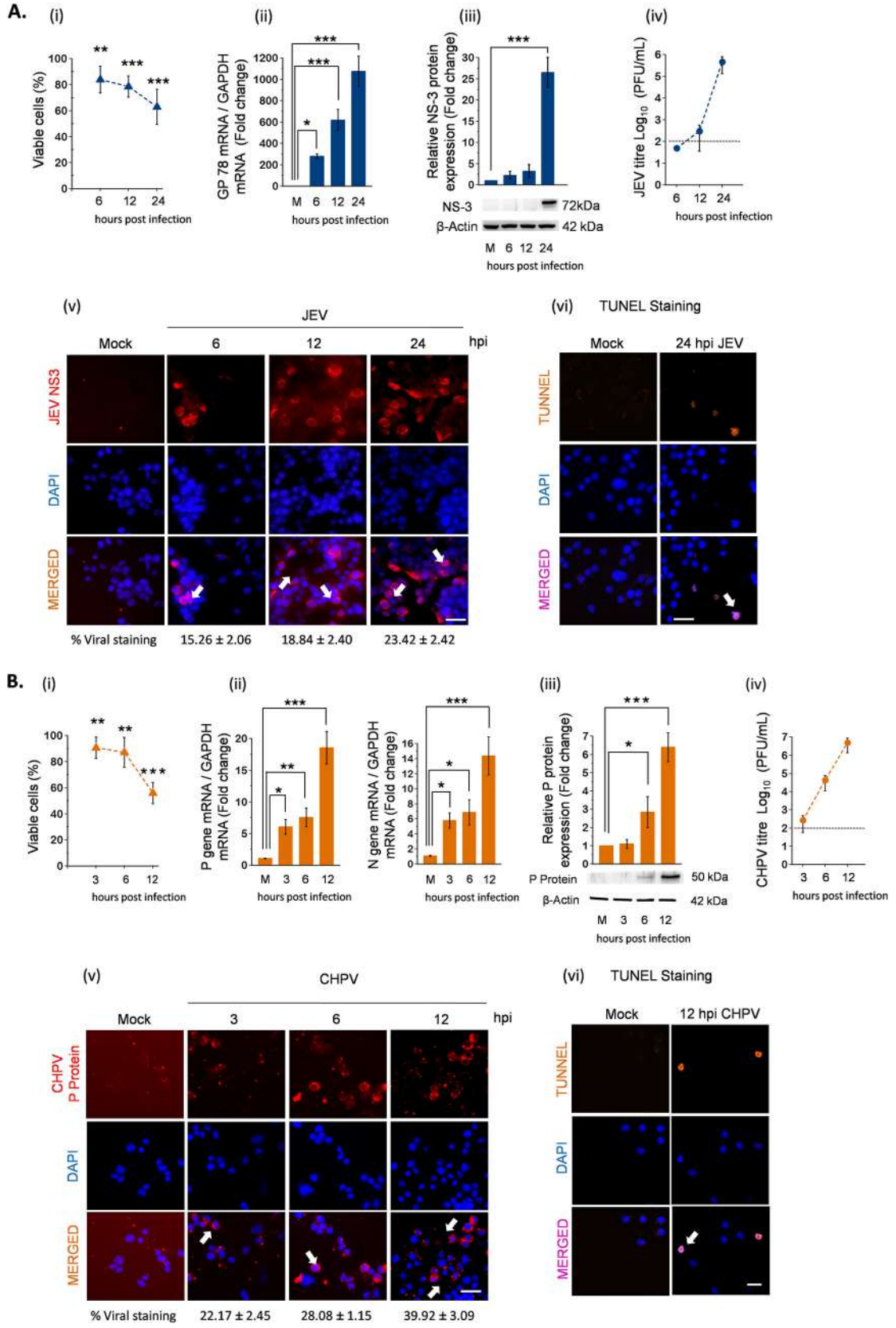

FIG 5 JEV and CHPV replicates actively in motor neuron cell line NSC34. Cells were either left untreated or were infected with JEV at an MOI of 1 and CHPV at an MOI of 0.1 for various times. Blue bar charts represent JEV infection data and orange bar

(Continued on next page)

FIG 5 Legend (Continued)

hpi, concomitant with increased amounts of viral transcripts visible by 3, 6, and 12 hpi (Fig. 5B, ii). Infectious viral particles were detected readily in supernatants obtained upon infection from both viruses studied (Fig. 5A and B, iv) with an increased expression of viral protein NS3 in JEV- and P in CHPV-infected cells (Fig. 5A and B, iii). Additionally, cytokine bead array (CBA) analysis of culture supernatant obtained upon infection further substantiated that seeded NSC34 cells were dying due to active replication of virus and not because of neuroinflammation (Fig. S2).

JEV and CHPV infection induces caspase-dependent extrinsic apoptosis in MN. Having shown that viral replication leads to apoptosis *in vitro*, we next wanted to determine which apoptotic pathway is activated in dying MNs. For this, we examined expression levels of various caspases, including caspase-8, caspase-9, and caspase-3, with their associated proteins BAX, BCL2, and c-PARP postinfection. Both *in vivo* and *in vitro* studies revealed significant overexpression of cleaved (c)-casp-8, c-casp-3, and c-PARP protein with no active form of caspase-9 being detected. Distinct upregulation of c-casp8 was observed in NSC34 cells at 12 hpi for JEV and 6 hpi for CHPV, which later declined significantly at 24 hpi for JEV and 12 hpi for CHPV (Fig. 6A, ii). Interestingly, a similar pattern of c-casp8 was observed *in vivo* at day 5 pi for JEV and day 2 pi for CHPV. In addition to this, the active form of casp-3 was detected at 24 hpi *in vitro* and day 7 pi *in vivo* upon JEV and 12 hpi *in vitro* and day 3 pi *in vivo* upon CHPV treatment (Fig. 6A). Further, to validate that MNs were dying via caspase-dependent pathways only, we performed experiments with Z-VAD-FMK, a pancaspase inhibitor. Pretreatment with Z-VAD-FMK attenuated expression levels of cleaved caspases and significantly reduced apoptosis in NSC34 cells compared with respective virus-infected sample (Fig. 6B and C, i). Cytosolic casp3/7 activity was greatly reduced in Z-VAD-treated cells compared with untreated samples (Fig. 6B and C, iv). Plaque assays further confirmed that reduced c-casp-3 in Z-VAD-FMK-treated cells was purely due to inhibition of apoptosis and not because of compromised viral replication (Fig. 6B and C, ii and iii).

JEV and CHPV infection activates RIG-I pathway. Next, we studied expression level of RIG-I, a well-described PRR involved in initiating antiviral signaling upon infection, both in infected lumbar tissue and NSC34 cells. Immunoblot analysis showed significant upregulation of RIG-I at days 5 and 7 pi for JEV and days 2 and 3 pi for CHPV in mice, with similar trends in infected NSC34 cells, where marked upregulation of RIG-I was evident by 6 hpi for JEV and 3 hpi for CHPV (Fig. 7A, i and ii). A transient upregulation of phosphorylated IRF3 and pIRF7, critical markers of the RIG-I/interferon signaling axis, was detected at 5 dpi for JEV and 2 dpi for CHPV that eventually declined at later days of infection. Consistent with our *in vivo* data, infected NSC34 cells showed similar trends of pIRF3 and pIRF7 at 12 hpi for JEV and 6 hpi for CHPV that declined over time. Activation of type 1 interferon signaling was confirmed by qRT-PCR analysis of IFN-α and IFN-β, both in infected lumbar tissue and NSC34 cells by day 5 pi *in vivo* and 6 hpi *in vitro* upon JEV and day 2 pi *in vivo* and 3 hpi *in vitro* upon CHPV (Fig. 7B, i and ii).

Thereafter, we employed short interfering RNA (siRNA)-mediated silencing to knock down RIG-I expression to validate its role in virus-induced caspase-dependent death of MNs. Gene silencing using specific RIG-I (Ddx58) esiRNA significantly downregulated

charts represent CHPV infection data. (A and B, i) Percent cell viability of NSC34 cells after JEV and CHPV infection quantified at various time points using WTS assay. (ii) Total RNA was extracted from both mock and experimental NSC34 cells following JEV and CHPV infection at the indicated time points. Relative abundance of viral transcripts was determined using qRT-PCR analysis as fold change, where GAPDH was used as the loading control. (iii) Cell lysates prepared from both mock-infected and virus-infected NSC34 cells were subjected to Western blot analysis at the indicated time points for studying viral protein kinetics. Densitometric analysis was performed with β-actin as a loading control to determine fold change expression of indicated proteins. (iv) Viral titer in NSC34 culture supernatant was determined using plaque assay at indicated time points after JEV and CHPV infection. Dashed lines represent the limit of detection of plaque assays for all experiments conducted. (v) Representative immunostaining of NSC34 cells with antibodies against viral protein NS3 (JEV) and P-protein (CHPV) with nuclear marker DAPI. White arrows show populations of infected NSC34 cells. Scale bar denotes 100 μm. (vi) Representative TUNEL staining of JEV and CHPV at late time points of infection with DAPI stained in blue. Scale bar denotes 100 μm. Here, data represent mean $\pm$ SD from a minimum of 3 independent experiments, where statistical significance (*, $P < 0.05$; **, $P < 0.01$; ***, $P < 0.001$; NS, nonsignificant) was calculated using one-way ANOVA followed by *post hoc* Bonferroni correction.

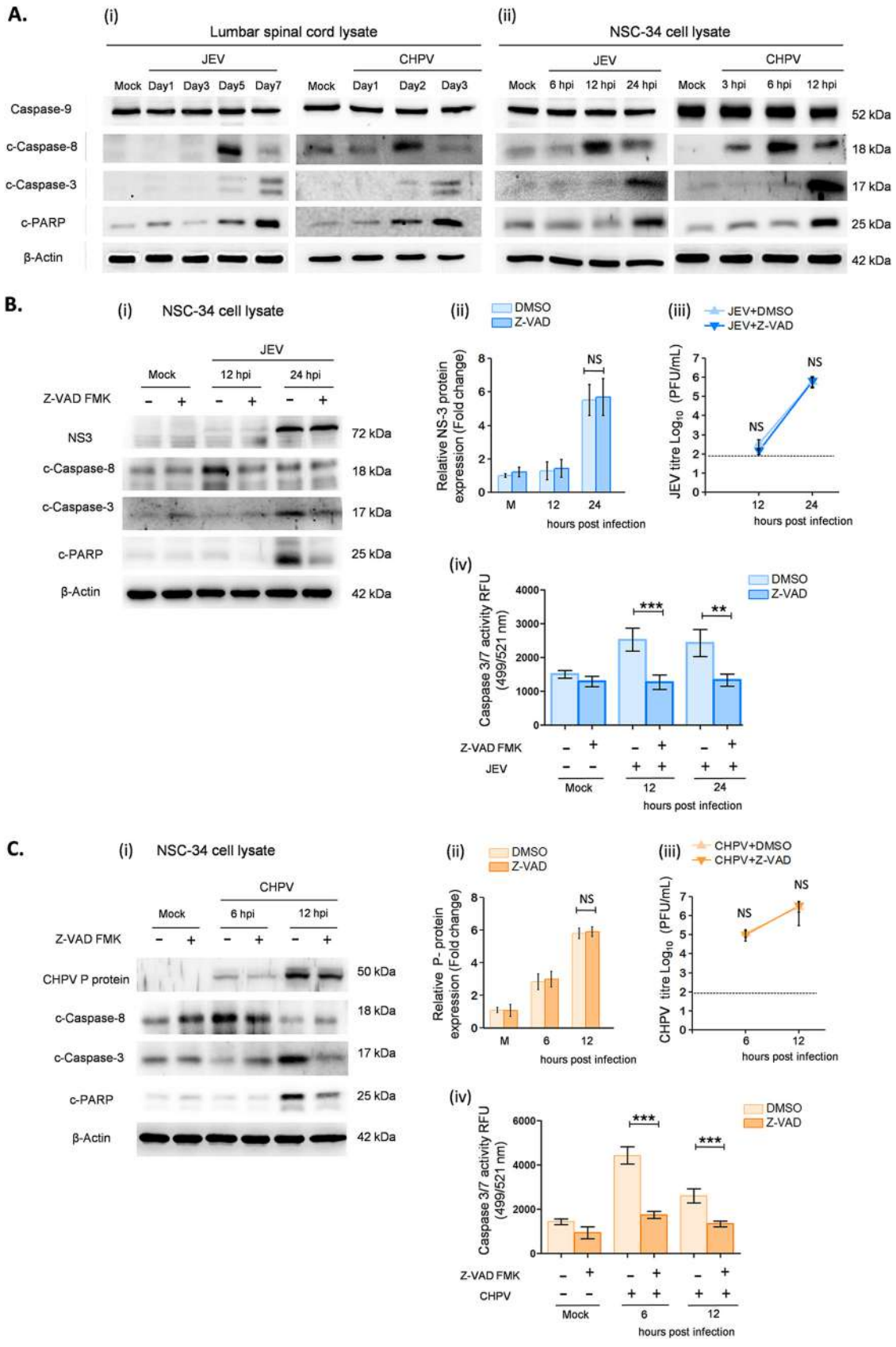

FIG 6 JEV and CHPV infection induces extrinsic apoptosis of motor neurons. For *in vivo* experiments, 10-day-old BALB/c mice were either mock infected or inoculated intraperitoneally with 3×10^4 PFU of JEV or 1×10^4 PFU of CHPV, and for *in vitro*

(Continued on next page)

cleaved caspases and rescued apoptosis at 12 and 24 hpi for JEV and 6 and 12 hpi for CHPV (Fig. 8A and B) with survival of live-NSC34 cells (Fig. S5). However, no changes in viral protein expression (Fig. 8A and B, ii) were detected, indicating that downregulation of apoptotic effector proteins upon gene silencing were not due to impaired viral replication. In addition to this, we performed qRT-PCR analysis and plaque assays to further substantiate our findings, which, in parallel to our observations, showed no significant differences in viral replication (Fig. 8A and B, iii and iv). There was significant decrease in pIRF3 and pIRF7 expression at 12 hpi for JEV and 6 hpi for CHPV in RIG-I-transfected NSC34 compared with the respective negative control. In line with immunoblot analysis, siRNA-mediated RIG-I silencing downregulated type 1 interferon production in both JEV- and CHPV-infected cells (Fig. S3), indicating that upon infection both viruses activate the RIG-I/pIRF3-7/interferon axis to initiate virus-induced apoptosis.

RIG-I-mediated apoptosis is independent of type 1 interferon pathway. Having shown that siRNA-mediated RIG-I silencing downregulated IFN expression and rescued MN death, we next determined the direct role of IFN signaling in virus-induced apoptosis. To address this, we performed two experiments, first with interferon-responsive cell line NSC34, where the receptor antibody neutralization assay was carried out to block any downstream IFN signaling, and second with the interferon-unresponsive cell line Vero. Surprisingly, in both experiments, JEV and CHPV led to apoptosis of NSC34 and Vero cells with distinct upregulation of c-casp3 and c-PARP proteins (Fig. 9A to C). NSC34 cells upon infection displayed no significant changes in the active form of casp-3 and viral protein expression for all three conditions studied (Fig. 9A and B, ii). Similar to NSC34 cells, Vero cells displayed cytopathic changes like rounding up of cells and refraction upon infection (data not shown), suggesting that both viruses induce apoptosis independent of host IFN signaling.

RIG-I deficiency suppresses viral replication *in vivo*. To explore whether RIG-I knockdown in mouse SC altered the behavioral outcome of flaccid paralysis and whether such changes were associated with reduction in virus-induced apoptosis, we infected RIG-I morpholino-treated (RIG-I-Mo) BALB/c mice with virus (Fig. 10A). Immunoblot analysis from RIG-I-Mo mice showed effective RIG-I silencing compared with negative control-treated morpholino (NC-Mo) and only virus-infected animals (Fig. 10B). Significant upregulation of c-casp3 and c-PARP was detected in both only virus-infected (A3, A4) and infected NC-Mo mice (A5, A6), while a lumbar isolate of infected RIG-I-Mo (A7, A8) animals showed drastic reduction in c-casp3 and c-PARP expression. Notably, both JEV and CHPV-infected RIG-I-Mo mice displayed remarkable reduction in viral protein expression compared with respective NC-Mo and only infected animals, suggesting an important role of the RIG-I/pIRF3-7 axis in viral apoptosis and replication *in vivo*.

DISCUSSION

In this study, we propose an AFP mouse model with detailed characterization of molecular pathways that lead to paralysis and spinal MN death. Here, we have used clinical isolates of two different neurotropic viruses belonging to two different families,

FIG 6 Legend (Continued)

experiments, NSC34 cells were either left untreated or were infected with JEV at an MOI of 1 and CHPV at an MOI of 0.1 for various times as stated previously. Blue bar charts represent data from JEV-infected samples and orange bar charts represent data from CHPV-infected samples. (A, i and ii) Lysates prepared from both lumbar cord tissue and NSC34 cells were subjected to Western blot analysis for studying expression of various active caspases and c-PARP, with β-actin used as a loading control. (B and C, i) NSC34 cells were either pretreated with Z-VAD-FMK solvent (DMSO) or Z-VAD-FMK, a pancaspase inhibitor, for 1 h, followed by incubation with virus at said MOIs. Lysates prepared from both mock-infected and virus-infected NSC34 cells with or without Z-VAD-FMK/DMSO treatment were subjected to immunoblot analysis for studying expression of active caspases and c-PARP. (B and C, ii) Densitometric analysis was performed with β-actin as a loading control to determine fold change expression of viral proteins (NS3 for JEV and P-protein for CHPV) in Z-VAD-FMK or DMSO-treated, mock-infected, or virus-infected NSC34 cells. (B and C, iii) Viral titer was determined in culture supernatant using plaque assay at indicated time points after JEV and CHPV infection in Z-VAD-FMK- or DMSO-treated NSC34 cells. Here, dashed lines represent the limit of detection of plaque assay for all experiments conducted. (B and C, iv) Caspase 3/7 activity was measured in NSC34 cells after JEV and CHPV infection at the indicated time points with or without pretreatment of Z-VAD-FMK/DMSO. Data here represent mean $\pm$ SD from a minimum of 3 independent experiments, where statistical significance (*, $P < 0.05$; **, $P < 0.01$; ***, $P < 0.001$; NS, nonsignificant) was calculated using one-way ANOVA followed by *post hoc* Bonferroni correction.

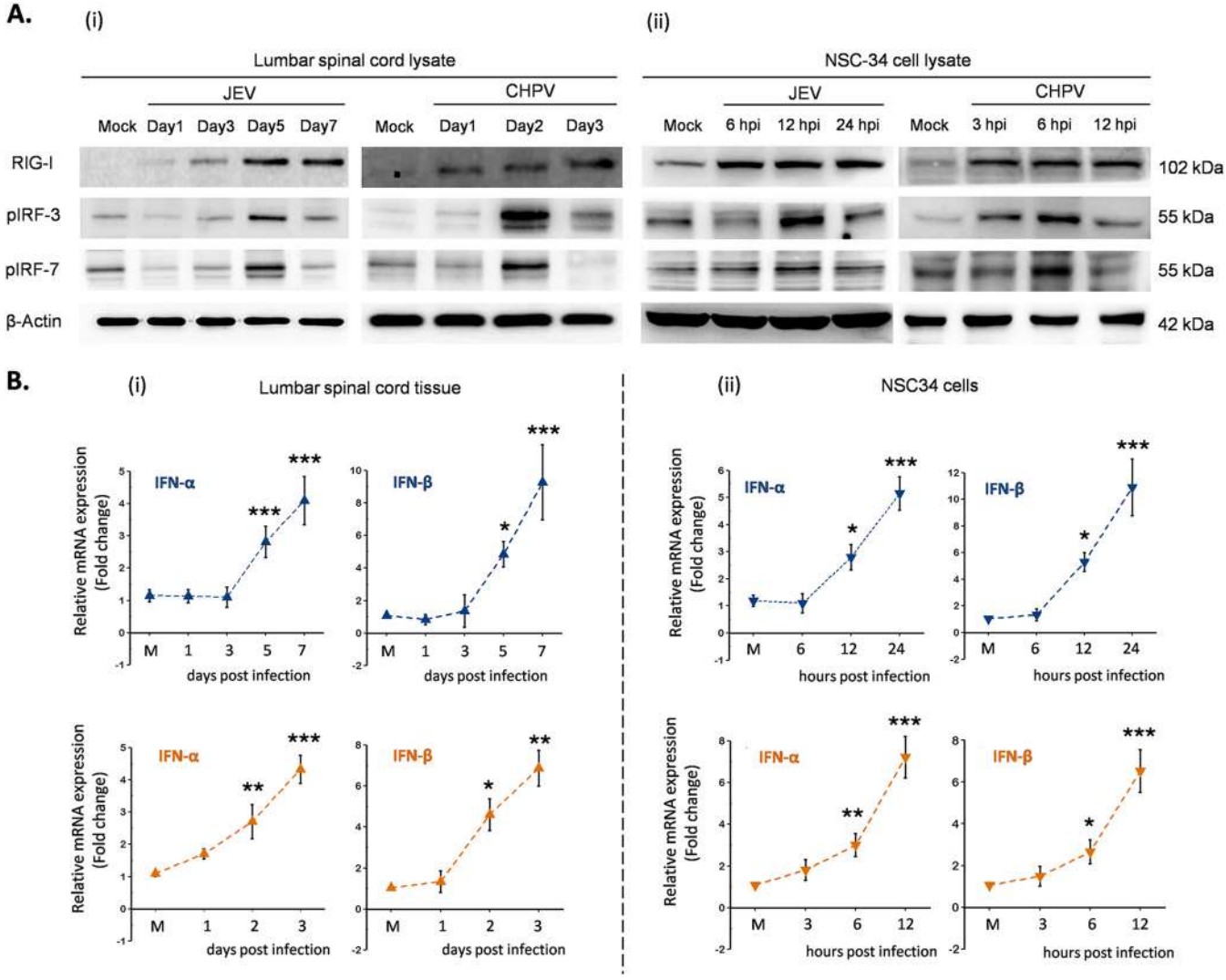

FIG 7 JEV and CHPV activates type-1 interferon production through RIG-I dependent pathway. For *in vivo* studies, 10-day-old BALB/c mice were either mock infected or inoculated intraperitoneally with 3×10^4 PFU of JEV or 1×10^4 PFU of CHPV, and for *in vitro* paradigms, NSC34 cells were either left uninfected or were infected with JEV at an MOI of 1 and CHPV at an MOI of 0.1 for various time points of infection. Blue bar charts represent data from JEV-infected samples and orange bar charts represent data from CHPV-infected samples. (A, i and ii) Lysates prepared from both lumbar cord tissue and NSC34 cells were subjected to Western blot analysis for studying expression of RIG-I and downstream proteins, with β-actin used as a loading control for all experiments. (B, i and ii) Total RNA was extracted from both lumbar spinal cord and NSC34 cells for studying gene expression of type-1 IFNs using qRT-PCR, with fold change being calculated with GAPDH as a loading control. For all experiments, data represent mean ± SD from a minimum of 3 independent experiments, where statistical significance (*, $P < 0.05$; **, $P < 0.01$; ***, $P < 0.001$; NS, nonsignificant) was calculated using one-way ANOVA followed by *post hoc* Bonferroni correction.

namely, *Flaviviridae* and *Rhabdoviridae*, for inducing paralysis in mice. When injected intraperitoneally, both viruses successfully induced AFP with consistent features of abnormal posture, hindlimb clasping, and gait abnormalities. This observation is in line with retrospective studies performed with JE-infected patients who presented prodromal features of nonspecific illness, which rapidly progressed to flaccid paralysis both in JE conscious and convalescent patients (41, 42).

Since lower-limb paralysis is a more commonly reported symptom of neurotropic virus infections, we mainly restricted our focus to the lumbar segment of SC. Both JEV- and CHPV-infected lumbar sections displayed features of chromatolysis, with increased viral replication in infected tissue with time. Consistent with these findings, paralyzed mice showed direct colocalization of SMI32 with virus-specific antigens, suggesting a strong association between paralysis onset and virus replication. Additional support came from studies with JE-conscious patients who displayed damaged anterior horn

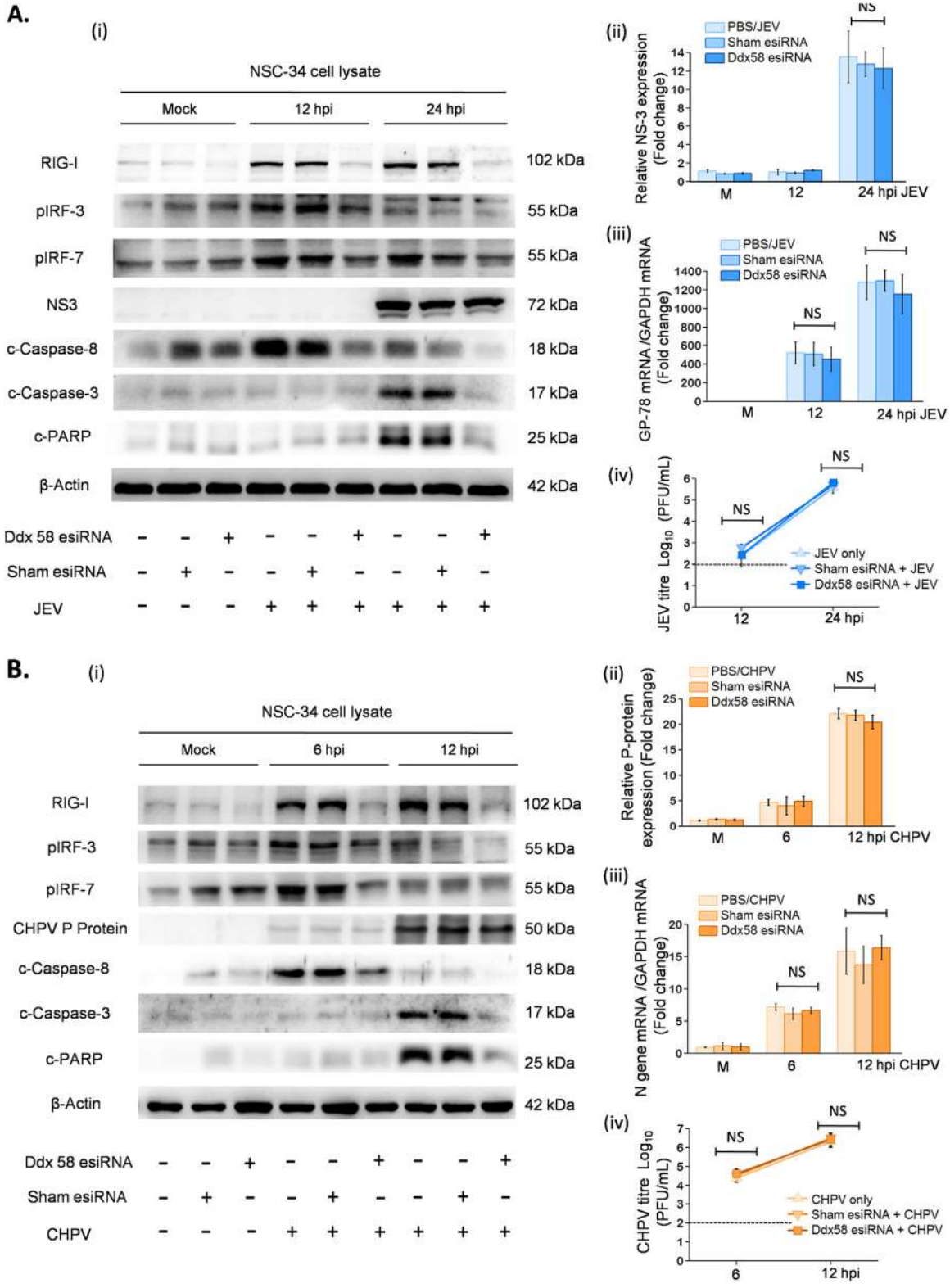

FIG 8 RNA interference using specific RIG-I siRNA abrogates MN apoptosis *in vitro*. NSC34 cells were either transfected with specific RIG-I esiRNA or negative-control eGFP esiRNA for 8 h. Posttransfection, cells were maintained in DMEM for another 16 h and were later infected with JEV at an MOI of 1 and CHPV at an MOI of 0.1 for indicated time points. (A and B, i) Cell lysates prepared from mock-infected control, only virus-infected NSC34, mock-infected RIG-I or eGFP-transfected cells, and virus-infected RIG-I or eGFP-transfected cells were subjected to immunoblot analysis for studying protein expression of RIG-I, pIRF3, pIRF7, NS3, P protein, cleaved caspases, cleaved-PARP, and β-actin. (A and B, ii) Densitometric analysis was performed with β-actin as a loading control to determine fold change in

(Continued on next page)

cells on electrophysiological and MRI experiments (27, 43). Since it is difficult to delineate complex signaling pathways leading to MN death in animal models, we planned to perform experiments employing a reductionist model comprised of infection of motor neuron cell line NSC34 with JEV and CHPV. Together, findings from our *in vivo* and *in vitro* experiments led us to conclude that direct viral injury is responsible for paralytic disease and MN death upon infection.

Numerous reports previously demonstrated the role of apoptosis in pathogenesis of lethal encephalitis (30, 31, 34, 44); however, no report has yet illustrated the role of spinal MN death in virus-induced AFP. In this study, we reported conclusively that upon infection MN undergoes extrinsic apoptotic signaling via activation of the RIG-I/pIRF3-7 axis. Essentially, we demonstrated that RIG-I-transfected-NSC34 cells abrogated apoptosis, with no significant activation of other viral PAMP expression (see Fig. S4 in the supplemental material), suggesting that RIG-I, not the TLR system, plays a critical role in MN apoptosis. Interestingly, RIG-I ablation in NSC34 cells reduced interferon expression upon infection, reinforcing the notion that IFN signaling is activating virus-induced apoptosis of MNs. However, receptor-blocking experiments with IFNAR antibody clearly suggested that virus-induced apoptosis in NSC34 cells is independent of interferon signaling. It is possible that RIG-I activation stimulates the production of pIRF3-induced IFN-independent genes (likely ISG54 and ISG56) that eventually lead to infection-elicited apoptosis (45, 46). Nonetheless, it needs to be highlighted that it is still uncertain how IFN-independent genes orchestrate the induction of apoptosis during infection in MNs.

Surprisingly, with our *in vivo* model, we made contrasting observations where CNS ablation of RIG-I significantly enhanced resistance to infection, clearly visible by reduced expression of viral proteins and apoptotic markers rather than increased susceptibility to infection, as reported previously (46, 47). Notably, in our paradigm, transient ablation of RIG-I in CNS using vivo-morpholino attenuated both antiviral and inflammatory arms of innate immune response, which may have interfered with replication of virus in SC compared to the control-treated morpholino animals, which displayed no change in virus protein expression. A plausible explanation for our interesting *in vivo* observation could be the decreased permeability of the BBB for systemic virus due to localized ablation of RIG-I in brain and SC. Although our *in vivo* data do not strongly support whether attenuated cellular death in RIG-I-knockdown animals is mediated directly via type 1 interferon response and/or indirectly via host cytokine response upon infection, our results provide one clear explanation as to how transient silencing of RIG-I in motor neuron NSC34 cells attenuated apoptosis by suppressing pIRF3/7 signaling effectively by blocking p-IRF3-induced IFN-independent genes (likely ISG54 and ISG56) and not any other IFN-dependent pathways (interferon-β production and IFNAR signaling).

In conclusion, the central finding of this paper is that upon infection, MNs induce RIG-I-dependent activation of apoptosis and type 1 interferon pathways, although upon infection the host cell remains resistant to antiviral effects of IFNs and undergoes apoptosis by following IFN-independent pathways.

MATERIALS AND METHODS

Viruses. The GP78 strain of JEV was propagated in suckling BALB/c mice (48), while CHPV strain 1653514, a kind gift by Dhrubajyoti Chattopadhyay (Amity University, Kolkata, India), was propagated in

FIG 8 Legend (Continued)
expression of viral proteins (NS3 for JEV and P-protein for CHPV) in mock-infected or virus-infected NSC34 cells with or without transfection with RIG-I siRNA or negative-control eGFP siRNA. (A and B, iii) Total RNA was extracted from both mock and experimental NSC34 cells following JEV and CHPV infection posttransfection at the indicated time points. Relative abundance of viral transcripts was determined using qRT-PCR analysis as fold change, where GAPDH was used as a loading control. (A and B, iv) Plaque assays were conducted using NSC34 culture supernatant after RIG-I-specific or negative-control eGFP transfection, followed by JEV and CHPV infection at the indicated time points. In the bar graph, dashed lines represent the limit of detection of plaque assay for experiments performed. Data represent means ± SD from a minimum of 3 independent experiments, where statistical significance (*, $P < 0.05$; **, $P < 0.01$; ***, $P < 0.001$; NS, nonsignificant) was calculated using one-way ANOVA followed by *post hoc* Bonferroni test.

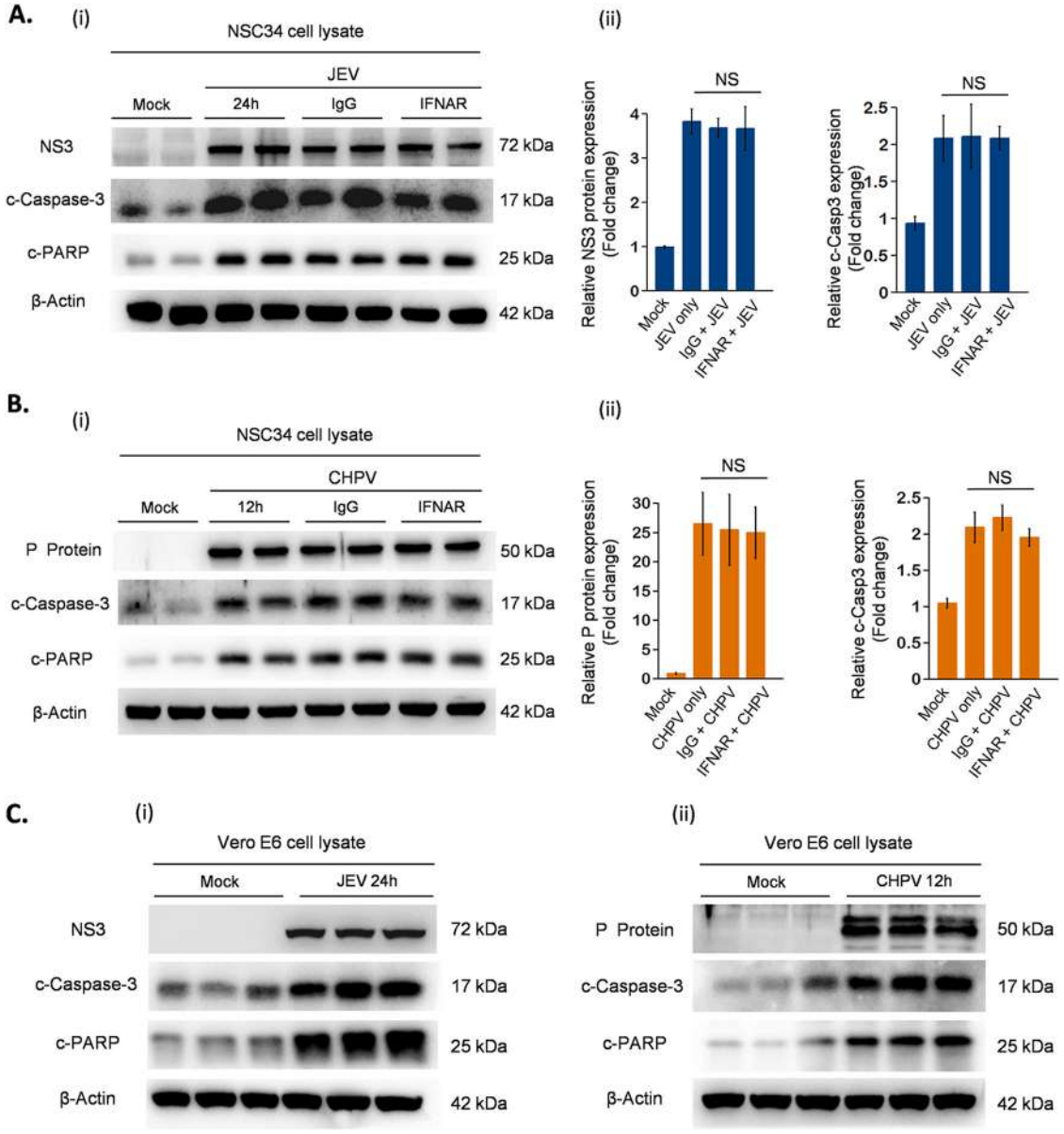

FIG 9 Characterization of mechanism involved in virus-induced apoptosis of NSC34 cells. Experiments were performed with IFN-responsive cell line NSC34 and IFN-unresponsive cell line Vero E6. NSC34 cells prior to infection were treated with neutralizing antibodies against IFNAR receptor or IgG control for 1 h, followed by infection with either JEV or CHPV at said MOIs. Postinfection, cells were maintained again with neutralizing antibody IFNAR or IgG control at a concentration of 10 μg/ml. Similar to NSC34, E6 Vero cells were mock infected and infected with JEV at an MOI of 1 and CHPV at an MOI of 0.1 for 24 and 12 h, respectively. (A, B, and C) Cell lysate prepared from both NSC34 cells and Vero E6 cells postinfection was subjected to Western blot analysis for studying expression of viral protein, cleaved-casp-3, and c-PARP, with β-actin as a loading control. (A and B, ii) Densitometric analysis was performed using FIJI to determine fold change in expression of viral proteins and cleaved-casp-3 in mock-infected or virus-infected NSC34 cells with or without treatment with IFNAR or IgG control antibody. The data are represented as mean $\pm$ SD from a minimum of 3 independent experiments, where *P* values were calculated (*, $P < 0.05$; **, $P < 0.01$; ***, $P < 0.001$) using one-way ANOVA followed by *post hoc* Bonferroni correction.

the Vero E6 cell line (35). Both viral preparations were analyzed briefly for determining number of PFU using plaque assay as described earlier (49).

Mouse experiments and behavioral scoring. All studies performed with animals were approved by the Animal Ethics Committee of National Brain Research Centre (approval no. NBRC/IAEC/2017/130) and were in accordance with the guidelines of the Committee for the Purpose of Control and Supervision of Experiments on Animals (CPCSEA), Ministry of Environment and Forestry, Government of India. BALB/c mice were purchased from The Jackson Laboratory (Bar Harbor, ME) and were housed at the pathogen-free and climate-controlled animal facility of the NBRC. Viral infections were performed on 10-day-old litters that were always housed with their mothers for milk feeding. Pups of either sex were inoculated intraperitoneally with 3×10^4 PFU of JEV or 10^4 PFU of CHPV in a 25-μl volume. Mice were examined twice

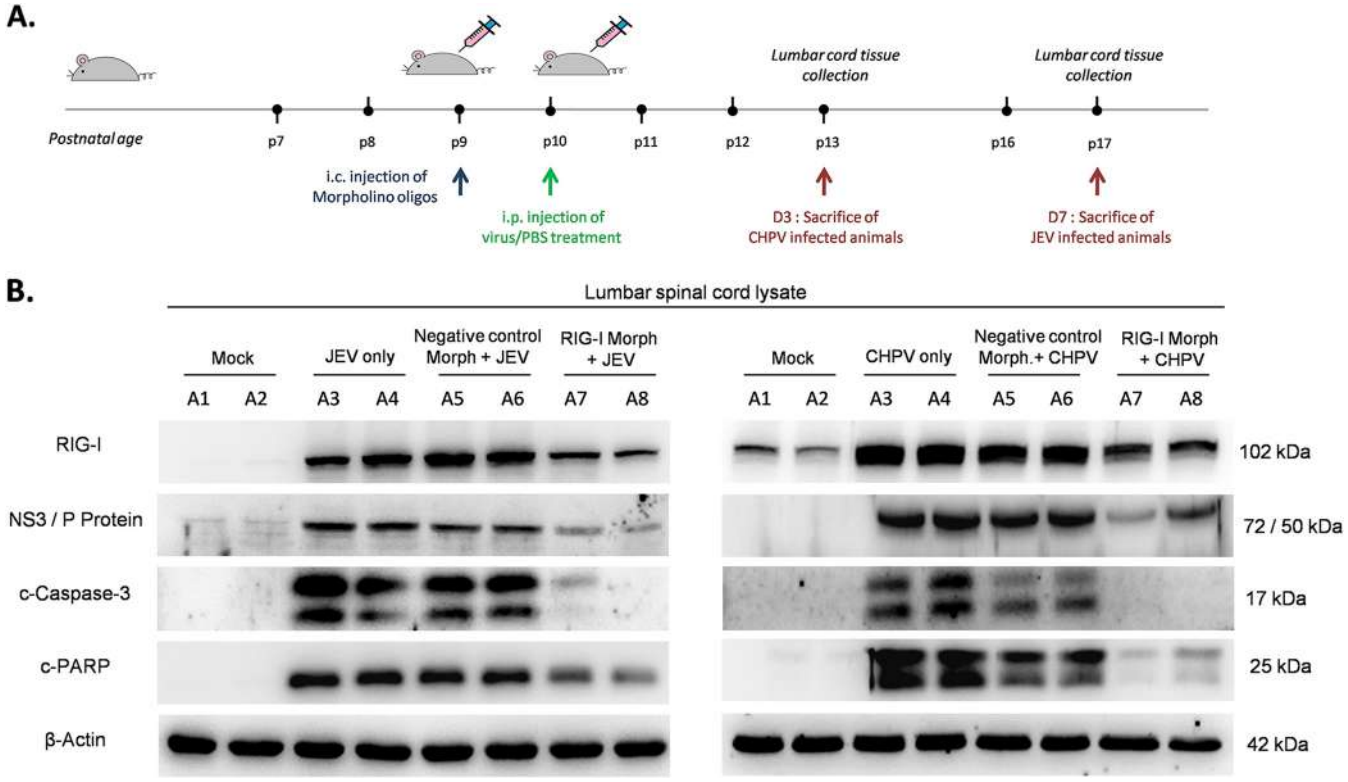

FIG 10 Inhibition of RIG-I *in vivo* abrogates cellular apoptosis in lumbar cord tissue. (A) Nine-day-old BALB/c mice were either treated with RIG-I-specific vivo-morpholino or negative-control vivo-morpholino (mock-morpholino) intracranially. After 24 h, pups were either injected with PBS (mock infection) or JEV at an MOI of 3×10^4 PFU or CHPV at an MOI of 1×10^4 PFU intraperitoneally. Lumbar cord tissue was harvested at day 7 pi for JEV and day 3 pi for CHPV, when pups displayed complete hindlimb paralysis with difficult or no movement at all. (B) Tissue lysates prepared from both mock-infected and virus-infected pups with or without specific vivo-morpholino or negative-control vivo-morpholino treatments were subjected to immunoblot analysis for studying expression of RIG-I receptor, viral proteins (NS3 for JEV and P-protein for CHPV infection), cleaved-casp-3, and cleaved-PARP, with β-actin used as a loading control. Data here are a representation of a minimum of 3 independent experiments performed.

daily, and behavioral experiments were performed once a day until clinical features of paralysis appeared (Table 1).

Tissue processing and IHC. For lumbar cord isolation, pups were deeply anaesthetized with ketamine and perfused transcardially using phosphate-buffered saline (PBS). Mice were sacrificed at days 1, 3, 5, and 7 of JEV and days 1, 2, and 3 of CHPV infection. Tissue samples obtained were used for RNA and protein isolation; however, for immunohistochemistry (IHC) and Nissl staining, pups were transcardially fixed with paraformaldehyde (PFA) solution. Isolated lumbar cords were postfixed in PFA overnight, followed by cryopreservation in 30% sucrose until saturated. Serial sections of 20-μm thickness

TABLE 1 Behavioral assessment and animal scoring after viral infection

Test type	Description
General locomotory behavior test[a] (GLB score)	0, normal locomotion supported by all four limbs; abdomen not touching the ground 1, tip-toe walk with elevated abdomen 2, hind leg inhibition with severe limp and lowered pelvis 3, difficult or no movement, paralysis of hindlimbs and abdomen touching the ground
Hindlimb clasping test[b] (HLC score)	0, hindlimbs consistently splayed away from midline 1, one of the hindlimb retracted towards midline 2, both hindlimbs partially retracted towards midline for more than 50% of observation time 3, both hindlimbs completely retracted towards midline for more than 50% of suspended time
Footprinting test[c]	Each run was analyzed for three parameters: stride length, sway length, and stance length (distance in cm)

[a]For evaluating GLB score, experimental pups were allowed to move freely in an open box having dimensions of 35 by 15 cm and were scored 0, 1, 2, and 3, representing none, moderate, marked, and extreme magnitude of locomotion deficits.
[b]For evaluating HLC score, mice were grasped from the base of the tail and suspended briefly in the air for 15 s, and pups were scored 0, 1, 2, and 3 on the basis of the position of hindlimbs.
[c]For the footprinting test, hind paws of mice were painted in nontoxic dye and pups were motivated to walk on narrow lanes lined with white paper. For analysis and quantification, the first few and last few footmarks were excluded and only the middle portion of each run was evaluated.

were prepared using a cryostat (Leica CM3050S) and permeabilized with 0.1% Triton X-100 in PBS. Afterwards, sections were blocked with serum and incubated overnight with primary antibodies NS3 (1:500; GeneTex), CHPV P protein (1:500; kind gift by Bharat Biotech International Limited, Hyderabad, India), and SMI-32 (1:500; Millipore) at 4°C. Stained sections next were subjected to PBXT washes and were later incubated with appropriate Alexa-fluor-tagged secondary antibody. Tissue sections were then either double stained using second primary antibody or mounted with 4′,6-diamidino-2-phenylindole (DAPI) (Vector Laboratories, USA). Images were captured on a Zeiss Apotome microscope (Carl Zeiss, Germany) at ×20 magnification.

Nissl staining. Lumbar sections were briefly rehydrated in Milli-Q and were subjected to cresyl violet staining. Sections were next immersed in differentiating solution (1:1 absolute ethanol and dioxane), followed by dehydration in dioxane (Merck-Millipore, Sigma) and tissue clearance in xylene (Merck-Millipore, Sigma). Finally, slides were mounted with DPX (dibutylpthalate polystere xylene) (Sigma) and were dried for 24 h in dark boxes. Images were captured on a Leica DMRXA2 microscope at ×5 and ×40 oil magnifications.

Cell lines, infections, and Z-VAD-FMK treatment. Motor neuron cell line NSC34, a kind gift from Jean-Pierre Julien (Laval University, Canada), Vero E6 cell line, a gift from Debi P. Sarkar (Delhi University, India), and porcine stable kidney cells (PS cells), a gift from G. R. Medigeshi (THSTI, India), were cultured in Dulbecco's modified Eagle's medium (DMEM) (Gibco), while a gastric adenocarcinoma cell line (AGS), a kind gift from Ellora Sen, was cultured in DMEM F-12 supplemented with 10% fetal bovine serum (FBS), penicillin (100 U/ml), and streptomycin (100 mg/ml) (Gibco) at 37°C. NSC34 cells were seeded and switched to serum-free DMEM upon reaching confluence 2 h prior to virus inoculation. For experiments, cells were infected at a multiplicity of infection (MOI) of 1 for JEV or 0.1 for CHPV for 2 h, followed by PBS wash to remove any noninternalized virus. Monolayers were then maintained in 5% DMEM, and cells were harvested at various time points postinfection for time-dependent studies. For Z-VAD-FMK (InvivoGen, USA) inhibitor experiments, NSC34 cells were divided into four groups: mock infection, virus infection, mock infection and Z-VAD-FMK treatment, and virus infection and Z-VAD-FMK treatment. Cells were pretreated with Z-VAD-FMK (20 μM) for 2 h and were later infected with virus. Postinfection, samples were harvested and cell supernatants were collected at the indicated time points for various cell death assays and immunoblotting experiments.

Cell viability assay. Viability of cultured cells was determined using cell proliferation reagent WST1 (Roche, Sigma) per the manufacturer's instructions. NSC34 cells were seeded at a density of 2×10^4 cells per well in separate 96-well plates, followed by infection at said MOIs. Twenty microliters of WST1 solution was added to each well after 6, 12, and 24 hpi for JEV and 3, 6, and 12 hpi for CHPV. Absorbance was recorded at 490 nm using a Multiskan Sky spectrophotometer (Thermo Fischer), reflecting the formation of formazan product by metabolically active cells. Results were expressed as relative percentages of virus-infected cells to that of mock-infected cells.

Transfection procedures and siRNA knockdown. Transient transfection of NSC34 cells was performed using Lipofectamine RNAiMAX reagent (Invitrogen, USA) per the manufacturer's instructions. Briefly, cells were cultured in DMEM until they attained a confluence of 60 to 70%, after which cells were transfected with 30 pmol siRNA specific to RIG-I (Ddx58) and a negative-control enhanced green fluorescent protein (eGFP). Transfection was performed in Opti-MEM for 8 h, after which cells were maintained in 5% DMEM for 16 h. Cells were then serum starved for an additional 2 h before being treated with virus as stated earlier. Postinfection, samples were harvested and supernatants were collected at different time points for various biochemical assays.

Live/dead assay. NSC34 cells were briefly seeded in 12-well plates and transfected upon reaching confluence. Posttransfection, cells were treated with virus at said MOIs for 12 and 24 hpi for JEV and 6 and 12 hpi for CHPV. NSC34 cells were then incubated with LIVE/DEAD reagent (Invitrogen, Thermo Fischer) at a concentration of 4 μM ethidium dimer-D1 and 2 μM Calcein-AM in the dark. Images were captured and analyzed using a Zeiss Axio Vert.1 microscope at ×10 magnification.

Immunocytochemistry. Briefly, NSC34 cells were grown in 8-well chamber slides, followed by infection with JEV and CHPV at said MOIs. Postinfection, cells were fixed with 4% paraformaldehyde solution and were blocked using bovine serum albumin (Sigma). Cells were then incubated overnight with primary antibodies NS3 (1:500) and CHPV P protein (1:500) at 4°C, followed by extensive washing. Finally, cells were incubated with appropriate Alexa fluor-tagged secondary antibody and were mounted with DAPI. Images were captured on a Zeiss Apotome microscope at ×20 magnification.

RNA isolation and qRT-PCR analysis. Total cellular RNA was isolated from lumbar cord tissue and NSC34 cells using Tri reagent (Sigma-Aldrich, USA). Briefly, cDNA was synthesized using random hexamer primers (Verso cDNA synthesis kit), and quantitative real-time PCRs (qRT-PCRs) were performed using Power SYBR green (Applied Biosystems, USA) with gene-specific primers (Table 2). Relative gene abundance for each reaction was determined using the delta threshold cycle method with glyceraldehyde-3-phosphate dehydrogenase (GAPDH) as a loading control in a ViiA 7 real-time PCR system (Applied Biosystems). Results were expressed as fold differences between mock- and virus-infected samples.

Protein isolation and immunoblotting. Whole-cell protein extract and tissue lysates were prepared as described previously (50), with protein concentration estimated using bicinchoninic acid (BCA) reagent. Equal amounts of protein samples were resolved by SDS-PAGE and transferred onto nitrocellulose membrane. Subsequently, membranes were blocked and incubated with primary antibodies specific for RIG-I (1:1,000; CST), cleaved-caspase-3 (1:1,000; CST), c-casp-8 (1:1,000; CST), caspase-9 (1:1,000; CST), cleaved-poly ADP-ribose polymerase (c-PARP; 1:2,000; Abcam), pIRF-3 (1:2,000; CST), pIRF-7 (1:2,000; CST), NS-3 (1:10,000), CHPV P protein (1:3,000), MDA5 (1:1,000; Abcam), TLR3 (1:1,000; Santa Cruz), TLR4 (1:1,000; Abcam), TLR7 (1:1,000; Abcam), and β-actin (1:10,000; Sigma) overnight at 4°C. After extensive

TABLE 2 Gene-specific primers

Primer	Sequence
GP-78	5′-TTGACAATCATGGCAAAC-3′ (sense)
	5′-CCCAACTTGCGCTGAATAA-3′ (antisense)
CHPV P gene	5′-ACCTGGCTCCAAATCCAATAC-3′(sense)
	5′-GGTGGATCAGACGGAGAGATA-3′ (antisense)
CHPV N gene	5′-CATTGTCCACTCTGTCACAC-3′ (sense)
	5′-GGCATGTAGGAATCAGCT-3′ (antisense)
GAPDH	TCTCCCTCACAATTTCCATCC (sense)
	GGGTGCAGCGAACTTTATTG (antisense)
IFN-α	5′-ATTGGCTAGGCTCTGTGCTTT-3′ (sense)
	5′-AGGGCTCTCCAGACTTCTGC-3′ (antisense)
IFN-β	5′-AAGAGTTACACTGCCTTTGCCATC-3′ (sense)
	5′-CACTGTCTGCTGGTGGAGTTCATC-3′ (antisense)

washes, blots were probed with peroxidase-conjugated secondary antibodies (Vector Laboratories) and developed using chemiluminescence reagent (Millipore). Images were captured using the Chemigenius bioimaging system (Uvitec Cambridge). To ensure equivalent loading of samples, blots were stripped and reprobed with β-actin.

Quantification of soluble cytokines using flow cytometry. Mouse cytokines interleukin-6 (IL-6), interleukin-10 (IL-10), monocyte chemoattractant protein-1 (MCP-1), IFN-γ, tumor necrosis factor (TNF), and interleukin-12p70 (IL-12p70) were estimated in culture supernatants of virus-infected NSC34 using a mouse inflammation CBA kit (BD Biosciences, USA) per the manufacturer's instructions. Analysis was carried out in FACS Verse (BD Biosciences) using FCAP 2.0 analysis software.

TUNEL staining. TUNEL assay was carried out using Promega's DeadEnd fluorometric TUNEL system per the manufacturer's protocol. Briefly, NSC34 cells were seeded at a density of 2×10^5 cells per well in 8-well chamber slides and infected with virus as described before. Postinfection, cells were fixed with PFA, followed by incubation with recombinant terminal deoxynucleotidyl transferase (rTdT) enzyme mix. Later, cells were washed extensively and mounted with Vectashield mounting medium and DAPI. Images were captured on a Zeiss Apotome at $\times$20 magnification.

Antibody neutralization assay. For antibody-based neutralization assay, NSC34 cells were seeded at a density of 5×10^4 cells per well on 24-well plates. Prior to infection, cells were treated with 10 μg/ml isotype IgG1 K (clone MOPC1; BioLegend) or purified anti-mouse IFNAR-1 (clone MARI-5A3; BioLegend) blocking antibody for 1 h. Cells were then washed with PBS once and infected with virus at said MOIs. Postinfection, cells were maintained in 5% DMEM containing 10 μg/ml neutralizing antibodies and samples were harvested at the indicated time points for immunoblotting.

RIG-I gene knockdown and mouse infection. For vivo-morpholino experiments, 10-day-old BALB/c pups were randomly assigned to four groups: group 1, mock infection; group 2, virus infection only; group 3, virus infection and negative-control vivo-morpholino; and group 4, virus infection and RIG-I vivo-morpholino. Starting a day prior to infection, mice belonging to groups 3 and 4 were injected intracranially with a single dose of RIG-I-specific vivo-morpholino (18.5 mg/kg of body weight; Gene Tools, USA) and negative control (18.5 mg/kg), respectively. After 24 h, all animals were infected intraperitoneally with either PBS or virus at day 0 of infection. Animals were then sacrificed at day 7 pi for JEV and day 3 pi for CHPV, and lumbar cords were harvested for immunoblot analysis.

Statistical analysis. Data were represented as means $\pm$ standard deviations (SD) from a minimum of three independent experiments unless otherwise stated. GraphPad Prism 5 and KyPlot2.0 were used for data analysis and preparation of graphs. Time-course studies were analyzed using one-way analysis of variance (ANOVA) with Bonferroni *post hoc* test, whereas differences between two groups were evaluated using paired two-tailed Student's *t* test with 95% confidence. Any *P* value less than 0.05 was considered statistically significant.

SUPPLEMENTAL MATERIAL

Supplemental material is available online only.

FIG S1, TIF file, 1.7 MB.

FIG S2, TIF file, 1.4 MB.

FIG S3, TIF file, 1.3 MB.

FIG S4, TIF file, 1.3 MB.

FIG S5, TIF file, 1.5 MB.

ACKNOWLEDGMENTS

This study was supported by a core grant to A.B. from NBRC. A.B. is also a recipient of JC Bose Fellowship (JCB/2020/000037) from the Science and Engineering Research Board (SERB), Ministry of Science and Technology, Government of India.

We thank Kanhaiya Lal Kumawat and Manish Dogra for their excellent technical assistance. We also thank Surajit Chakraborty for critically reading the manuscript and giving insightful comments.

We declare no competing financial and/or nonfinancial interests.

REFERENCES

1. Solomon T, Kneen R, Dung NM, Khanh VC, Thuy TT, Ha DQ, Day NP, Nisalak A, Vaughn DW, White NJ. 1998. Poliomyelitis-like illness due to Japanese encephalitis virus. Lancet 351:1094–1097. https://doi.org/10.1016/S0140-6736(97)07509-0.
2. Suresh S, Forgie S, Robinson J. 2018. Non-polio Enterovirus detection with acute flaccid paralysis: a systematic review. J Med Virol 90:3–7. https://doi.org/10.1002/jmv.24933.
3. Saraswathy TS, Zahrin HN, Apandi MY, Kurup D, Rohani J, Zainah S, Khairullah NS. 2008. Acute flaccid paralysis surveillance: looking beyond the global poliomyelitis eradication initiative. Southeast Asian J Trop Med Public Health 39:1033–1039.
4. Johnstone J, Hanna SE, Nicolle LE, Drebot MA, Neupane B, Mahony JB, Loeb MB. 2011. Prognosis of West Nile virus associated acute flaccid paralysis: a case series. J Med Case Rep 5:395. https://doi.org/10.1186/1752-1947-5-395.
5. Messacar K, Asturias EJ, Hixon AM, Van Leer-Buter C, Niesters HGM, Tyler KL, Abzug MJ, Dominguez SR. 2018. Enterovirus D68 and acute flaccid myelitis-evaluating the evidence for causality. Lancet Infect Dis 18:e239–e247. https://doi.org/10.1016/S1473-3099(18)30094-X.
6. Greninger AL, Naccache SN, Messacar K, Clayton A, Yu G, Somasekar S, Federman S, Stryke D, Anderson C, Yagi S, Messenger S, Wadford D, Xia D, Watt JP, Van Haren K, Dominguez SR, Glaser C, Aldrovandi G, Chiu CY. 2015. A novel outbreak enterovirus D68 strain associated with acute flaccid myelitis cases in the USA (2012–14): a retrospective cohort study. Lancet Infect Dis 15:671–682. https://doi.org/10.1016/S1473-3099(15)70093-9.
7. Van Haren K, Ayscue P, Waubant E, Clayton A, Sheriff H, Yagi S, Glenn-Finer R, Padilla T, Strober JB, Aldrovandi G, Wadford DA, Chiu CY, Xia D, Harriman K, Watt JP, Glaser CA. 2015. Acute flaccid myelitis of unknown etiology in California, 2012–2015. JAMA 314:2663–2671. https://doi.org/10.1001/jama.2015.17275.
8. Sejvar JJ, Lopez AS, Cortese MM, Leshem E, Pastula DM, Miller L, Glaser C, Kambhampati A, Shioda K, Aliabadi N, Fischer M, Gregoricus N, Lanciotti R, Nix WA, Sakthivel SK, Schmid DS, Seward JF, Tong S, Oberste MS, Pallansch M, Feikin D. 2016. Acute flaccid myelitis in the United States, August-December 2014: results of nationwide surveillance. Clin Infect Dis 63:737–745. https://doi.org/10.1093/cid/ciw372.
9. Solomon T, Ravi V. 2003. Acute flaccid paralysis caused by West Nile virus. Lancet Infect Dis 3:189–190. https://doi.org/10.1016/S1473-3099(03)00574-7.
10. Chung CC, Lee SS, Chen YS, Tsai HC, Wann SR, Kao CH, Liu YC. 2007. Acute flaccid paralysis as an unusual presenting symptom of Japanese encephalitis: a case report and review of the literature. Infection 35:30–32. https://doi.org/10.1007/s15010-007-6038-7.
11. Morens DM, Folkers GK, Fauci AS. 2019. Acute flaccid myelitis: something old and something new. mBio 10:e00521-19. https://doi.org/10.1128/mBio.00521-19.
12. Mateen FJ, Black RE. 2013. Expansion of acute flaccid paralysis surveillance: beyond poliomyelitis. Trop Med Int Health 18:1421–1422. https://doi.org/10.1111/tmi.12181.
13. United Kingdom Acute Flaccid Paralysis (AFP) Task Force. 2019. An increase in reports of acute flaccid paralysis (AFP) in the United Kingdom, 1 January 2018–21 January 2019: early findings. Euro Surveill 24:1900093. https://doi.org/10.2807/1560-7917.ES.2019.24.6.1900093.
14. Knoester M, Helfferich J, Poelman R, Van Leer-Buter C, Brouwer OF, Niesters HGM, 2016 EV-D68 AFM Working Group. 2019. Twenty-nine cases of enterovirus-D68-associated acute flaccid myelitis in Europe 2016: a case series and epidemiologic overview. Pediatr Infect Dis J 38:16–21. https://doi.org/10.1097/INF.0000000000002188.
15. Pérez G, Rosanova MT, Freire MC, Paz MI, Ruvinsky S, Rugilo C, Ruggieri V, Cisterna D, Martiren S, Lema C, Savransky A, González S, Martínez L, Viale D, Bologna R. 2017. Unusual increase of cases of myelitis in a pediatric hospital in Argentina. Arch Argent Pediatr 115:364–369.
16. Labeaud AD, Bashir F, King CH. 2011. Measuring the burden of arboviral diseases: the spectrum of morbidity and mortality from four prevalent infections. Popul Health Metr 9:1. https://doi.org/10.1186/1478-7954-9-1.
17. World Health Organization. 2012. Weekly epidemiological record, 2012, p 161–168, vol 87. World Health Organization, Geneva, Switzerland.
18. Laxmivandana R, Yergolkar P, Gopalkrishna V, Chitambar SD. 2013. Characterization of the non-polio enterovirus infections associated with acute flaccid paralysis in south-western India. PLoS One 8:e61650. https://doi.org/10.1371/journal.pone.0061650.
19. Liu W, Fu S, Ma X, Chen X, Wu D, Zhou L, Yin Q, Li F, He Y, Lei W, Li Y, Xu S, Wang H, Wang Z, Wang H, Yu H, Liang G. 2020. An outbreak of Japanese encephalitis caused by genotype Ib Japanese encephalitis virus in China, 2018: a laboratory and field investigation. PLoS Negl Trop Dis 14:e0008312. https://doi.org/10.1371/journal.pntd.0008312.
20. Maan HS, Dhole TN, Chowdhary R. 2019. Identification and characterization of nonpolio enterovirus associated with nonpolio-acute flaccid paralysis in polio endemic state of Uttar Pradesh, Northern India. PLoS One 14:e0208902. https://doi.org/10.1371/journal.pone.0208902.
21. Fall A, Ndiaye N, Messacar K, Kebe O, Jallow MM, Harouna H, Kiori DE, Sy S, Goudiaby D, Dia M, Niang MN, Ndiaye K, Dia N. 2020. Enterovirus D68 subclade B3 in children with acute flaccid paralysis in West Africa, 2016. Emerg Infect Dis 26:2227–2230. https://doi.org/10.3201/eid2609.200312.
22. Fang Y, Zhang Y, Zhou Z-B, Xia S, Shi W-Q, Xue J-B, Li Y-Y, Wu J-T. 2019. New strains of Japanese encephalitis virus circulating in Shanghai, China after a ten-year hiatus in local mosquito surveillance. Parasit Vectors 12:22. https://doi.org/10.1186/s13071-018-3267-9.
23. Narain JP, Dhariwal AC, MacIntyre CR. 2017. Acute encephalitis in India: an unfolding tragedy. Indian J Med Res 145:584–587. https://doi.org/10.4103/ijmr.IJMR_409_17.
24. Solomon T, Dung NM, Kneen R, Gainsborough M, Vaughn DW, Khanh VT. 2000. Japanese encephalitis. J Neurol Neurosurg Psychiatry 68:405–415. https://doi.org/10.1136/jnnp.68.4.405.
25. Gurav YK, Tandale BV, Jadi RS, Gunjikar RS, Tikute SS, Jamgaonkar AV, Khadse RK, Jalgaonkar SV, Arankalle VA, Mishra AC. 2010. Chandipura virus encephalitis outbreak among children in Nagpur division, Maharashtra, 2007. Indian J Med Res 132:395–399.
26. Zimmerman HM. 1946. The pathology of Japanese B encephalitis. Am J Pathol 22:965–991.
27. Misra UK, Kalita J, Jain SK, Mathur A. 1994. Radiological and neurophysiological changes in Japanese encephalitis. J Neurol Neurosurg Psychiatry 57:1484–1487. https://doi.org/10.1136/jnnp.57.12.1484.
28. Kumar S, Misra UK, Kalita J, Salwani V, Gupta RK, Gujral R. 1997. MRI in Japanese encephalitis. Neuroradiology 39:180–184. https://doi.org/10.1007/s002340050388.
29. Jackson AC, Moench TR, Griffin DE, Johnson RT. 1987. The pathogenesis of spinal cord involvement in the encephalomyelitis of mice caused by neuroadapted Sindbis virus infection. Lab Invest 56:418–423.
30. Samuel MA, Morrey JD, Diamond MS. 2007. Caspase 3-dependent cell death of neurons contributes to the pathogenesis of West Nile virus encephalitis. J Virol 81:2614–2623. https://doi.org/10.1128/JVI.02311-06.
31. Shrestha B, Gottlieb D, Diamond MS. 2003. Infection and injury of neurons by West Nile encephalitis virus. J Virol 77:13203–13213. https://doi.org/10.1128/jvi.77.24.13203-13213.2003.
32. Wang YF, Chou CT, Lei HY, Liu CC, Wang SM, Yan JJ, Su IJ, Wang JR, Yeh TM, Chen SH, Yu CK. 2004. A mouse-adapted enterovirus 71 strain causes neurological disease in mice after oral infection. J Virol 78:7916–7924. https://doi.org/10.1128/JVI.78.15.7916-7924.2004.
33. Goody RJ, Schittone SA, Tyler KL. 2008. Experimental reovirus-induced acute flaccid paralysis and spinal motor neuron cell death. J Neuropathol Exp Neurol 67:231–239. https://doi.org/10.1097/NEN.0b013e31816564f0.
34. Havert MB, Schofield B, Griffin DE, Irani DN. 2000. Activation of divergent neuronal cell death pathways in different target cell populations during neuroadapted Sindbis virus infection of mice. J Virol 74:5352–5356. https://doi.org/10.1128/jvi.74.11.5352-5356.2000.
35. Ghosh S, Dutta K, Basu A. 2013. Chandipura virus induces neuronal death through Fas-mediated extrinsic apoptotic pathway. J Virol 87:12398–12406. https://doi.org/10.1128/JVI.01864-13.

36. Verma AK, Ghosh S, Pradhan S, Basu A. 2016. Microglial activation induces neuronal death in Chandipura virus infection. Sci Rep 6:22544. https://doi.org/10.1038/srep22544.
37. Mukherjee S, Akbar I, Kumari B, Vrati S, Basu A, Banerjee A. 2019. Japanese encephalitis virus-induced let-7a/b interacted with the NOTCH-TLR7 pathway in microglia and facilitated neuronal death via caspase activation. J Neurochem 149:518–534. https://doi.org/10.1111/jnc.14645.
38. Swaroop S, Mahadevan A, Shankar SK, Adlakha YK, Basu A. 2018. HSP60 critically regulates endogenous IL-1β production in activated microglia by stimulating NLRP3 inflammasome pathway. J Neuroinflammation 15:177. https://doi.org/10.1186/s12974-018-1355-6.
39. Verma AK, Ghosh S, Basu A. 2018. Chandipura virus induced neuronal apoptosis via calcium signaling mediated oxidative stress. Front Microbiol 9:1489. https://doi.org/10.3389/fmicb.2018.01489.
40. Kaushik DK, Mukhopadhyay R, Kumawat KL, Gupta M, Basu A. 2012. Therapeutic targeting of Krüppel-like factor 4 abrogates microglial activation. J Neuroinflammation 9:57. https://doi.org/10.1186/1742-2094-9-57.
41. Misra UK, Kalita J. 1997. Movement disorders in Japanese encephalitis. J Neurol 244:299–303. https://doi.org/10.1007/s004150050090.
42. Solomon T, Vaughn DW. 2002. Pathogenesis and clinical features of Japanese encephalitis and West Nile virus infections. Curr Top Microbiol Immunol 267:171–194. https://doi.org/10.1007/978-3-642-59403-8_9.
43. Misra UK, Kalita J. 1997. Anterior horn cells are also involved in Japanese encephalitis. Acta Neurol Scand 96:114–117. https://doi.org/10.1111/j.1600-0404.1997.tb00250.x.
44. Thach DC, Kimura T, Griffin DE. 2000. Differences between C57BL/6 and BALB/cBy mice in mortality and virus replication after intranasal infection with neuroadapted Sindbis virus. J Virol 74:6156–6161. https://doi.org/10.1128/jvi.74.13.6156-6161.2000.
45. Pulit-Penaloza JA, Scherbik SV, Brinton MA. 2012. Type 1 IFN-independent activation of a subset of interferon stimulated genes in West Nile virus Eg101-infected mouse cells. Virology 425:82–94. https://doi.org/10.1016/j.virol.2012.01.006.
46. Ashley CL, Abendroth A, McSharry BP, Slobedman B. 2019. Interferon-independent upregulation of interferon-stimulated genes during human cytomegalovirus infection is dependent on IRF3 expression. Viruses 11:246. https://doi.org/10.3390/v11030246.
47. Hiscott J, Paz S, Nakhaei P. 2011. CS09-7. Cross-talk between RIG-I dependent antiviral signalling and apoptosis. Cytokine 56:57. https://doi.org/10.1016/j.cyto.2011.07.359.
48. Kaushik DK, Gupta M, Kumawat KL, Basu A. 2012. NLRP3 inflammasome: key mediator of neuroinflammation in murine Japanese encephalitis. PLoS One 7:e32270. https://doi.org/10.1371/journal.pone.0032270.
49. Mukherjee S, Sengupta N, Chaudhuri A, Akbar I, Singh N, Chakraborty S, Suryawanshi AR, Bhattacharyya A, Basu A. 2018. PLVAP and GKN3 are two critical host cell receptors which facilitate Japanese encephalitis virus entry into neurons. Sci Rep 8:11784. https://doi.org/10.1038/s41598-018-30054-z.
50. Hazra B, Chakraborty S, Bhaskar M, Mukherjee S, Mahadevan A, Basu A. 2019. miR-301a regulates inflammatory response to Japanese encephalitis virus infection via suppression of NKRF activity. J Immunol 203:2222–2238. https://doi.org/10.4049/jimmunol.1900003.